MICROFLUIDICS SENSOR TO DETECT WATER SALINITY AND BACTERIA USING OPTICAL AND ELECTRICAL METHODS

MohammadJavad FarshchiHeydari

A THESIS SUBMITTED TO THE FACULTY OF GRADUATE STUDIES

IN PARTIAL FULFILLMENT OF THE REQUIREMENTS FOR THE DEGREE OF

MASTER OF APPLIED SCIENCE

GRADUATE PROGRAM IN MECHANICAL ENGINEERING

YORK UNIVERSITY

TORONTO, ONTARIO

May 2022

Abstract

Supplying safe water is becoming more challenging as the world population constantly grows. Contaminants of various sources pollute waters worldwide and pose serious health issues to humans. Thereby, regular monitoring of the water quality in swift, reliable, low-cost, and *in-situ* manners is crucial.

The conventional water contamination detection methods mostly require bulky and expensive lab equipment, trained personnel, and sample collection and transportation to labs that make them unsuitable for the mentioned needs. Numerous microfluidics-based contamination sensors have been presented. These sensors show great potential for miniaturization of detection platforms that enable on-site detection and quantification of target analytes at a lower cost and with faster response times than conventional techniques.

Despite the above advantages of microfluidic-based sensors, their detection performance is usually inferior to those of laboratory-based methods. These detection limitations frequently inhibit commercialization and/or widespread adoption of microfluidics solutions. In this respect, this thesis aims to design an inexpensive sensor to narrow the gap between some of the sensing requirements in conventional lab-based methods and the necessary point-of-need qualities like miniaturization and lower cost. The low-cost characteristic in this thesis solely refers to the cost of device materials and fabrication. The cost of accessories for operation and mass production should be considered in the future.

The **first objective** of the thesis was to develop and optimize a low-cost microfluidic water monitoring platform through experimental and numerical investigations. The proposed design employed two microwires suspended orthogonally in a microchannel, like two bridges across a road, to measure water content contamination (e.g., salt and bacteria) based on the electrical resistance between the microwires. The sensor's detection capability was investigated through experimental analysis to detect sodium chloride (NaCl), as an ionic contamination surrogate. The preliminary design of the sensor could measure water salinity in the range of 1-20ppm in less than one minute with detection sensitivity, limit of detection (LOD), and limit of quantification (LOQ) of 17.1 Ohm/Ohm.cm, 0.31 ppm, and 0.37 ppm, respectively.

For the **second objective** of the thesis, data from the preliminary design was used for developing and validating a numerical model, which was subsequently used for parametric studies and optimization to improve the sensor's performance. Accordingly, an optimized sensor was developed and applied for NaCl detection, then compared to the primary design. An order of magnitude increase in sensitivity (385 Ohm/Ohm.cm), a 6-fold wider detection range (1-120ppm), and a 15-fold enhancement in miniaturization of the microfluidic channel was obtained with similar LOD and LOQ of 0.39 and 0.44 ppm to the primary sensor, respectively.

For the **third objective** of the thesis, the developed sensor was applied to the detection of biological contaminations. *E. coli* K12 was selected as a bacteria surrogate for the detection with electrical and photothermal methods at the surface of the wires. For the electrical detection section, anti-*E. coli* antibodies were immobilized on the gold-coated microwires for capturing *E. coli* K12 from the sample. Electrical conductivity between the two wires was measured prior to and after bacteria capturing on the wires and was correlated to bacteria counts. The electrical detection showed successful detection and quantification of bacteria at 10^6 and 10^7 CFU/mL. For photothermal detection, a compact hand-held platform was developed to facilitate the detection of bacteria off-chip. In this method, the antibody-immobilized wires were first used to capture bacteria. Then, gold nanoparticles (GNPs) coated with anti-*E. coli* K12 antibodies were used to sandwich the bacteria on the wires. Lastly, the photothermal activities of the GNPs as a result of laser irradiation were recorded by infrared radiation and correlated to the bacteria counts. The analysis showed successful detection of *E. coli* in the range of 10-10^7 CFU/mL with an LOD of 10 CFU/mL and an approximate resolution of 10^3 CFU/mL.

We envision that the integration of this sensing platform into a handheld device would allow for addressing the current unmet need for low-cost and on-field contamination surveillance of drinking water in the future.

Dedication

To my beloved mother, father, and sister. To my wife, my sweetheart and companion.

Acknowledgement

I want to express my sincere appreciation to my M.Sc. supervisors, Professor Pouya Rezai and Professor Nima Tabatabaei, for their support and guidance throughout the past two years. I was fortunate to learn a lot from both, professionally and personally. Apart from the technical aspects, I learned that any accomplishment requires consistency, passion, hard work, modesty, and obsessive attention to minutia without losing sight of the big picture.

I would also like to thank the time and consideration of my defence committee, Professors Satinder Brar and Stephanie Gora, who kindly examined and critically reviewed my thesis.

I am grateful to all my current and previous tenacious and learned colleagues in the Advanced Center for Microfluidics Technology and Engineering (ACμTE) and Hybrid Biomedical Optics (HBO) labs, who helped me with insightful comments, suggestions, and fruitful conversations. I would like to also thank Dr. Khaled Youssef for his continuous support and help throughout my master's. I am thankful for having the chance to work with Dr. Vasily Panferov and Daphne-Eleni Archonta during the last six months of my studies who helped me with some of the preparations, protocols, and experimentation.

Being an international student, the first few months in Toronto would have been more difficult without the help of my friends. I want to thank Amir-Ali Ebrahimirad and Ali Gholami for their continued presence and support. I would also like to thank my friends in other parts of Canada and aboard who have been supportive regardless of the long distance.

I would also like to express my deepest gratitude and love to my whole family, mom, dad's spirit, sister, wife, and her wonderful family. I would have never been where I am now without their unconditional love and support.

Table of Contents

List of Figures

List of Tables

List of Abbreviations

Abbreviation	Explanation	Abbreviation	Explanation
μ-PAD	Microfluidic paper-based analytical device	HRP	Horseradish peroxide
PVC	Polyvinyl chloride	ECL	Electrochemiluminescence
LOD	Limit of detection	SPE	Screen-printed electrodes
QCM	Quartz crystal microbalances	DBAE	2-(Dibutylamino)-ethanol
SAW	Surface acoustic wave	NADH	Nicotinamide adenine dinucleotide
MCL	Microcantilever	TMB	3,3′,5,5′-tetramethylbenzidine
SPR	Surface plasmon resonance	mFSH	Mouse follicle stimulating hormone
RIU	Refractive index unit	GO	Graphene oxide
TEM	Transmission electron microscopy	MoS2	Molybdenum disulfide
CMOS	Complementary metal–oxide–semiconductor	AT	Active thermography
AC	Alternating current	NDT	Non-Destructive Testing
DC	Direct current	PT	Pulse Thermography
LOQ	limit of quantification	LIT	Lock-In Thermography
MNP	Magnetic nanoparticle	PPT	Pulse-Phase Thermography
FNP	Fluorescent nanoparticles	MT	Matched-Filter Thermography
QD	Quantum dots	LFA	lateral flow immunoassays
pDEP	Positive dielectrophoretic force	GNP	Gold nanoparticles
CL	Chemiluminescence	BSA	Bovine serum albumin
PMMA	Poly(methyl methacrylate)	MES	2-(N-morpholino)ethanesulfonic acid
PDMS	Polydimethylsiloxane	FDA	Food and Drug Administration
OPD	Organic photodiode	CFU/mL	Colony-forming unit per mL
APTES	(3-Aminopropyl)triethoxysilane	Ab	Antibody
EDC	1-Ethyl-3-(3-dimethylaminopropyl)carbodiimide	pAb	Polyclonal antibody
NHS	N-Hydroxysuccinimide	mAb	Monoclonal antibody
TTL	transistor-transistor logic	dAb	Detection or secondary antibody
PWM	Pulse-width modulation	cAb	Capture or primary

Chapter 1: Introduction

1.1 Background Information and Research Motivation

As the world's population grows, it is becoming more challenging to supply safe water to everyone. It is estimated that one-sixth of the world does not have access to freshwater resources [1]. As industry and technology grow, these restricted resources are even more threatened and polluted worldwide [2]. Therefore, due to extreme limitations and contamination, the water crisis has become an important global issue [3].

Contaminants pollute waters worldwide with geological or human-induced sources [4]. These sources are categorized into two broad types of point and non-point. Point sources include domestic and industrial dumping of wastes, whereas land runoff or chemical leaks, among others, shape non-point sources [5]. The contaminants could be further categorized into physical (e.g., microplastics), chemical (e.g., salts, heavy metals, pharmaceuticals, fertilizers and pesticides) and biological (e.g., bacteria, viruses, parasites) groups [3]. This thesis focuses on the development of technologies for screening salt and bacterial contaminations of water as two representatives of chemical and biological pollutants.

Water contamination risks and threats could be averted by taking appropriate measures, including rapid and sensitive water quality monitoring at public and end-user levels [2]. Here, regular monitoring of the water quality in swift, reliable, low-cost, and in-situ manners is crucial [6], [7]. Over the years, several detection methods have been established for measuring and monitoring water pollutants. For instance, electrochemical sensors that measure salinity based on conductivity are widely used in commercial CTD (conductivity, temperature, and pressure) instruments [8]. These devices are expensive and bulky while being either laboratory-based or requiring

complicated logistic processes to be used for on-site monitoring. Therefore, they are usually used for measuring the water salinity at sea salt levels (35,000 mg/L or 35,000 ppm) [8]–[10]. Industrial examples for biological contamination water safety monitoring are colony counting, PCR (Polymerase chain reaction), and ELISA (Enzyme-linked immunosorbent assay) methods [11]. These techniques should also be performed in a lab by trained professionals and require hours to days to complete, making them costly and time inefficient for rapid water testing [12].

Due to the cost, size, and rapidness limitations of established industrial methods, numerous studies have focused on developing point-of-need sensors for water quality monitoring. In this context, microfluidics-based methodologies are specifically promising because they allow for controlling and manipulating infinitesimal amounts of samples with fast reaction processes, compactness, field-deployability, disposability, parallelization for higher throughputs, lower costs, and higher process control [11], [13]–[15]. Microfluidic sensors could be categorized based on their signal measurement strategy into three categories: electrochemical [16]–[18], optical [12], [19], and mass-based [20], [21]. Numerous research studies using microfluidic techniques to detect different analytes have been presented, and the most important ones will be reviewed in the next chapter. These sensors show great potential for miniaturization of detection platforms that enable on-site detection and quantification of target analytes at a lower cost and faster response times than conventional techniques. Owing to these appealing characteristics of microfluidics-based sensors, the market of such sensors is rapidly growing and is projected to reach $36 billion by 2025 [22].

Despite the cost, size, and rapidness advantages of microfluidics-based sensors, the detection performance of these technologies is ordinarily inferior to those of laboratory-based methods. These detection limitations frequently inhibit commercialization and/or widespread adoption of microfluidics solutions. For example, the detection/quantification range of developed water

salinity microfluidic sensors does not accommodate the salinity range needed for drinking water quality control. In other cases, high sensor fabrication costs and long test times compromise sensors' low-cost and point-of-need characteristics. Besides, detection of certain contaminants and/or their quantification within ranges significant to high impact applications are not yet reported with microfluidic sensors and biosensors. This research is motivated by such shortcomings and aims to work toward developing a low-cost, simple, and swift sensing platform that allows inexpensive water surveillance that would have the potential to be used even in remote areas for warning water consumers or inspection officials and preventing future outbreaks.

1.2 Research Opportunity and Thesis Objective

There have been numerous research studies on developing various sensing devices. However, most of these technologies are not low-cost, require tedious fabrication steps, and might only be suitable for detecting one contamination type. Thereby, a single platform that can be tailored to detect several contaminants with low cost and straightforward fabrication steps is beneficial. The low-cost characteristic in this thesis solely refers to the cost of device materials and fabrication. The cost of accessories for operation and mass production should be considered in the future. In this thesis, such microfluidic sensor has been developed, enabling the detection and quantification of salt and bacteria in the drinking water, swiftly and reliably, with the potential to be used for on-site detection.

Towards the goal above, a microfluidic sensor in our lab was optimized to be used as a contamination detection and quantification platform. In particular, the sensor in this thesis was used to detect NaCl salt (as an ionic contamination) and *Escherichia coli* bacteria (as a biological contamination) in drinking water as two proof of concept examples of water pollutants. However, the sensing platform can be expanded in the future to detect other types of chemical or biological

contaminations. For the case of NaCl salinity, our goal has been to detect and quantify water salt content in very low detection ranges (typically below 120ppm), which is key to quality control of drinking water. Such detection and quantification ranges are not offered by any low-cost and rapid microfluidic-based sensor. In the case of bacteria detection, microfluidic-based solutions suffer from an intrinsic trade-off between sensitivity and sensor cost. As mentioned, our focus in this thesis has been to design an inexpensive microfluidic sensor for water contamination detection. Accordingly, the objectives of the thesis are defined as:

1. Development and optimization of a low-cost microfluidic water monitoring platform through experimental and numerical investigations with bimodal detection techniques.
2. Investigating the developed sensing platform's ability to detect and quantify water salinity in the range of drinking waters (below 120ppm) through electric conductivity measurements.
3. Investigating the developed sensing platform's ability to detect and quantify specific biological entities (*E. coli* bacteria) through both electric conductivity and photothermal radiometry measurements.

1.3 Thesis Organization

The first chapter of the thesis provides a general introduction to the research background, motivation, gaps and objectives.

The second chapter begins with an overview of conventional environmental monitoring techniques. It is followed by a review of the microfluidic environmental microfluidics sensors. We then discuss salinity and bacteria detection methods as two chemical and biological contamination

examples. Next, a comprehensive review of the developed microfluidics detection platforms for salinity and bacteria detection applications will be provided. Research gaps and questions will be highlighted in this chapter.

The third chapter describes our microfluidic sensor theory and design, experimental and numerical methodologies, signal acquisition techniques, and data analysis. Experimental methodologies include the fabrication process of devices, sample preparation protocols, and experimentation procedures.

The fourth chapter provides the achieved results and the following discussions. First, the microfluidics sensor's working principle and equivalent electrical circuit are discussed. Next, the primary sensing experimental results for the case of salinity detection are presented, followed by the development of a numerical model and optimization of an optimized sensing platform which is subsequently used for studies of objectives 2 and 3. Then, the experimental analysis of the optimized design will be discussed, and a comparison between the numerical and experimental findings will be drawn. Afterwards, the applicability of the microfluidics sensor will be studied for bacteria detection with electrical and photothermal methods toward the thesis's third objective.

The fifth and last chapter summarizes the presented thesis findings, discusses the limitations of the work, and provides suggestions and recommendations for future works.

Chapter 2: Literature Review and Research Gaps

This chapter will provide some basic information about sensor characteristics, followed by a review of conventional environmental monitoring challenges. Then, how microfluidics could help resolve these challenges will be reviewed. Later, the microfluidic environmental sensor types will be studied. Lastly, previously developed microfluidic salinity and bacteria sensors, as two selected contaminants in this thesis, will be reviewed.

2.1 Sensor Characterization

Sensors are defined as devices that produce an output signal when exposed to a biological, physical, or chemical measurand [23]. It is vital to understand sensor characteristics in order to fully comprehend sensing and how sensors that detect the same measurand can vary [23]. In this section, sensor terminologies and nomenclatures will be defined using their most frequent names, with alternate names referenced where appropriate.

2.1.1 Range

The range can be defined for both input and output values, and it is described as the minimum and maximum values of the sensor input or output. For the input, the range describes the sensor operating input parameters and conditions [26]. For the output, the range defines the measurand's maximum and minimum values that can be detected with an acceptable level of accuracy [26]. Span or dynamic range are also interchangeably used as alternatives to the range. Using the sensor without applying appropriate input ranges can compromise sensor integrity.

2.1.2 Calibration Curve

The calibration curve is a function that describes a relationship between the recorded signal and the measurand in the operating range of the sensor [23]. This correlation can be expressed as a

mathematical formula, a table of values, or a graph. The correlation should be independent of time and relate to the signal and measurand, usually expressed as a formula similar to (2-1).

$$S=F(x) \tag{2-1}$$

Where S is the recorded signal by the sensor and x is the measurand. As it is rarely possible for a calibration curve to be entirely defined by a single formula, functional approximations of the calibration curves are usually used [24]. For example, a statistical test like the goodness of the fit is performed to determine how well the functional approximation fits the sensor measured values.

2.1.3 Linear and Non-Linear Calibration Curves

The most straightforward calibration curves are defined based on a linear formula expressed as in (2-2).

$$S=A+B(x) \tag{2-2}$$

Where B is the sensor slope (sensitivity), and A is the sensor offset when no measurand is applied. Linear characterization allows plotting a straight line to relate measurand and corresponding recorded signals in the sensor's operating range [25]. It also shows that the sensitivity of the sensor is independent of the measurand value.

In contrast, some calibration curves cannot illustrate the relationship of the signal and measurand via a linear formula. Other mathematical functions such as logarithmic, exponential, power, or non-linear polynomials could be used as calibration curves [25].

2.1.4 Sensitivity

Sensitivity is the amount of change in the output as a result of one unit change in the input. An ideal and straightforward sensor should have a significant and constant sensitivity [26]. For the

case of linear calibration curves, the sensitivity would be the slope of a straight line and constant throughout the detection range. If the sensor is non-linear, the sensitivity will vary through the sensor span and can be calculated by taking the derivative of the calibration curve with respect to the measurand (dS/dx).

There are two critical concepts associated with sensitivity: dead-band and saturation. Dead-band is the range in which the output signal remains unchanged (and usually zero) while the input signal varies. The sensor is not responsive and sensitive in the dead-band range. On the other hand, saturation is reached when the sensor output can no longer show an increase with the input values [23].

2.1.5 Resolution

One of the most important parameters in sensors is resolution, defined as the smallest change in the input that causes a detectable alteration in the recorded output signal. The resolution determines if a sensor is suitable for a specific application or not. Low resolutions make the sensor incapable of detecting low incremental changes of measurand, and unnecessary high resolutions could significantly increase the sensor cost for a specific application [23].

2.1.6 Repeatability and Reproducibility

Repeatability is defined as a sensor's ability to generate and record the same output when the measurand and all experimental conditions are kept the same (e.g., repeated sensing of the same measurand with the same sensor in the same environmental conditions) [23]. Reproducibility, on the other hand, is the sensor's ability to generate and record the same output when the measurand is kept the same but an experimental condition has changed (e.g., when testing the same measurand with two replicates of a sensor).

2.1.7 Transient Effect and Settling Time

The settling response is an innate response of instrumentation systems when they are suddenly exposed to excitation. This effect usually dies out over time, and the device would reach an appropriate steady-state for measurement [26]. The time that takes the sensor to stabilize and reach a plateau is called settling time or response time [27].

2.1.8 Biosensing

In biosensing, the measurand is a biological entity usually referred to as the target antigen. Bioreceptors such as primary antibodies are usually used to t selectively capture the target antigen from the sample for detection and signal acquisition. Some sensors use labels for transduction that could be tagged to the captured antigen by secondary antibodies.

2.2 Conventional Environmental Monitoring

Environmental monitoring is crucial to safeguard the population and the environment from harmful chemicals and pathogens discharged into a range of media such as air, soil, and water [28]. As mentioned in the previous chapter, point and non-point sources of water contamination in underground and surface waters is a global issue that could be in biological, chemical, and physical forms. Phosphorous and nitrate are agricultural chemicals that soil cannot maintain and will be carried away by water in land runoffs [3]. Heavy metals pose severe fatal consequences at sufficiently high levels [29], [30]. Mercury (Ag), arsenic (As), and lead (Pb), among other heavy metals, pollute water as a result of uncontained industrial or domestic activities [30]. Salinity pollution like excessive sodium chloride leaves several outcomes that include perturbation in osmosis regulations and extinction of some biological species [4], seed germination prevention in soil [5], and various health threats to humans, primarily through drinking waters [30]. Biological contamination results from discharging animal/human excreta and organic wastes in water [31].

Bacteria, viruses, parasites, and protozoa are among biological contaminations, and in some species, even a few cells can cause gastrointestinal diseases or even mortalities [3], [32].

Traditional contamination monitoring entails invasive sample collection in the field followed by assessments in centralized facilities. In this approach, lengthy delays can cause chemical, biological, and physical changes in the sample that renders the results unreliable and the method itself unacceptable [30]. Therefore, rapid detection and quantification of the contaminants on-site is one of the best preventative measures, yet a key technological challenge in environmental monitoring [30]. As two important chemical and biological contaminant examples, we will overview NaCl salt (ionic) and bacteria (solid biological) contaminations and conventional environmental monitoring procedures.

2.2.1 Conventional Monitoring of Salinity Contamination

Water salinity measurement is critical in water quality monitoring and surveillance to preserve water safety [33]. Sodium chloride (NaCl) is the dominant dissolved salt leading to water salinity. Uncontrolled salinity levels can have detrimental effects on human health, agriculture, industry, and the environment [34]. Salt concentrations of water sources are continually changing due to global warming, human exploitation of ecosystems, and waste discharge into the environment [35]; yet, exceeding certain salt thresholds could cause pernicious consequences for human health and the ecosystem. These outcomes include perturbation in osmosis regulations and extinction of some biological species [36], seed germination prevention in soil [37], algal blooms increase in water bodies [38], and various health threats to humans, primarily through drinking waters [39].

Sodium plays a vital role in maintaining the osmotic pressure of the human body fluid and preventing excessive fluid loss. However, high sodium levels in the body could cause hypertension, cardiovascular diseases, renal diseases, and Meniere's disease [39], [40]. High blood

pressure alone is the leading cause of death and the second major cause of disability in children worldwide [41], [42]. According to the world health organization (WHO), acceptable salt intakes are recognized to be 5 g/day and 500 mg/day for adults on regular and sodium-restricted diets, respectively [43]. Canada's national health and welfare department requires a salt limit of 20 ppm on drinking water to maintain a sodium-restricted diet, assuming a daily water consumption of 1.5 litres [44].

Sodium levels in Canadian drinking water supplies vary seasonally and geographically [40]. The primary sources of water include tap water, groundwater, and surface water with sodium levels in the ranges of 0.3-242 ppm [45], 6-130 ppm [46], and 1-300 ppm [47], respectively. More than 75% of 2100 studied water supply cases in the U.S. had sodium concentrations below 50 ppm [48]. Salinity levels within these low limits must be monitored frequently, rapidly, and preferably specific to the salt type to prevent drastic effects on humans and the ecosystem.

According to Health Canada, there is a maximum acceptable concentration of none per 100 mL of *E. coli* in drinking water [49], which is a target for other pathogenic entities too. Thereby, accurate detection of biological contaminants with limits of detection as low as single cell per milliliter of drinking water is required. There are several well-established methods for measuring water salinity, among which measuring the electrical conductivity of water remains the most prevalent [8], [50]. Most of the current conductivity-based salinity sensing technologies are restricted to measuring high salt levels at the scale of seawater salinity (35,000 ppm) and/or are expensive, bulky, and not suitable for on-site drinking water NaCl monitoring [8], [10], [51]. For instance, ion chromatography is one of the methods that allow separation and quantification of ionic contaminants through conductometric detection but is mainly lab-based. Other electrochemical sensors that measure salinity based on conductivity, and are widely used, are commercial CTD

(conductivity, temperature, and depth) instruments [8]. As seen in *Figure 2-1*, these types of equipment require a logistical arrangement for on-site detection. *Figure 2-1* depicts two examples of the in-situ measurement equipment developed for seawater salinity monitoring using the CTD method.

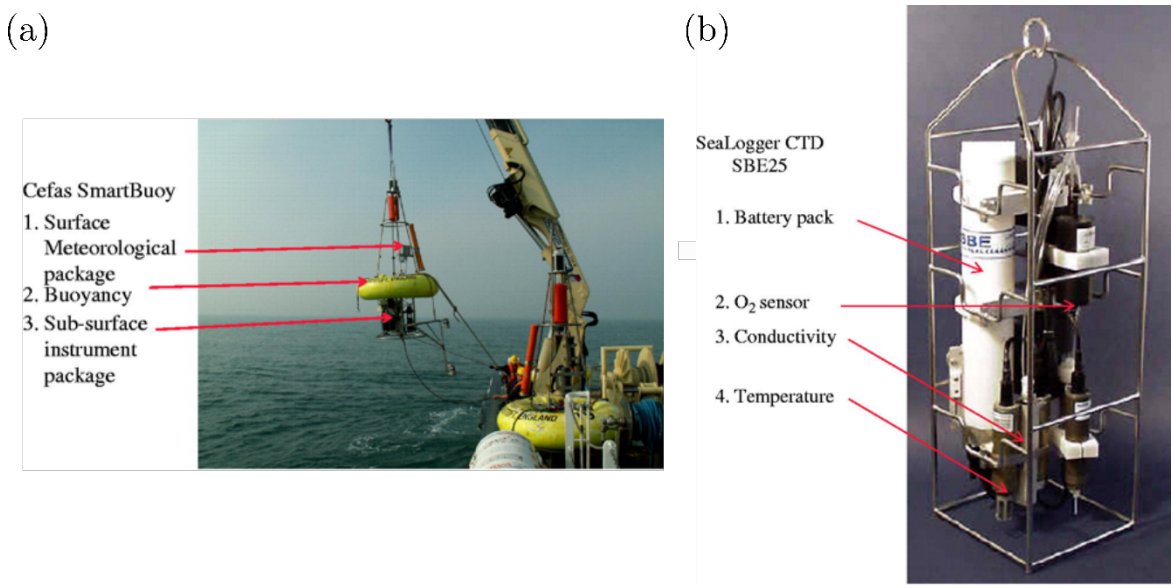

Figure 2-1. Two examples of CTD-based in-situ equipment used for monitoring seawater. (a) Cefas SmartBuoy [52] *and (b) SeaLogger CTD SBE25* [53] *are depicted that require logistical arrangement and trained personnel for the monitoring process. © Emerald Publishing Limited all rights reserved.*

Another salinity monitoring method is optical detection. Several fiber optic sensors [54]–[58] based on interference, fiber Bragg grating, long-period grating, and surface plasmon resonance have been proposed for on-field salinity measurement. Rahman et al. [54] reported a fiber-based optical method for detecting different sodium chloride concentrations. The sensor working principle was based on the change in refractive index when the fiber was immersed in salt samples, leading to quantification of salinity from measured transmission optical intensities (*Figure 2-2*a). Zhao and colleagues [55] developed an optical seawater salinity and temperature sensor based on beam deviation as the refractive index changes (*Figure 2-2*b). In another effort by Rahman et al.

[56], salt concentrations in deionized water were quantified as a 594 nm He-Ne laser was transmitted into the samples and the absorbance was measured (*Figure 2-2*c). Meng et al. [57] proposed an optical fiber laser consisting of a no-core fiber sandwiched by two single mode fibers leading to multimode interference effects (*Figure 2-2*d). Hussain et al. [58] developed a smartphone-based optical fiber sensor to detect salinity through attenuation and evanescent field absorption when the light passed a U-bent detection fiber region that was uncladded (*Figure 2-2*e).

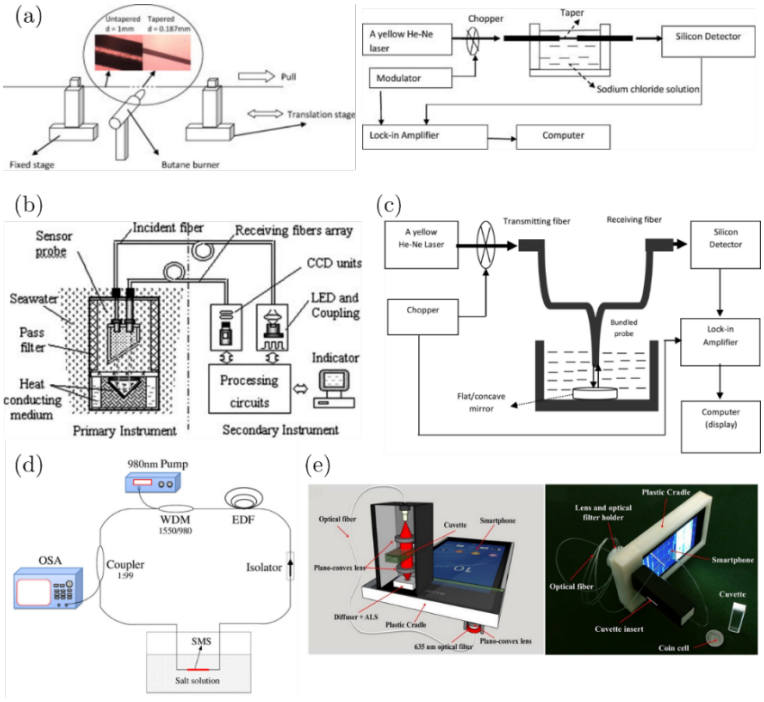

Figure 2-2. Select developed optical salinity detection devices are shown. (a) Rahman et al. used a tapered optical fiber sensor to detect salinity based on the change in recorded transmission [54]. *Reprinted with permission from Elsevier. (b) Zhao and coworkers measured beam deviation as the light passed through seawater to quantify salinity* [55]. *Reprinted with permission from Elsevier. (c) Rahman et al. measured absorbance changes as the light was transmitted into a salt sample and was reflected by a mirror and received at the detector to measure salinity* [59]. *Copyright © 2012, IEEE (d) Meng et al. used multimode interference effect by an optical fiber made with a no core fiber sandwiched with two single-mode fibers to record attenuation by salt samples* [57]. *Copyright © 2014, IEEE (e) Hussain et al. made a smartphone-based detector with a U-bend uncladded optical fiber as the detection region to measure salinity through evanescence absorption in saline samples* [58]. *Reprinted with permission from Elsevier.*

While these optical sensors have reported the lowest detected salt values of 2 ppm [60], 4 ppm [37], 6.7 ppm [55], 10 ppm [61], and 40 ppm [62], they lack the required resolution to quantify salinity within drinking water ranges. This fundamental limitation is rooted in insensitivity of the refractive index to small changes in salinity. That is, a 1,000 ppm change in salt commonly causes an infinitesimal optical path length deviation [33]. This intrinsic characteristic makes the optical sensors not sensitive enough for reliable quantification of salt at drinking water levels [58]. In addition, optical sensors usually are complex, laboratory-based, and costly due to their reliance on precision optical elements (e.g., prisms) or delicate fiber optics. Optical sensors, however, can detect non-ionic salts such as silica [63].

2.2.2 Conventional Monitoring of Bacteria Contamination

Water and foodborne infectious diseases pose a severe threat to public health worldwide. According to WHO, there are more than 600 million cases of pathogen infection every year across the globe [64]. In Canada, 1 in 8 Canadians contacts pathogenic illness every year [65]. This puts an economic burden on governments in both developing and developed countries. WHO estimates that unsafe foods cost low- and middle-income countries about USD $110 billion per year [66]. According to a USDA report in 2013, the annual cost of pathogenic diseases is more than USD 7 billion due to food recalls. In this section, conventional methods for water safety surveillance for biological detection and monitoring will be reviewed.

There are several well-established methods and techniques for pathogen detection in the food and water safety industry (Figure 2-3a). Colony counting in microbiological culture stays the ‘gold standard’ method in the water and food safety industry [67]. This method was established by the Food and Drug Administration (FDA) for bacteria detection and is consisted of sample enrichment, plate culturing, and counting the bacterial colonies in the culture plates after prolonged sample

incubation at 37ºC. It also introduced a unit for expressing bacteria counts, which is colony-forming unit per mL of the sample (CFU/mL) (*Figure 2-3*b) [68], [69]. This method should be performed in a lab by trained professionals and takes 2-5 days, making it costly and time inefficient [70]. Enzyme-linked immunosorbent assay (ELISA) is another pathogen detection technique that relies on the binding of antibody-antigen complexes (Figure 2-3c) [71]. The ELISA methods have specific detections, but a process of pathogen enrichment is sometimes required for the testing [72]. For instance, a commercial product based on ELISA by Solus Scientific Testing Solutions allows for detecting (not quantifying) *Salmonella, Listeria,* and *E. coli O157* in 24-36 hours [73]. Polymerase chain reaction (PCR) is another pathogen detection method that is based on the amplification of nucleic acids (Figure 2-3d) [74]. It can amplify a single nucleic acid into millions of similar copies through a thermal cycling procedure that involves DNA denaturation, annealing, and extension [75]. PCR has drawn attention in both the water and food safety industries. It reduces the detection time to 24 hours and less with high sensitivity, high specificity, and low detection limit [76]. PCR can be modified for quantification but involves additional steps which adds to complexity, cost, and turnaround time of the method. Another drawback of PCR is that the dead and live cells cannot be distinguished, and false-positive results could occur [16], [77]. The long times required for the tests and methods' dependence on laboratories and trained personnel render them unsuitable for applications needing field-deployability and rapidness.

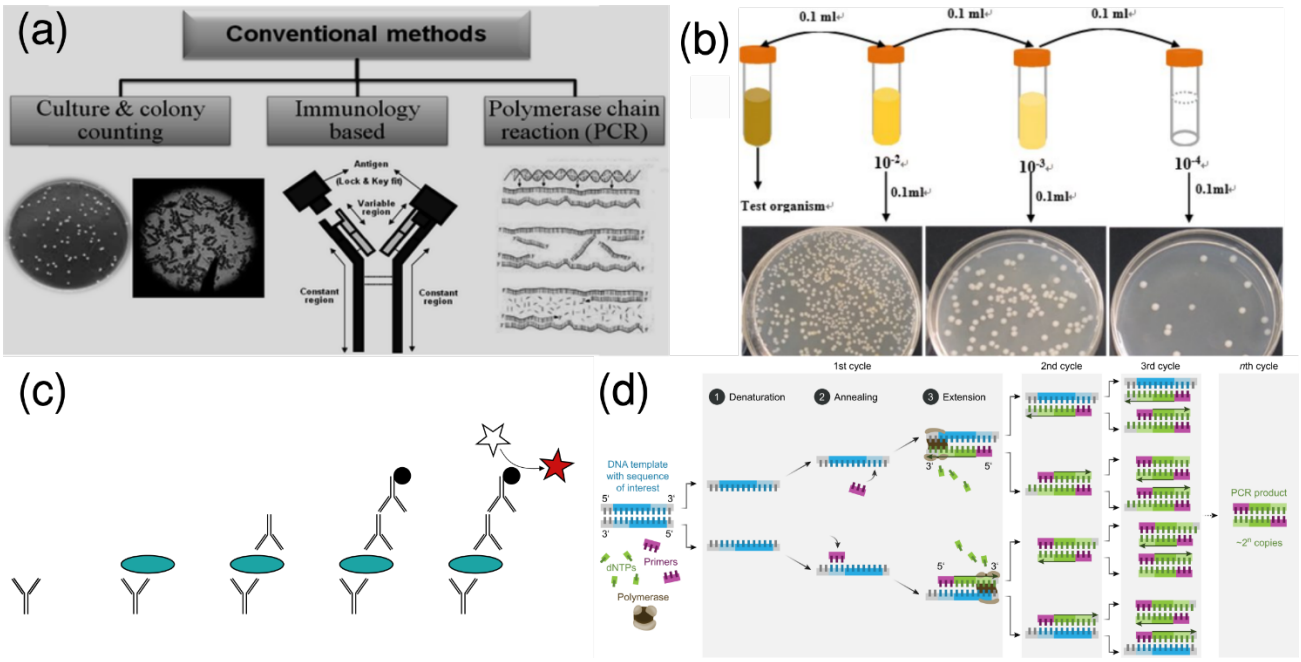

Figure 2-3. Conventional pathogen detection methods. (a) Three common and standard methods to detect pathogens are colony counting, polymerase chain reaction (PCR), and enzyme-linked immunosorbent assay (ELISA) [78]. *Reprinted by permission from Springer Nature. The working principles of (b) colony counting* [79] *Reprinted with permission from Springer Nature, (c) ELISA* [80] *and (d) PCR* [81], *are illustrated.*

2.3 Microfluidics-based Environmental Monitoring

Microfluidics in the context of environmental surveillance offers the promise of inexpensive, reliable, and precise water analysis that can be used to evaluate samples in the field or *in situ* [82]. Thus, the results would be available sooner, at a lower cost, and contamination would be minimized by eliminating the need for samples to be transported to labs [82]. Microfluidics sensing and detection systems can be categorized based on their type of sensing into three main categories electrochemical, optical, and mechanical, which are further discussed below [83]–[85].

2.3.1 Electrochemical Sensors

Electrochemical sensors are sorted based on their detection mechanism into four categories of potentiometric (potential), amperometric (current), voltametric (voltage), and conductometric.

Potentiometry is a technique for passive measurement of the potential of a solution between two electrodes without affecting it (no current or voltage applied) [86]. Voltammetry uses a three-electrode setup to apply a variable potential to an electrode surface and measure the associated current [87]. In amperometry, a constant potential, in contrast to varying potential in voltammetry, is applied, and the resulting current is measured [88]. Conductometry involves measuring sample conductivity according to Ohm's law (V=RI), usually through direct current measurement [89].

Electrochemical reactions at the analyte and electrode interface produce an electrical signal that is measured based on changes in either current, voltage, or electric potential [89], [90]. Conventional electrochemical sensors generally contain three electrodes: a reference electrode, a counter electrode, and a working electrode [89], [90]. The working electrode is the cathode, and the counter electrode closes the circuit while the reference electrode measures the potential of the working electrode without passing any current through it. In the case of an oxidation reaction at the working electrode, there would be an equal reduction reaction at the counter electrode, while there would be no current flow between the reference and working electrodes due to high input impedances, which enables monitoring potential changes at the working electrode. This monitoring capability through the reference electrode would not be obtained in two-electrode systems.

In this context, microfluidics allows for miniaturization and the potential for on-site detection. The recorded signals inside the microfluidic electrochemical sensors could be used to quantitatively determine the concentration of contaminants in the sample [90]. Microfluidic electrochemical sensors have shown to be a promising candidate for the next generation of point-of-care sensors owing to their high sensitivity, low cost, and portability[3], [91], [92]. However, there are some limitations to some of the developed paradigms, such as susceptibility to the environment, time-inefficiency, and relatively complex fabrication processes that increase the cost [3], [90].

2.3.2 Optical Sensors

Optical sensors are widely used for analysis and detection in different applications ranging from medical therapeutics and diagnostics [93]–[96] to environmental [95], [97], food, and water analysis [98], [99]. Optical biosensing can be categorized into direct and indirect analyte detection methods [90]. Indirect methods include using labelling probes like chemiluminescence and fluorescence [100]. In contrast, direct detection methods include, surface plasmon resonance (SPR) [101], fiber optics-based [102], UV absorption [103], surface-enhanced Raman Scattering (SERS) [104], and planar optical waveguide based [105] sensing modalities.

In optical systems, change in concentrations of the measurand alters certain attribute of light (e.g., power, polarization) that allow detection and quantification of measurands. For instance, intensity readouts of fluorescent images from a biosensor could be correlated to the concentrations of fluorophore-tagged bacteria. [90], [106]. Despite high sensitivity and reliability, the need for bulky and lab-based instruments for some methods, the necessity of surface modification, or high sensitivity to the environment are among the shortcomings of optical biosensing [90].

2.3.3 Mass-based Sensors

Mass-based or gravimetric detection is another type of sensing that include surface acoustic wave (SAW) [107], quartz crystal microbalances (QCM) [108], and microcantilever-based (MCL) [109] techniques. These methods mainly rely on the changes of mass due to contamination at the interface of the electrodes that influence their electrical signal transduction. The output electrical signal would be compared to the input frequency, phase, or amplitude to determine changes with respect to reference input parameters toward detection and quantification. Although very sensitive, these micro- and nano-mechanical methods require isolated laboratories to prevent environmental

noises such as oscillations and vibrations that make them unfitting for in-situ and on-field detection [90].

Despite the drawbacks in question, microfluidics-based detection platforms are promising candidates to enable detection in rapid, low-cost, and on-site paradigms. They have shown the capability of detecting infinitesimal amounts of various water contaminations [3]. Here, our focus will be on NaCl and bacteria detection microfluidic sensors (as two applications of our presented sensor), and literature will be comprehensively reviewed.

2.4 Salinity Microfluidic Sensors

Our literature search has shown that there are few efforts to detect salt using microfluidic platforms. Nevertheless, microfluidic devices are promising because they allow for low-cost mass production of compact and field-deployable salt sensors that would require a short time and a small sample volume for measurement [110]. On a microfluidic device, Sun et al. [112] used grayscale readouts from a Schlieren microscope to detect salt concentration changes in water. As shown in **Error! Reference source not found.**, saline water samples close to the seawater salt values were infused into a T-microchannel, and optical readouts were recorded by a microscope. They successfully detected saline samples with salt concentrations ranging from 10 to 40 g/kg (10,000-40,000ppm). This method was restricted to seawater samples as changes at lower salt concentrations did not change the visual readouts. It also required lab-based equipment and free space laser that could not be used for on-site detection.

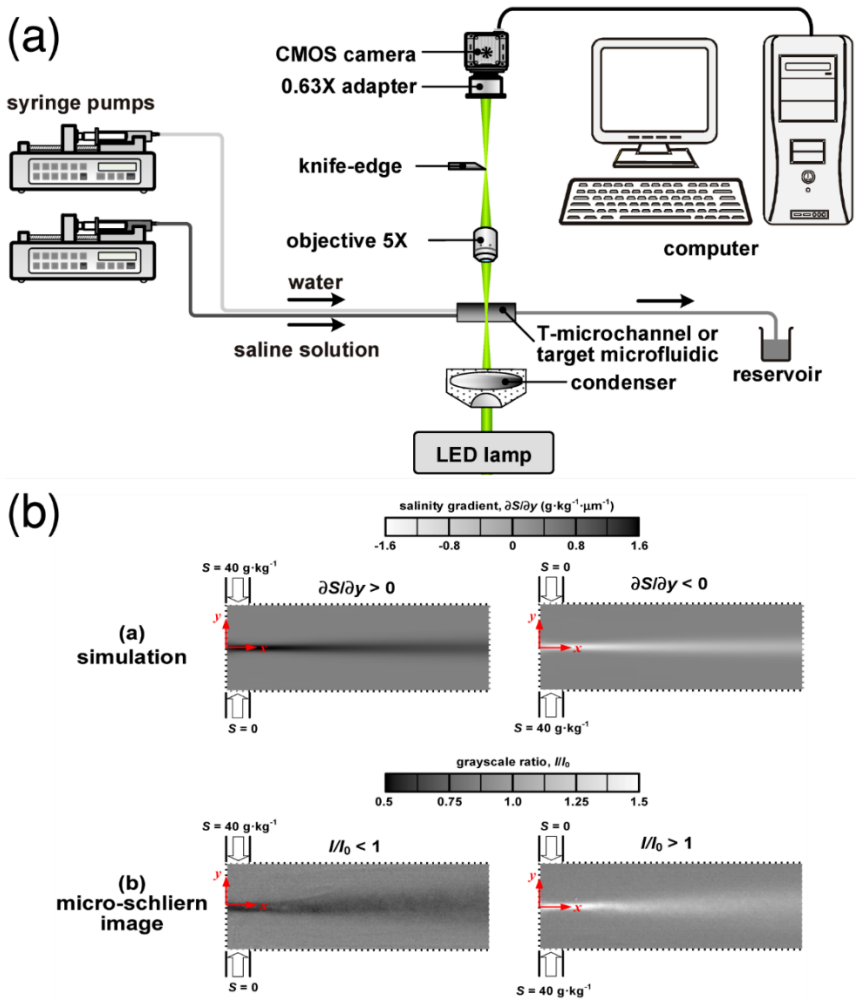

Figure 2-4. Experimental setup and salinity detection of Sun et al. [111]. *(a) Salinity samples were infused in a T-microchannel, and salinity gradients changed the optical readout as shown in (b). Creative Commons Attribution 4.0 International (CC BY 4.0).*

In another effort, Xie et al. [62] presented a salt sensor based on integrating microfluidics and optical fiber-assisted Mach-Zehnder interferometry. As in Figure 2-5a, salt samples were flown into the microchannel where the microfiber was located. When the light passes through the tube, it is divided into two parts where one half-beam goes through the NaCl sample with different refractive indices, and the other goes through the microfiber. The difference in optical path length of the two half-beams would be correlated to the NaCl concentration inside the microchannel. The

study showed a high sensitivity for detection in a 40-31,000 ppm range of NaCl but was inept below 40 ppm, which is needed in the drinking water application.

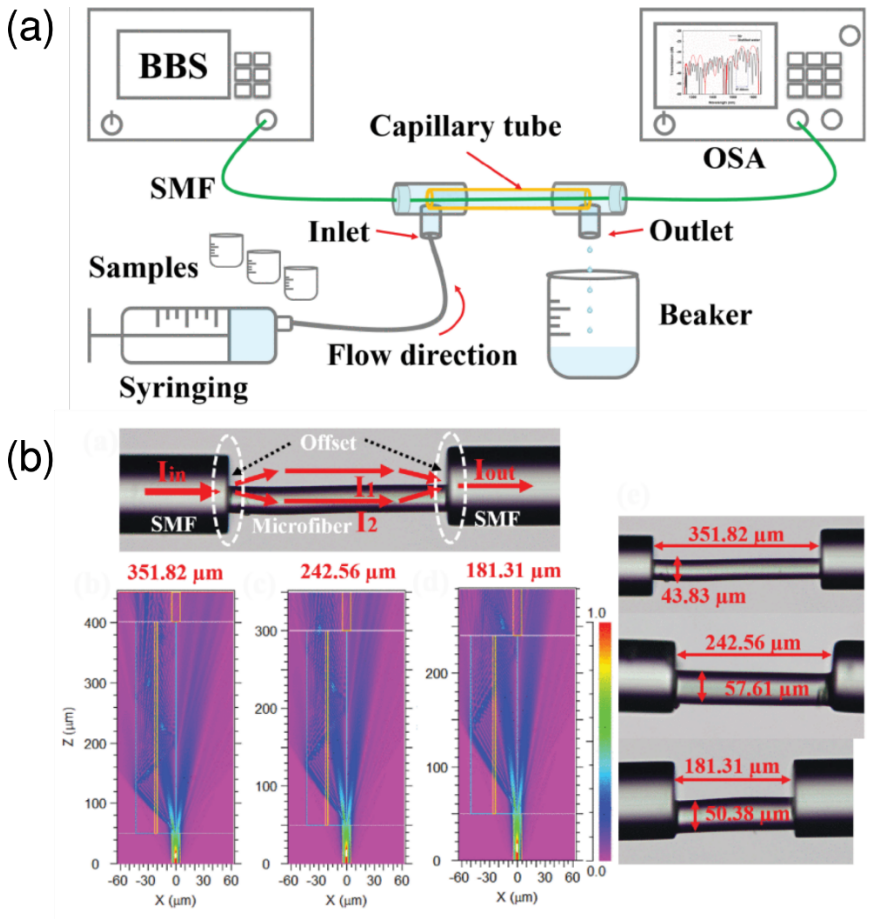

Figure 2-5. Experimental setup schematic and microscopic image of developed microfibers with different diameters and cavity lengths by Xie et al. [62]. *(a) A schematic of the experimental setup is depicted. (b) two-path lines of the light through salinity sample and microfiber are illustrated. Various microfiber lengths and diameters were developed and simulated. Copyright © 2018, IEEE*

In another study, Kim et al. [112] developed an integrated temperature and conductivity sensor for monitoring the product water of reverse osmosis desalination. As illustrated in Figure 2-6, the developed sensor consists of three components of a power board for AC signal generation, a sensing microchannel, and a signal acquisition board. The conductivity and temperature were measured through Cu/CuNi metal films and four gold electrodes, respectively, situated on a glass

substrate. The handheld microfluidic device was designed and calibrated to detect conductivities in the range of 0.33-14.64 mS/cm, corresponding to relatively high salt levels of 165-7,320 ppm, which is more relevant for seawater detection and is not suitable for drinking water monitoring.

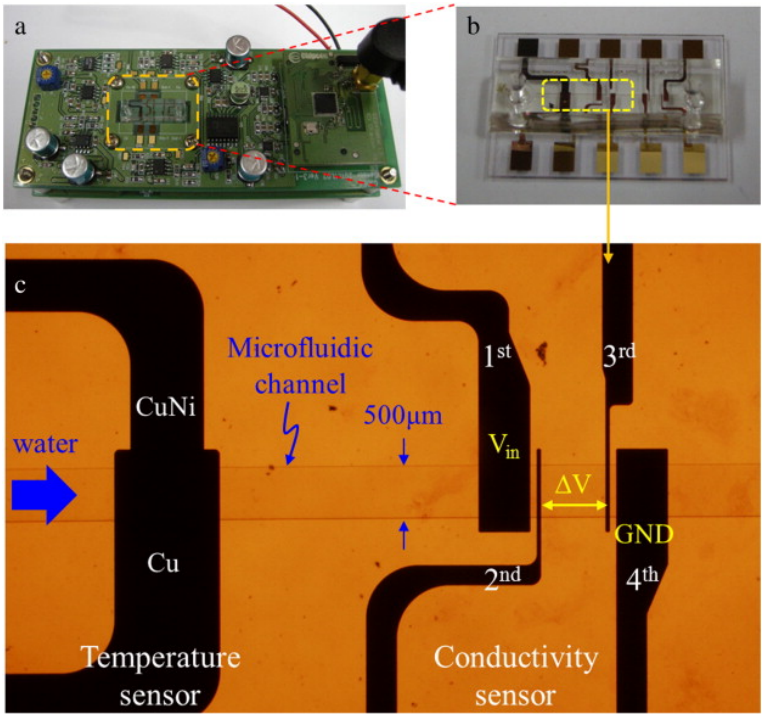

Figure 2-6. Integrated microfluidic conductivity and temperature sensor developed by Kim et al. [112]. *(a) The sensor board and (b) the microfluidic device is depicted. (c) the integrated microfluidic sensor is shown under a microscope. All electrodes are placed on a glass substrate. Temperature is measured through two thin metal films of Cu and CuNi. The conductivity sensor is made of four gold electrodes. Reprinted with permission from Elsevier.*

Based on our reviews, the need to sensitively measure low water NaCl ranges of 1-120 ppm (aka. drinking water salt range) is not addressed by the existing microfluidic technologies. Another significant gap in this area is the lack of specificity in NaCl detection which requires future work toward its resolution. Available sensing paradigms are usually total conductivity sensors or optical devices that cannot differentiate different salts in the samples. Other issues like expensive

fabrication procedures and the need for lab-based or costly auxiliary equipment compromise these sensors' aim to enable low-cost on-site detection for continuous water quality surveillance.

2.5 Bacteria Microfluidic Biosensors

Bacterial microfluidic biosensors mainly rely on immunoassay detection and could be categorized based on their signal measurement technique into three categories: electrochemical [16]–[18], optical [12], [19], and mass-based [20], [21] (Figure 2-7). Electrochemical and optical methods are better candidates for on-field detection as they are less prone to environmental noises (errors). They can also be augmented by receptors and/or labels for selective sensing/detection. In the following sections, biosensors will be reviewed based on these categorizations.

2.5.1 Choice of Bioreceptor

Based on the type of target analyte, a suitable recognition element can be chosen among antibodies, enzymes, DNA, phages, and aptamers (Figure 2-7). These recognition elements are employed on the surface of sensing structures to capture specific targets and convert these binding events into sensor outputs using various transduction mechanisms. Antibodies are widely employed for bacteria and pathogen detection and proved to bring about fast detection to biosensing platforms. As the antibodies are mainly specific to the target analyte, they can detect pathogens in samples with other components [113]. Aptamers, as one of the competitors of antibodies, are nucleic acids with one strand that has shown high specificity to detect different analytes, including proteins [114], [115], pathogens [116], [117], toxins [114], and whole cells [118]. Enzymes are catalytic proteins that improve chemical reaction rates by 5 to 17 orders of magnitudes compared to chemical reactions without enzymes [119]. Enzymes mainly play the role of catalyst for reduction-oxidation (redox) reactions in biosensing applications [90]. As a result of such reactions, measurable parameters like ions, electrons, protons, light, and/or heat can be produced [120].

There are advantages and disadvantages in employing each of the mentioned biological recognition elements that should be considered when selecting them for specific microfluidics applications. Antibodies [121], [122] are only suitable for large targets like bacteria or pathogens, whereas aptamers [123], [124] can be applied for a variety of sizes [90]. Besides, aptamers would be cost-efficient and stable, whereas antibodies used for indirect detection or labelling could increase the cost of the device [90]. However, aptamers weakly bind to analytes and have shown higher toxicity and faster excretion than antibodies [90]. Enzymes [125], [126], on the other hand, could lose their functionality as a result of immobilization and are only suitable for detecting small targets such as lactate, urea, and glucose. On the bright side, however, enzymes have shown to be highly selective and specific and are an inseparable part of detections based on oxidation-reduction reactions [90].

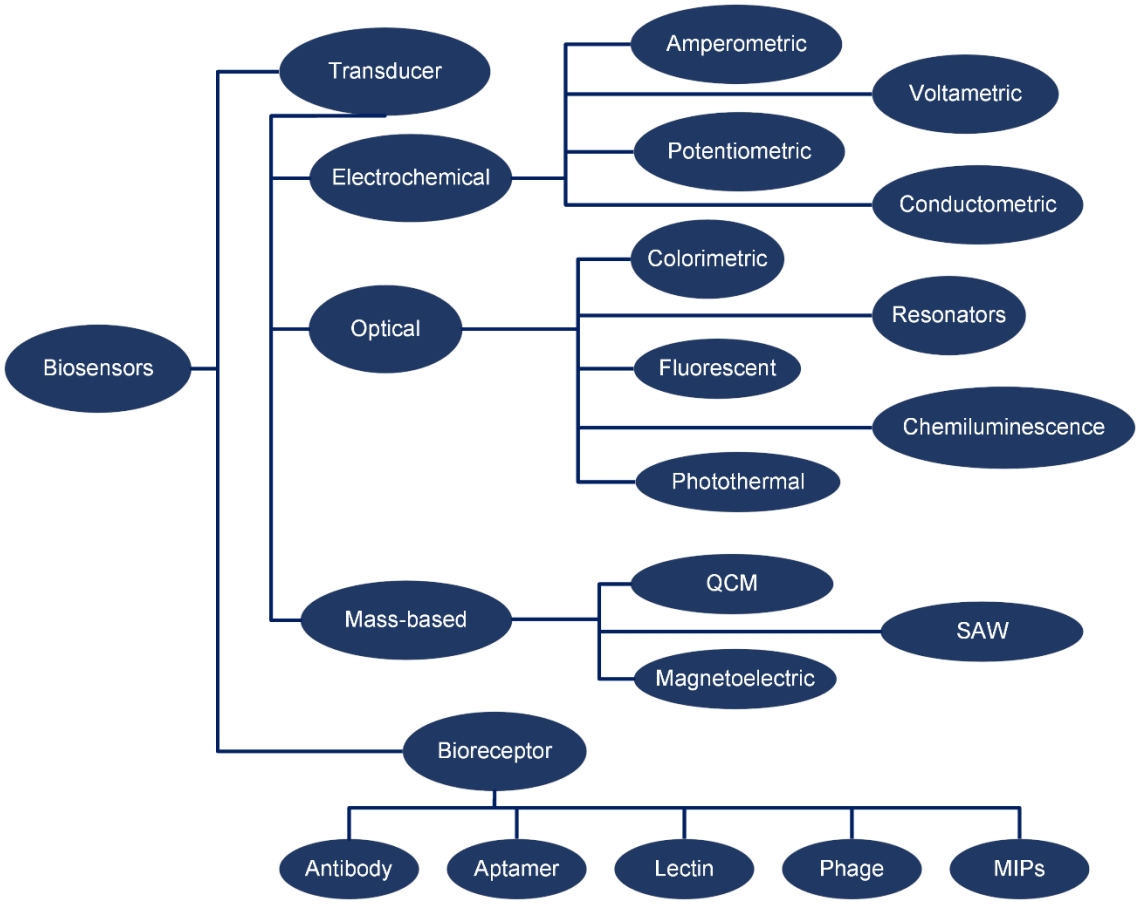

Figure 2-7. Biosensor categorization based on transducer types and bioreceptor.

2.5.2 Electrochemical Microfluidic Biosensors

The working principles of microfluidic electrochemical sensors are similar to the macroscale ones described in section 2.2.1, with the detection cells and electrodes being miniaturized into micro-scale dimensions and devices. These biosensors use alternating current (AC) or direct current (DC) as a probe to investigate bacteria concentrations in the sample based on current, voltage and or resistance. These sensors are less prone to environmental noise, and their integration with electronic signal acquisition equipment is more straightforward than other techniques. Other advantages include relatively shorter detection times and lower costs.

In a study carried out by Dastider et al. [127], an electrochemical biosensor was developed by an electrode array on the bottom of a fluidic channel. A comparison study was performed between microfluidic and non-microfluidic versions of the same device (Figure 2-8a). The biosensor provided the results after incubation for 3hr with non-enriched samples. The microfluidic biosensor's limit of detection (LOD) was reported as 10^3 CFU/mL. In contrast, the non-microfluidic device had a LOD of 10^4 CFU/mL, indicating that the microfluidic biosensor was more sensitive.

Yao et al. [128] presented a microfluidic biosensor to detect *E. coli O157:H7* using streptavidin-biotin chemistry (Figure 2-8b). First, magnetic nanoparticles (MNPs) were conjugated with streptavidin, and polyclonal antibodies were tagged with biotin to produce antibody tagged MNPs (immune MNPs). These particles were added to the bacteria sample to selectively attach to the target antigen so that the magnets would separate them in the microdevice. Next, gold nanoparticles (AuNPs) were coated with urease and secondary antibody to sandwich the bacteria captured with the immune MNPs. Lastly, impedance changes at the electrode surface due to hydrolysis of urea to produce ammonium carbonate was measured and correlated to bacteria count with a reported LOD of 12 CFU/mL.

Hou et al. [129] fabricated an electrochemical microfluidic sensor and maintained two electrodes in the inlet and outlet to measure the voltage through the microchannel (Figure 2-8c). They sandwiched the bacteria in samples with antibody-modified magnetic nanoparticles (Ab-MNP) and enzyme-tagged polystyrenes to produce magnetic-enzymatic bacteria. Afterward, the sample was infused into the microchannel, and the bacteria complexes were trapped using a magnet. Then, hydrogen peroxide was injected, and an oxygen gap was formed because of catalysis with enzymatic bacteria. The formation of the oxygen gap would result in a decrease in voltage levels,

and the recorded voltages would correspond to bacteria counts. A limit of 33 CFU/mL detection between tested counts ranging from 3.7×10^1 CFU/mL to 3.7×10^6 CFU/mL was achieved within 2 hours.

Wang et al. [130] proposed a pathogen detection method based on the reduction of silicon dioxide (SiO_2) nanoparticles covered with manganese(IV) oxide (MnO_2), also known as SiO_2@MnO_2, that would change the biosensor's impedance (Figure 2-8d). This technique used antibody-modified magnetic nanoparticles (Ab-MNPs) to separate the sample's target bacteria (*S. typhimurium*). Next, SiO2@MnO2 nanocomposites, conjugated with a secondary antibody, were added to the complex and the reduction of the nanocomposite to Mn^{2+} was achieved by adding H_2O_2. The resulting bacteria sample was poured on interdigitated electrodes, and the impedance was measured. After normalization to the baseline, the biosensor's calibration curve was established. The enrichment was performed over 45 minutes, and the obtained LOD was 21 CFU/mL from milk samples.

In a similar effort by Altintas et al. [131], an automated electrochemical biosensor was developed based on oxidation/reduction reactions of HRP and TMB (3,3′,5,5′-tetramethylbenzidine). This study used a gold chip to covalently bond primary antibodies to selectively capture the target antigen from the bacteria sample (Figure 2-8e). Afterward, a secondary antibody tagged HRP was used to sandwich the captured pathogen. Lastly, TMB was infused to have an oxidation reaction that released an electron that the electrodes could measure. They were able to measure a range of 10^4 to 10^9 CFU/mL with a LOD of 50 CFU/mL.

Despite the promising achievements discussed in this section, a few drawbacks remain for the electrochemical biosensors. Biosensors that illustrate low detection limits often have multi-step and off-chip detection or involve high fabrication and detection costs. Sensors with lower costs usually have high detection limits or require antigen amplification that would increase detection

time and complicate the process. Therefore, a trade-off of sensitivity and cost should be considered to acquire an optimized condition for each application.

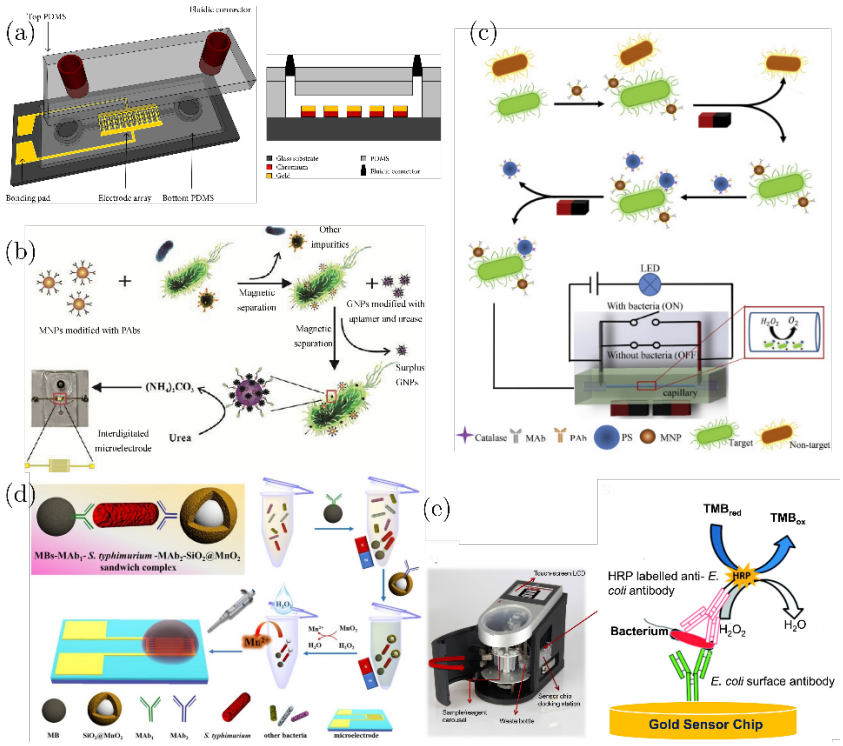

Figure 2-8. Electrochemical microfluidic biosensors. (a) Dastider et al. [127] *developed two interdigitated electrodes on glass for pathogen detection. Copyright © 2015 Shibajyoti Ghosh Dastider et al. Attribution 3.0 Unported (CC BY 3.0) (b) Wang et al.* [130] *employed MNPs coated with pAB for magnetic separation of target bacteria antigens and used aptamer-tagged GNPs to detect urea enzymatic reactions. Reprinted with permission from Elsevier. (c) Hou et al.* [129] *used a similar magnetic separation. The trapped particles in the middle of the channel reacted with H_2O_2, and an O_2 bubble was formed that changed the electrical readings between the two electrodes. Reprinted with permission from Elsevier. (d) Yao et al.* [128] *also took advantage of magnetic separation and urea enzymatic reaction to measure bacteria count. Reprinted with permission from Elsevier. (e) Altintas et al.* [131] *developed a fully automated device to track electrochemical activities due to TMB and HRP on a gold chip. . Reprinted with permission from Elsevier.*

2.5.3 Optical Microfluidic Biosensors

Optical biosensors are designed to detect the interaction between the target analyte and immobilized-on-the-surface biological receptors (designed to bind specifically to targets) that

produce an optical change. This change can be recorded as a measurable signal that could be translated to quantify the target analyte based on its concentration. There are a variety of optical biosensors that could be user-friendly for binary results or have superior sensitivity for accurate results. Optical biosensing methods are adaptable for simultaneous detection of multiple analytes with low quantities in testing samples [90], [132]. Optical biosensors fall into several sub-categories of colorimetric, resonators (surface plasmon resonance/SPR and surface-enhanced Raman spectroscopy/SERS), optical waveguides, chemiluminescence/fluorescence, and photothermal approaches.

2.5.3.1 Colorimetric Biosensors

This approach does not need high-end analytical instruments [133], provides a binary result, and could be coupled with colour intensity measurement for quantification. Bacteria or other pathogens in the sample would change the colour of a reaction solution, and the result can be easily observed with the naked eye. Integration of microfluidic and colorimetric methods has also been widely used recently [134], [135]. Among the available techniques, paper-based microfluidic was mainly used for colorimetric detections. It is inexpensive, suitable for in situ detection, disposable, and easy to work with [136]. In this regard, Sun et al. [135] presented a microfluidic paper-based analytical device (μ-PAD) that consisted of filter paper and polyvinyl chloride (PVC) pad (**Error! Reference source not found.**a). The μ-PAD contained enzymes specific to *Cronobacter spp*, and upon exposure to these bacteria, the pad's colour would change from colourless to blue when the bacteria is inoculated for 10hrs. The colour change happens when α-glucosidase secreted from bacteria reacts with its specific enzyme of 5-bromo-4-chloro-3-indolyl-α-D- glucopyranoside (XαGlc) to release aglycone 5-bromo-4-chloro-3-indole which generates chromogenic groups in the presence of oxygen. Average grey intensity values from the optical images were used to

establish the sensor's calibration curve for various bacteria counts. The developed platform allowed bacteria detection on the μ-PAD with a LOD of 10 CFU/cm^2. In another effort, Jokerst et al. [137] fabricated a μ-PAD device with wax printed filter paper and operated based on the enzyme's colour change specific to the target antigen. When used in conjunction with the enrichment process, the technology enabled enrichment times of 12 hours or less, and counts in inoculated food could be detected as low as 10 CFU/mL (**Error! Reference source not found.**b). Low selectivity, lengthy detection time, and low sensitivity are the fundamental shortcomings of colorimetric detection.

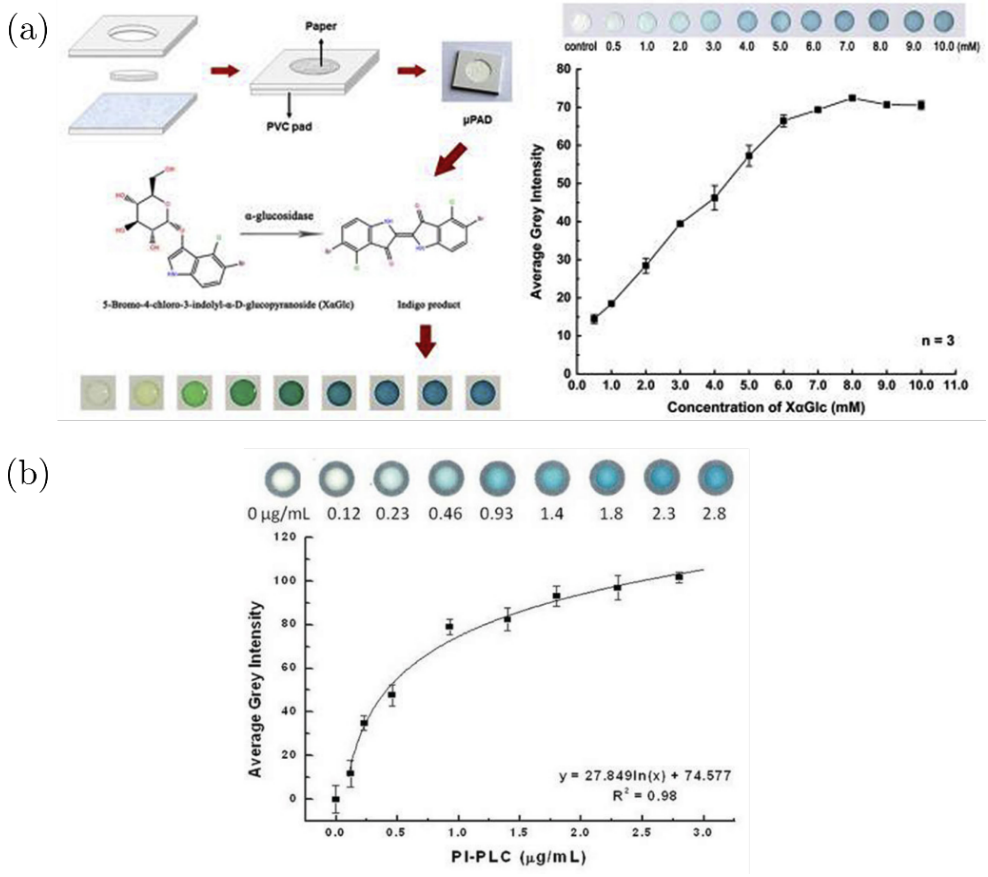

Figure 2-9. Microfluidic paper-based analytical devices. (a) Sun et al. [135] *developed μ-PAD for specific detection of inoculated bacteria in 10hr. Reprinted with permission from Elsevier. (b) Jokerst et*

al. [137] *presented μ-PAD for detection of multiple pathogens. Reprinted with permission. Copyright © 2012, American Chemical Society.*

2.5.3.2 Fluorescent biosensors

Fluorescent biosensors are analytical instruments that use the fluorescence effect, which happens when fluorescently tagged molecules absorb electromagnetic radiation, or fluorophores to detect biomolecules in biological samples noninvasively [138]. One of the following procedures is used to determine the generated signal: FI (changes in Fluorescence Intensity), FRET (Förster Resonance Energy Transfer), FCS (Fluorescence Correlation Spectroscopy), and FLIM (Fluorescence Lifetime Imaging) [139]. These biosensors have several advantages, including high sensitivity and readability [140], [141]. Compared to the colorimetric method, florescence detection has higher sensitivity [133]. Several studies recently combined microfluidic with fluorescent techniques to develop detection platforms with low cost for in situ detection [142].

In an effort for the detection of *S. Typhimurium*, Wang and colleagues [143] used CdSe/ZnS@SiO2-NH2 composite fluorescent nanoparticles (FNPs) as a fluorescent tag (Figure 2-10a). First, CdSe/ZnS quantum dots (QDs) were wrapped with SiO_2 shells. To capture bacteria, the shell was aminated by (3-Aminopropyl) triethoxysilane (APTES). The bacteria were chemically bonded to FNPs by glutaraldehyde crosslinker in a one-step and two-step method. Intensity measurement was performed under the microscope, and a detection limit of 3.3×10^2 CFU/mL was obtained with a linear range of 6.6×10^2 to 6.6×10^4 CFU/mL. To achieve better visualization, they added interdigitated electrodes to the microfluidic channel to produce positive dielectrophoretic force (pDEP) that captures and enriches the particles along the electrodes. The bacteria were chemically attached to FNPs by the amine groups on the bacterium. The amine group, however, is a shared quality among a large number of pathogens. Hence, this method did not allow for selective capture of target bacteria.

Kubo et al. [144] presented a microfluidic disk device for PCR amplification and detection of *Salmonella* by fluorescent tags produced by gene amplification. *Salmonella* cells were loaded on the system, and PCR was performed targeting the invA gene specific to the *Salmonella* strain (Figure 2-10b). The detection was performed by measuring the fluorescent signal obtained in the gene amplification technique. Magnetic nanoparticles (MNPs) tagged with anti-*Salmonella* antibodies were used to enrich the target antigen to optimize the process further. A LOD of 5.0×10^4 cells/mL was obtained, and the whole process took 6hr to complete in egg yok samples.

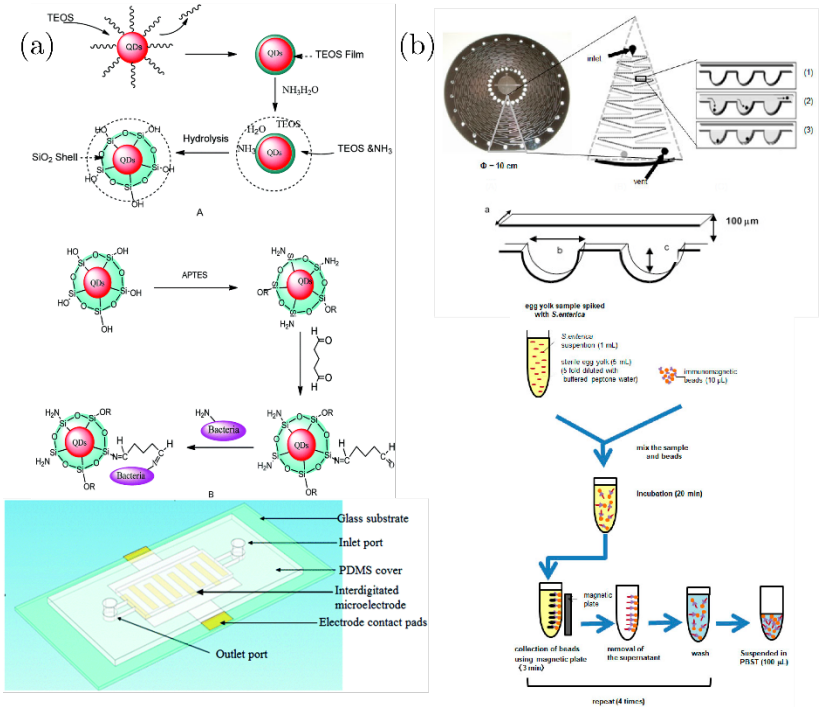

Figure 2-10. Select microfluidic fluorescence-based pathogen detection studies are depicted. (a) Capturing and detection paradigm of bacteria by Wang et al. [143] *is illustrated along with the microfluidic detection platform. Reproduced with permission from the Royal Society of Chemistry. (b) A microfluidic disk presented by Kubo et al.* [144] *to enrich and detect the pathogenic bacteria is demonstrated. Reproduced with permission. Attribution 4.0 International (CC BY 4.0).*

2.5.3.3 Chemiluminescence (CL) Biosensors

Chemiluminescence is referred to chemical reactions that result in light generation. The intensity of the generated light can be measured and correlated to the concentration of analytes involved in the reaction. The CL technique is commonly used to determine hormones and immunoglobulin G (IgG) levels, and it is gaining popularity in microbiological research [145]. It is also used to quantify microorganisms and was previously employed for bacteria detection.

Tan et al. [145] developed a microfluidic ELISA platform (Figure 2-11a) that could be performed and quantified with 8 μL of the sample. They showed a dynamic range of 0.5–250 ng/mL for the mouse follicle-stimulating hormone (mFSH). Multiple capillary arrays were prepared with different concentrations of antibodies and ELISA was performed with a secondary antibody. Lastly, a chemiluminescence substrate was added, and a CMOS camera measured the intensity of the transmitted light.

In another effort by Dong et al. [146], a multi microwell microfluidic biosensor was designed in integration with an organic photodiode (OPD) for simultaneous CL detection of several pathogens (Figure 2-11b). The biosensor consisted of several layers fabricated using spin coating and injection molding from poly methyl methacrylate (PMMA), polydimethylsiloxane (PDMS), glass cover, and OPD. To detect target *E. Coli* O157:H7, they covalently bonded antibodies to the PMMA microwells using APTES-EDC/NHS chemistry. Bacteria-containing samples were infused into the microchannel and were incubated and captured by the primary antibodies. Next, biotinylated antibodies were introduced to the biosensor to sandwich the bacteria. Finally, conjugated horseradish peroxide (HRP) with streptavidin was added to the chip, followed by a mixture of CL reagents and measurement of CL signals. The LOD of this method was 5×10^5 cells/mL for *E. Coli*, 1×10^5 cells/mL for *C. jejuni,* and the detection took 35 mins.

Electrochemiluminescence (ECL) is an electrochemical potential-based approach for generating and regulating CL reactions that have recently become more popular in analytical chemistry [133]. In an effort by Delaney et al. [147], an ECL paper-based microfluidic biosensor was developed by a combination of screen-printed electrodes (SPE) and inkjet-printed paper substrates (Figure 2-11c). Smartphone images were acquired, and red colour intensities were measured and correlated to concentrations of 2-(Dibutylamino)-ethanol (DBAE) and nicotinamide adenine dinucleotide (NADH) that demonstrated LOD of 0.9 µM and 72 µM, respectively.

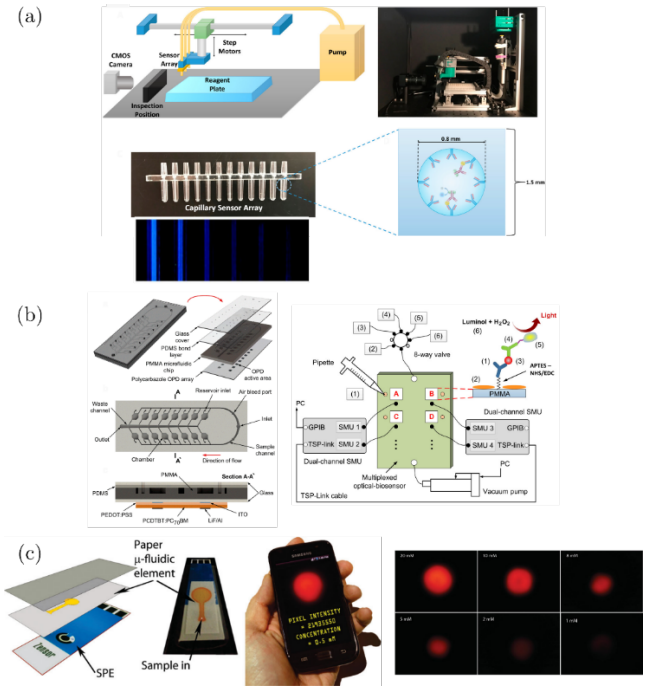

Figure 2-11. Select microfluidics-chemiluminescence pathogen detection sensors. (a) Tan et al. [145] *produced CL capillary sensor based on ELISA is depicted. The platform is automated for experimentation. A CMOS camera was used for light intensity measurement. Copyright © 2018, American Chemical Society (b) Dong et al.* [146] *presented a micro-welled PMMA-made microfluidic device that captured the target antigen using a primary antibody and sandwiched it with the secondary antibody. Later, CL substrate was added, and the intensity was measured. Reproduced with permission. Attribution 3.0 Unported (CC BY 3.0) (c) Delaney et al.* [147] *developed an ECL paper-based platform that allowed for light intensity measurement using smartphones. Copyright © 2011, American Chemical Society.*

2.5.3.4 Resonator Biosensors

Surface plasmon resonance (SPR) is one of the most accurate technologies that allow for single-molecule detection of biomolecular interactions and measurement of their affinity [148]. SPR is produced when an incident light with normal polarization resonates electrons at the interface of two media with distinctive relative tolerances, e.g., a metal and a dielectric. As the SPR is mainly a lab-based technique, there have been some efforts to integrate microfluidics for in situ measurements.

Luo et al. [149] developed a microfluidics-SPR platform for analyzing immunoassay tests (Figure 2-12a). The sensor gold spots were deposited on a glass substrate that acted as the main detection chamber, where the antigen-antibody binding would happen. The device consisted of two PDMS layers. The bottom layer was engraved with the flow microchannels, and the upper layer consisted of several pressure-driven valves to control the flows. The detection and quantification could be performed using a small amount of reagent (6 microliters in 10 min), resulting in nanomolar accuracy. To increase the sensitivity to below picomolar, they used gold nanoparticles to couple with the antigen-antibodies. However, the test time was increased to 1 hr. Although the prototype showed promising low detection limits, issues such as the development costs and proneness to environmental errors need to be addressed.

Manera et al. [150] worked on an SPR-microfluidics platform to detect *L. pneumophila* bacteria from water samples (Figure 2-12b). They used a glass substrate with a thin layer of titanium/gold (2nm/50nm) functionalized with specific protein to capture the bacteria from the aqueous sample and detected changes by a shift in the reflectance signal. They demonstrated the device's specificity for *L. pneumophila* bacteria against *E. coli* and *Salmonella*. Investigating different counts of the target bacteria from water samples, they achieved a linear increase that could be used

to quantify bacteria count (10^3-10^5 CFU/mL) during detection. The device requires 60 min to operate, which is a step forward compared to conventional methods but could not be considered rapid testing.

In another research study based on the SPR technology, Tokel et al. [151] developed a portable device based on the SPR mechanism of a reflecting light (Figure 2-12c). Their handheld device used changes in refractive index to detect contamination of phosphate-buffered saline and peritoneal dialysis fluid with *E. coli* bacteria. The portable platform could detect *E. coli* at counts ranging from ~10^5 to 3.2 × 10^7 CFUs/mL. Although the device showed a compromise in LOD compared to bulky lab-based SPR systems, the sensitivity was acceptable for detecting critical values of bacteria.

Gomez-Cruz et al. [152] presented a cost-friendly and portable platform that took advantage of normal (90 degrees) light emission to a transmission electron microscopy (TEM) grid that has multiple arrays of nanoholes upon it (Figure 2-12d). According to the classic aperture theory, the light should be diffracted when light emits to the aperture with diameters smaller than half of its wavelength. However, it would not be the case when SPR happens on the surface of nanohole arrays. Having the SPR on the TEM grid, the light would be funnelled through the array in a coherent manner that allows "extraordinary light transmission" [153]. As the sample with bacteria (uropathogenic Escherichia coli) was captured on the TEM grid, the intensity of the light changed at the complementary metal-oxide-semiconductor (CMOS) detector. Intensity changes were then correlated to counts of bacteria for sensor calibration. The device showed slight changes in intensity while higher counts of bacteria were tested but demonstrated a 100 CFU/mL detection limit.

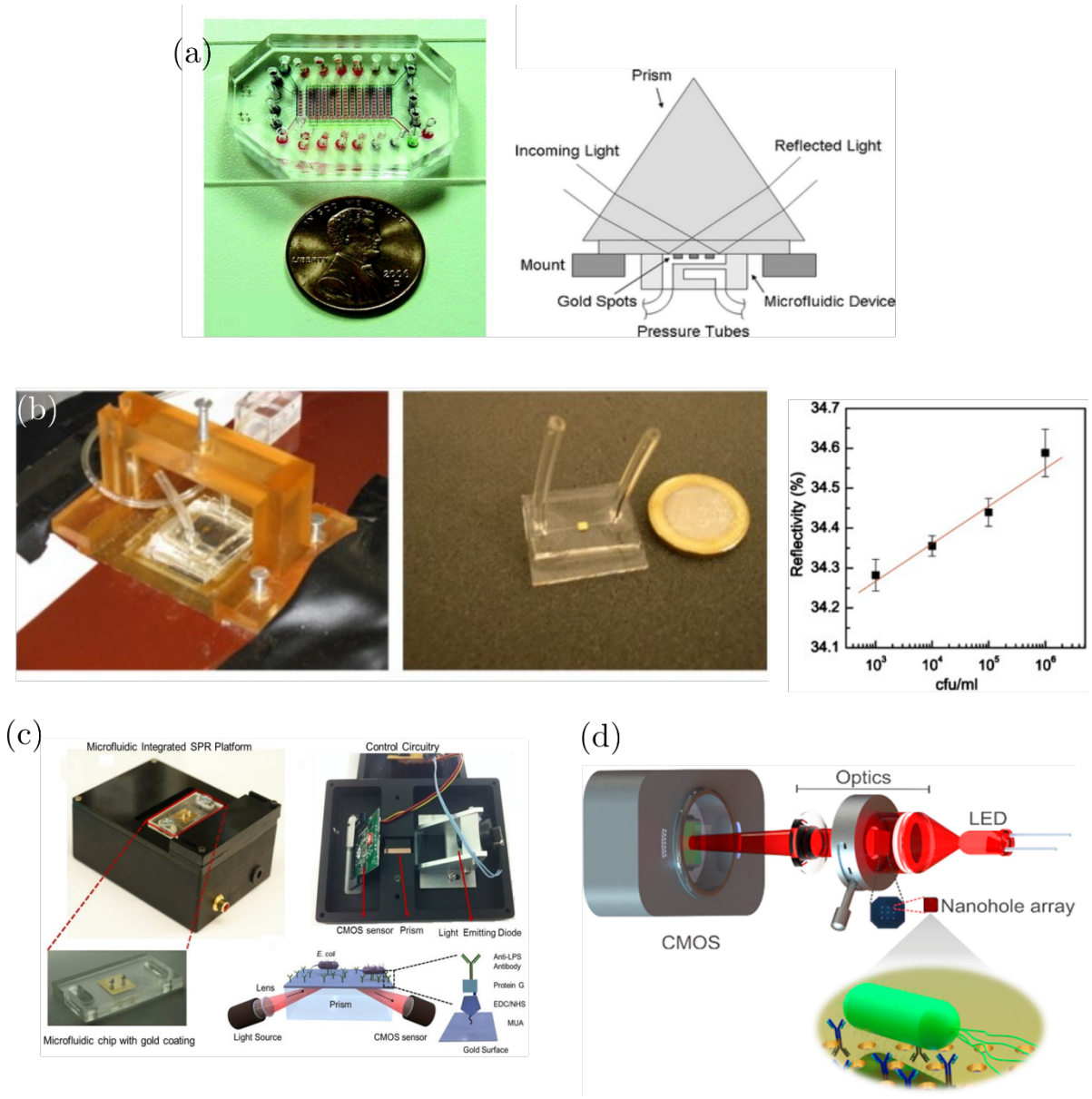

Figure 2-12. SPR-microfluidics devices and working principles. (a-c) Prism enabled SPR pathogen detection with microfluidics integration [149]–[151], [154]. *Reproduced with permission from the Royal Society of Chemistry, Elsevier, and Copyright © 2015, The Author(s). (d) Bacteria detection via nanoarray enabled SPR* [152]. *Reproduced with permission from Elsevier.*

2.5.3.5 Photothermal Detection

Photothermal sensors are capable of measuring the changes in thermal activities. These thermal fields are usually produced due to light irradiation that would be absorbed in the detection chamber.

The photothermal method could be a low-cost and sensitive method for bacteria detection and quantification.

Wang et al. [155] captured bacteria cells in water samples using antibody-tagged particles and then used graphene oxide (GO) as a photothermal agent to attach to the bacteria (**Error! Reference source not found.**a). Then the graphene oxides were excited using a laser source. The increase in temperature was recorded using a thermal sensor and correlated to bacteria count with a detection limit of 10^4 CFU/mL. Du et al. [156] had a similar methodology. However, they used the thermometer surface directly as their detection platform instead of nitrocellulose membranes and achieved a limit of detection of 10^3 CFU/mL (Figure 2-13b). There have been several similar attempts that utilized infrared cameras for signal measurements. Lu et al. [157] captured the bacteria with a detection limit of 1.95×10^4 CFU/mL using antibodies on a nitrocellulose membrane and used MoS_2 as photothermal agents to be excited from a laser source and recorded the increase in temperature by a thermal camera (Figure 2-13c). The device's limit of detection using the photothermal method was 10^3 CFU/mL. Jia et al. [158] captured pathogens on a membrane surface with antibodies and emitted a laser source on the test zone where gold nanoparticles were attached to bacteria and were excited (Figure 2-13d). The excitation resulted in a temperature increase on the surface, and an infrared camera was used to record and correlate the increase in temperature to bacteria count.

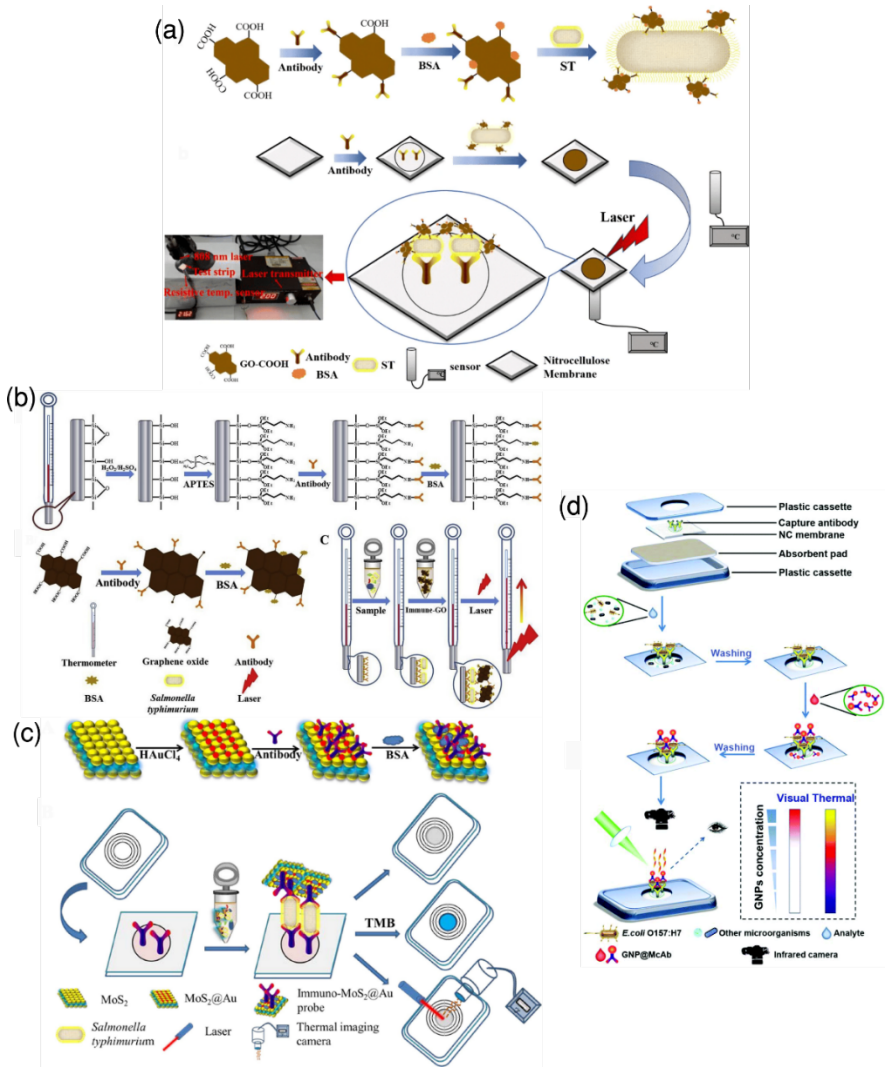

Figure 2-13. Select photothermal pathogen detection platforms. (a) Wang et al. [155] *utilized Ab-coated graphene oxide (GO) immobilized on nitrocellulose that captured the bacteria from the sample solution. Irradiation of laser light was absorbed, and temperature changes were recorded. Reprinted with permission from Springer Nature. (b) Du et al.* [156] *used a similar approach but used a thermometer for this purpose. Reprinted with permission from Elsevier. (c) Lu et al.* [157] *did a trimodal detection using MoS_2 and laser and infrared camera. Reprinted with permission from Elsevier. (d) Jia et al.* [158] *used a nitrocellulose platform to capture target bacteria using Ab-tagged GNP and measured radiations of GNP as a result of laser irradiation by an infrared camera. Reproduced with permission from the Royal Society of Chemistry.*

Although these research studies provided promising results, they have some drawbacks. Some of them have high limits of detections above the sickening threshold of pathogens and/or lack crucial

sensitivity. Some require expensive bulky or lab-based auxiliary equipment, and some are too sensitive to be used for actual samples and outdoor measurements. Most of these works measured absolute temperatures, making them prone to changes in ambient temperature, environmental heat transfer, etc. Thereby, photothermal methods with higher sensitivities, such as active thermography, are needed to surpass these shortcomings. These techniques will be reviewed in the next chapter.

Chapter 3: Methodology and Common Practices

In this chapter, experimental and numerical methodology and common practices are discussed as well as the development procedure and working principles of the microfluidic sensor.

3.1 Microfluidic Sensor Overview: Fabrication and Theory

In this section, the microfluidic sensor fabrication will be elaborated. Then, the theory and equivalent circuit behind the sensor will be discussed.

3.1.1 Experimental Setup

The experimental setup is shown in Figure 3-1a. It consisted of a microfluidic sensor, a DC electrical source-meter (Model 2410, Keithley Instruments Inc., USA), a syringe pump (Legato 110, KD Scientific Inc., USA), a DMIL LED conventional inverted fluorescence microscope (Leica, Germany), and a PC to control and record electrical signals of the source-meter using the manufacturer's software (KickStart, Keithley Instruments Inc., USA).

3.1.2 Microfluidic Sensor Fabrication

The microfluidic sensor shown in Figure 3-1b and Figure 3-1c is comprised of two polydimethylsiloxanes (PDMS) layers, with mirrored channel designs, cast on 3D printed molds. PDMS prepolymer (Sylgard 184, Dow Corning Co., USA) was prepared with a 1:10 cross linker to monomer ratio, poured on 3D printed molds containing the microchannel design and maintained at 80℃ for 2 hours. After peeling off the cured PDMS layers, two microwires (as known as microbridges) with a known diameter were placed in the middle of the channel. The microfluidic

sensor, and the device geometries such as channel width (w), height (h), and inter-wire spacing (g) are also shown in Figure 3-1c. Oxygen plasma bonding was used to seal the two PDMS layers and then to bond them to a glass substrate. Afterward, the device was placed on the inverted microscope to monitor the microchannel while conducting the experiments.

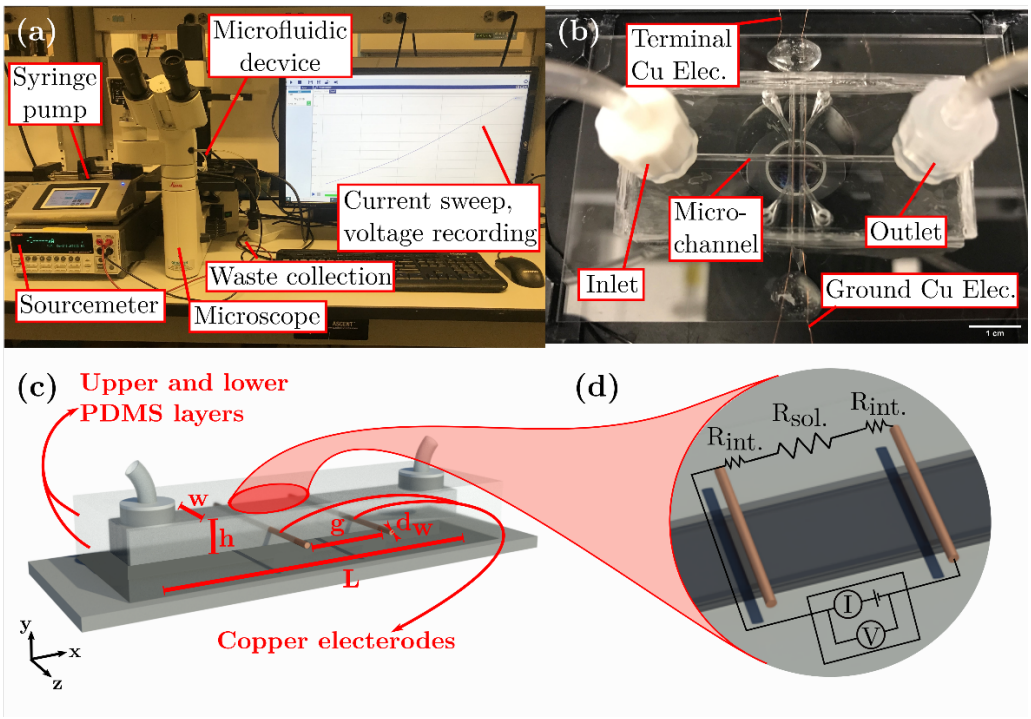

Figure 3-1. Experimental setup and microfluidic salinity sensor. a) Various components of the experimental setup consist of the microfluidic sensor, electric source-meter, syringe pump, microscope, and PC. b) Microfluidic device consisting of a sample flow microchannel with an inlet and an outlet, and two copper microwire bridges acting as terminal and ground electrodes. c) Schematic of the microfluidic device and the geometrical parameters contributing to the salinity sensor's response, including the channel height (h), channel length (L), channel width (w), interwire distance (g), and microwire diameter (d_w). d) The two wires were connected to the source meter. Samples with different NaCl concentrations dissolved in DI water were flown in the channel, and an electric current was swept between the wires from 10nA to 1μA. The corresponding voltages were recorded to calculate the electric resistances based on Ohm's law. The resistance consists of the solution resistance ($R_{sol.}$) and the electrode-electrolyte interface resistances ($R_{int.}$).

3.1.3 Microfluidic Sensor Operation

The terminal and ground microbridge wires were connected to the DC source-meter. As this study aims to pave the way for developing a handheld sensor that runs by a battery in the future, a DC supply was used in our tests. The source-meter swept the DC electric current from I=10 nA to I=1 μA in 1 minute during each experiment while measuring the electric voltage (V) across the copper microwires (Figure 3-1d). The corresponding voltages were recorded using the KickStart software. The measured current and voltage values were used to calculate the NaCl sample resistance, $R=2R_{int.}+R_{sol.}$ in Figure 3-1d, using Ohm's law (R=V/I) [159]. Here, $2R_{int}$ is the electrode-electrolyte interface resistances of the two wires due to their electric double layers in series with the non-uniform solution resistances near the wires. $R_{sol.}$ is the bulk solution resistance which is relatively high for the cases in this study with samples containing low salt concentrations, i.e., high resistivities [159]. More details about the theory of the operation can be found in section 3.2.1.3 below.

3.2 Sensor Applications: Salinity and Bacteria Detection

In this section, methodology and common practices for salinity and bacteria detection applications will be discussed.

3.2.1 Salinity Detection Principles and Methodology

At first, we applied the sensor for salinity detection by measuring the conductivity of the sample between the two copper wires that were used as microbridges. The measured resistance between the two wires would decrease as the salt concentration increases. For the case of NaCl detection, the main component of the equivalent electrical circuit that changes is the solution resistance ($R_{sol.}$), whereas the interface resistance ($R_{int.}$) would be less significant. Here, the primary design will be first reviewed. Next, the numerical modelling procedure followed by the numerical

optimization process will be discussed. The optimized design achieved through the numerical study will be introduced in the results section.

3.2.1.1 Primary Sensor Design

Figure 3-1c depicts the geometrical parameters of the salinity sensor, such as the channel length (L), height (h), width (w), the wire diameter (d_w), and interwire distance (g) that were investigated numerically. In this study two designs were used, beginning with the primary design that had the following geometrical characteristics: h=500 μm, w=900 μm, g=1500 μm, and d_w=90 μm. The data from four replicate fabricated devices of the primary design was then used together with a numerical model to optimize the sensing platform.

3.2.1.2 Sample Preparation for Experimentation

Samples with salinities ranging from 1-120 ppm NaCl dissolved in DI water were used in the salinity sensor studies. The 120 ppm samples were prepared by dissolving 240 mg of NaCl, from Sigma-Aldrich Inc. (Cat. #S7653), in 2 liters of DI water, respectively. Through serial dilution with DI water, concentrations of 100, 80, 60, 40, 30, 20, 15, 10, 7.5, 5, 3, 2, and 1 ppm NaCl were produced and used in the experiments.

3.2.1.3 Numerical Model: Design, Governing Physics, and Boundary Conditions

A numerical model was developed in COMSOL Multiphysics based on the experimental configuration of the primary sensor (Figure 3-1c,d) which was then verified and validated against the experimental measurements. After validation, the model was employed to find an optimized sensor geometry to increase its sensitivity for salinity measurement applications. The parameters used in this study and their units are summarized in Table 3-1. The model of the primary sensor consisted of a 2D rectangular microfluidic channel, cross-sectioned across the x-y plane of Figure 3-1c at the middle of the channel, with two 90 μm diameter circles representing the wire electrodes

in the middle. The microchannel height (along the y-axis) was h=500 μm. The width of the microchannel along the z-axis was set to w=900 μm using COMSOL's out-of-plane thickness feature, which allowed achieving similar results to 3D simulation in a 2D setup. Interwire distance was set to g=1500 μm.

Table 3-1. Parameters used in the numerical model with their symbols, descriptions, and units.

Symbol	**Description**	**Units**	**Symbol**	**Description**	**Units**
ρ	Density	Kg/m3	E	Electric field	V/m
u	Mean velocity	m/s	ρ_{el}	Electrical resistivity	Ohm. m
p	Pressure	N/m2	J	Current density	A/m2
μ	Viscosity	Pa.s	V	Electrical potential	V
Re	Reynolds number	-	σ	Electrical conductivity	S/m
D_h	Hydraulic diameter	m	Q_j	Current source	A/m3
A	Microchannel cross-section area	m2	J_e	External current density	A/m2
P	Microchannel wetted perimeter	m	z_i	Charge number of ions (e.g., +1 for Na+)	C
d_w	Wire diameter	m	T	Temperature	K
w	Width (along the z-axis in Figure 3-1c)	m	C_p	Specific heat capacity	J/kg. K

h	Height (along the y-axis in Figure 3-1c)	m	k	Thermal conductivity	W/m. K
L	Microchannel length (along the x-axis in Figure 3-1c)	m	Q_e	Resistive dissipation	W/m3
g	Interwire distance (along the x-axis in Figure 3-1c)	m	Q_{ted}	Thermoelastic dissipation	W/m3
J_i	Diffusive flux	Mol/cm2.s	Q_{vd}	Viscous dissipation	W/m3
F_c	Faraday's constant	C/mol1	Q_p	Pressure work	W/m3
$u_{m,i}$	Ionic mobility	m2/s. volt	Q	Heat source	W/m3
Λ	Molar conductivity	S/cm2.mol	R	Molar gas constant	J/mol. K
c	Molar concentration	Mol/ L	R_i	Reaction rate	M/s
α	Correlation factor	-	F	Other forces	N/m3
Λ_0	The infinite dilution	S/cm2.mol	I	Identity matrix	-
κ	Specific conductance	S/m			

Governing Physics.

The simulation model was governed by the physics of fluid flow, electric field, transport of diluted species, and heat transfer. To obtain a better convergence in our simulation, we first computed the fluid flow and electric potential profiles in the microchannel, and then the electrochemical and heat transfer behaviors were developed.

The flow regime in this study would fall into the laminar flow category with the Reynolds number, Re in equation (3-1), being 16<Re<64. Thereby, the simplified incompressible non-Newtonian continuity equation (3-2) and Navier-Stokes equation (3-3) were employed to solve for the electrolyte flow under steady-state conditions.

$$Re = \frac{\rho u D_h}{\mu} \tag{3-1}$$

$$\nabla.(\rho\vec{u}) = 0 \tag{3-2}$$

$$\rho(\vec{u}.\nabla)\vec{u} = \nabla\{-pI + \mu(\nabla\vec{u} + (\nabla\vec{u})^T)\} + \vec{F} \tag{3-3}$$

The hydraulic diameter of the channel was obtained from equation (3-4).

$$D_h = 4\frac{A}{P} = \frac{4wh}{2(w+h)} = \frac{2wh}{(w+h)} \tag{3-4}$$

The electrolyte sample containing sodium and chloride ions flows at a constant flow rate in the microchannel. The applied electric field between the wires causes the ions to migrate toward the electrodes with the opposite charge, and an electric double layer would be shaped. Steady-state charge conservation equation (3-5) governs the electric field in the microchannel and electric current passing from the terminal to the ground electrode through the electrically conductive electrolyte sample.

$$\nabla.\vec{J} = -\nabla.(\sigma\nabla V - \vec{J}_e)d = Q_j w \qquad 3\text{-}5)$$

The electrical resistance, *R,* between the wires was assumed to be related to the sample electrical resistivity, ρ_{el}, and other geometrical properties of the channel as defined in equation (3-6).

$$R = \rho_{el}\frac{g}{hw} \qquad 3\text{-}6)$$

Mass conservation equation (3-7) was solved to investigate the diffusion, convection, and ionic migration of the dissolved NaCl ions for one or more solutes (i) [160]. Fick's law governs the diffusion term.

$$\frac{\partial c_i}{\partial t} + \nabla.\vec{J}_i + \vec{u}.\nabla c_i = R_i \qquad 3\text{-}7)$$

The reaction rate is for chemical reactions in the model, which does not apply in our study. The diffusive flux vector in the case of applying the electric field is expressed below.

$$\vec{J}_i = -D_i\nabla c_i - z_i u_{m,i} F c_i \nabla V \qquad 3\text{-}8)$$

For a very dilute solution, the ionic mobility of solute *i* can be obtained from the Nernst-Einstein equation (3-9).

$$u_{m,i} = \frac{D_i}{RT} \qquad 3\text{-}9)$$

Debye–Hückel–Onsager equation (3-10) was used to calculate the electrolyte conductivity at different concentrations of NaCl below 0.001 mol/L (~60ppm) [161]. This equation is suitable for very dilute solutions of strong electrolytes (e.g., NaCl) with high solubility in their solvent, as expressed below.

$$\Lambda = \Lambda^0 - (A + B\Lambda^0)c^{1/2} \qquad 3\text{-}10)$$

The values of A and B constants depend on the viscosity and dielectric constant of the solvent, temperature, and charge. In the case of NaCl and water at 25℃, A = 60.20, B = 0.229, and $\Lambda^0 = 126.39 \times 10^{-14}$ [161]. For salt concentrations between 60 and 120ppm, a correlation factor of α=0.55 was used to correlate the salt concentration to electrical conductivity [162], [163]. The electrical resistivity for the salty water samples was then calculated from equation (3-11).

$$\rho_{el} = \frac{1}{\kappa} = \frac{1}{\Lambda c} \qquad 3\text{-}11)$$

To consider the possibility of resistive dissipation in form of heating in wires which perturbates the recorded signal, and to ensure that this physical phenomenon is not overlooked in the numerical model, equation 3-12) was employed to solve the steady-state heat transfer in a solid [164].

$$\rho C_p(\frac{\partial T}{\partial t} + \vec{u}_{trans}.\nabla T) + \nabla.q = Q + Q_{ted} + Q_e \qquad 3\text{-}12)$$

where q is the conduction heat flux, u_{trans} is the translational motion velocity, Q_e=$J.E$ is electromagnetic heating (resistive dissipation), Q is the heat source (or sink) and Q_{ted} is the thermoelastic dissipation that is responsible for the expansion of material upon heating. The conduction heat transfer of the wires in the microchannel is accounted for on the left side of the equation 3-12). On the right-hand side of equation, the first term considers the heat conduction in the wires, the second term computes the resistive losses in wires which employs the electric field profiles from the electric current module, and the third term is the electromagnetic heating. The last two terms are negligible and do not apply in the case of our salinity sensor.

Heat transfer in fluids. Similarly, the heat transfer in a fluid considers conduction, convection, viscous heating (Q_{vd}) which occurs as a result of friction upon microchannels walls, and the work that is resulted from pressure changes (Q_p) (similar to heating from adiabatic compression) which is negligible in our study. It is noteworthy to mention that the convection is only negligible in creeping flows since the flow velocity is small and conduction would be the main heat transfer method [165]. Equation 3-13) was solved in a steady state condition to obtain heat transfer in the fluid traversing the microchannel where *u* is the velocity vector [164].

$$\rho C_p(\frac{\partial T}{\partial t} + \vec{u}.\nabla T) + \nabla.(q) = Q + Q_{vd} + Q_p \qquad 3\text{-}13)$$

Boundary Conditions.

The boundary conditions were selected based on the experimental conditions. A fully developed flow profile with a constant flow rate of 0.2 mL/min was imposed in the x-direction for the primary and optimized sensors. The actual devices had a longer channel length in the x-direction than the numerical study that allowed for the safe assumption of a fully developed flow. The velocity in the y-axis direction was zero, and a no-slip boundary condition was applied throughout the microchannel and wire walls. Static gage pressure of zero (p=0) was considered at the channel outlet. The two copper microwires were considered as the electrodes that probe and measure the resistance in the salinity sensor. A ramping DC current of 10 nA to 1 μA was maintained in the terminal while the ground was assumed to have no voltage (V=0). The PDMS walls were insulated (J=0).

Two important parameters of the numerical model were the dynamic viscosity and density of the sample. According to previous studies [166], [167] upon adding 10,000 ppm of salt to water at 25°C, an increase of 0.7% and 2% would be observed in the dynamic viscosity and density of

water, respectively. These slight changes were safe to be neglected in our models with 1-120 ppm salt concentrations. Therefore, the water dynamic viscosity of μ = 8.90 × 10^{-4} Pa·s and density of ρ=1000 kg/m^3 were considered in the numerical analyses.

For the heat transfer study, the characteristics of copper wires are considered according to the experimental study. The parameters and the values of the copper wires that were imposed in the simulation include thermal conductivity at k = 400 W/m. K, density at 8960 kg/m^3, and heat capacity at constant pressure equal to C_p = 385 J/kg. K. In the case of salt and water mixture, heat transfer properties of seawater at 25℃ is reported to have a slight increase of 1.3% in heat capacity at constant pressure and 0% in thermal conductivity [166], which allows us to neglect any change in heat transfer properties of water in salt concentrations of 1-120 ppm. Therefore, the thermal conductivity of k = 0.6 W/m^2 and heat capacity at a constant pressure of C_p= 4186.5 J/kg. K were assumed for the electrolyte.

Heat Generation in Salinity Sensor.

The highest resistance measured by the salinity sensor for the case of 1ppm was 178MΩ. The measurements were performed by a sweeping current of 10nA-1μA. This would result in a maximum power dissipation of P=RI^2=178 μW, considering the maximum current of I=1 μA. We should also consider the effect of convection because of fluid flow in the channel, that is at Q=0.2 mL/min (3.3333e-9 m^3/s) for the optimized sensor. The flow rate could be converted to the mass rate with $\dot{m} = \rho Q = 1000\ kg/m^3 \times 3.33 \times 10^{-9}\ m^3/s = 3.33 \times 10^{-6}\ kg/s$. Thus, the temperature difference generated was $\Delta T = P/(\dot{m}c) = 178\ \mu W/(3.33 \times 10^{-6}\ kg/s \times 4190\ J/KgK) =$ 0.003K. Thereby, the effect of thermoelectric heating is negligible and is not expected to affect the measurements.

3.2.2 Bacteria Detection Principles and Methodology

As previously mentioned, the sensor was employed for bacteria detection as the second contamination sensing application. The device in this application was used to capture the target bacteria on the surface of the wires by means of capturing antibodies (capAb, See **Error! Reference source not found.**). The signal acquisition was performed by two different methods.

First, electrical detection was performed by measuring the conductivity between the two wires in the microfluidic device and based on Ohm's law (See **Error! Reference source not found.**). In electrical detection, as bacteria are conductive entities [168], an increase in their count around the wires in expected to bring about a decrease in the measured resistance between the two wires. Unlike the NaCl detection, the main components of the equivalent electrical circuit that change are the interface resistances ($R_{int.}$), while the solution resistance ($R_{sol.}$) would remain constant. This is due to our experimental procedure in which the solution before and after bacteria capturing remained the same in all experiments using a post-capturing washing process.

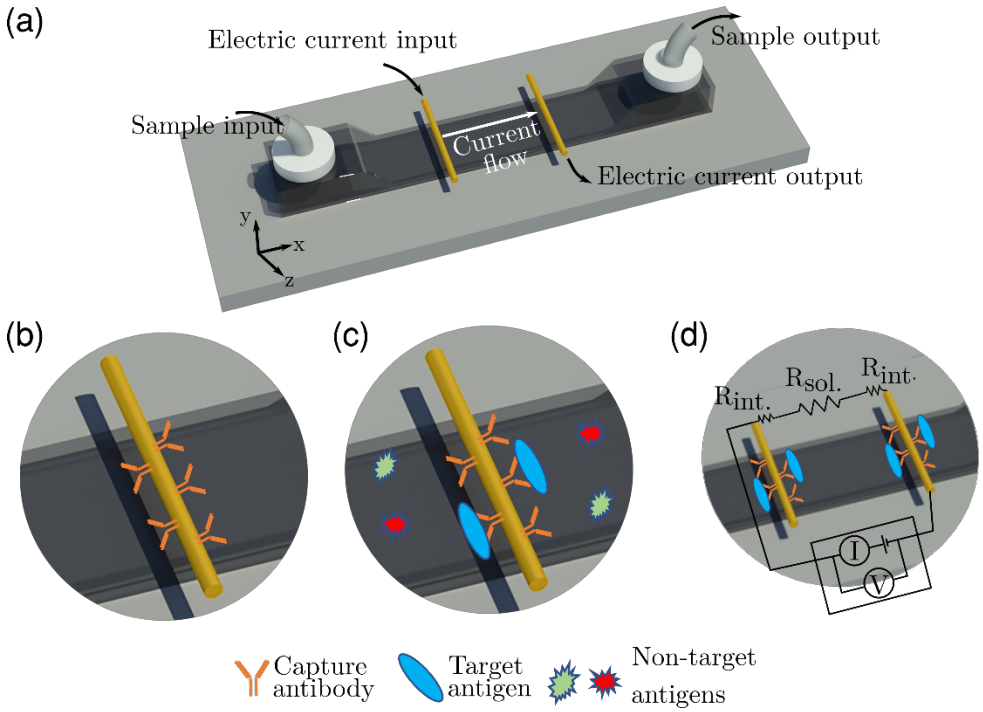

Figure 3-2. Electrical bacteria detection platform. (a) Microfluidic device with gold coated wires is depicted. (b) Magnified view of the wires with previously coated capture antibodies are illustrated. (c) E. coli K12 could be captured on the wires. (d) Electrical detection inside the microchannel isshown.

Second, photothermal detection was performed on wires and outside a device, using gold nano particles (GNPs) that sandwiched the bacteria via the detection antibody (detAb, See Figure 3-3). Then, the sensor was illuminated with an intensity-modulated laser light which resulted in modulated temperature variations at the interface of GNPs due to surface plasmon resonance. These thermal modulations were subsequently sensed by a cellphone attachment infrared camera and demodulated. Both electrical and photothermal recordings were correlated to the bacteria counts. In this study, gold-coated copper wires were used as the Ab immobilization on gold is well established in the literature.

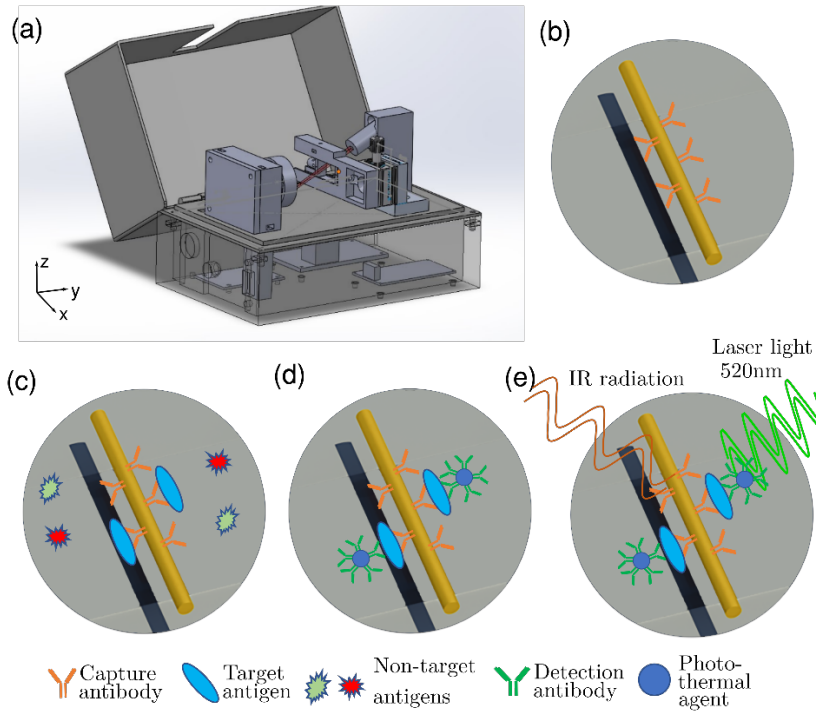

Figure 3-3. Photothermal bacteria detection platform. (a) A preliminary compact and handheld device for bacteria photothermal detection on gold-coated wires is depicted. (b) A magnified view of the wires with previously coated capture antibodies are illustrated. (c) E. coli K12 could be captured on the wires. (d) GNPs coated with detection antibodies sandwiched the bacteria off-chip. (e) Photothermal detection inside and outside the microchannel, respectively, are shown.

Here, we will introduce the theory and background of photothermal detection as the electrical detection was elaborated in section 3.1.1. Next, the materials and methodologies used to produce the test samples and perform detection will be discussed.

3.2.2.1 Active Thermography

The photothermal detection used in this thesis falls under the general sensing area of Active Thermography (AT). AT is a term that refers to a collection of thermographic methods used for non-destructive material testing (NDT). AT is extensively employed in many areas of engineering and science, including moisture detection in building structures in civil engineering [169], identifying leakage sources in electronic components in electrical engineering [170], and safety

checks of aero-engine parts, space shuttle parts, and primary and secondary structures of aero planes [171]. AT has also been utilized in biology and medicine to assess skin thickness, blood flow, skin burns, inflammations, early dental caries detection, and pathogen detection [172]–[175].

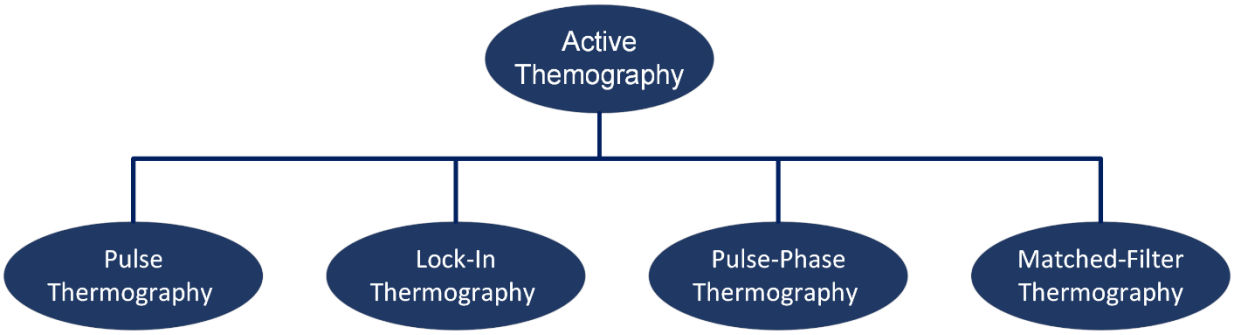

Figure 3-4. Subcategories of Active Thermography.

In AT, the specimen is stimulated by an external excitation source, and the photothermal responses are measured using infrared detectors such as infrared cameras. When there are internal defects in the specimen, the temporal profile will differ from the intact regions that result in their detection. The nature of the excitation source may be adapted to the application, which is one of the advantages of AT. These sources include optical, mechanical, and electromagnetic excitation sources [176]. In this thesis, optical excitation is focused. AT can be divided into four groups based on the temporal pattern of light excitation used:

a. **Pulse Thermography (PT):** The sample is stimulated by light pulses in PT [177]. The excitation source is commonly a heat gun, a lamp, or a similar instrument. As a result, PT is predicated on collecting responses while the sample surface is cooled. Sandwich constructions and composites are mainly subjected to PT testing [178].
b. **Lock-In Thermography (LIT):** An infrared camera receives the thermal wave radiated from a surface in a steady-state thermal regime (also known as a thermal-wave field) as the

sample is heated with a modulated excitation source. The modulated infrared signals are then demodulated at the known modulation frequency of the excitation source to obtain the amplitude and phase of thermal waves [179], [180]. As the phase image in LIT is emissivity-normalized, it does not show the effect of non-uniform heating or differences in sample surface emissivity [181], [182]. However, amplitude images are mainly used for analysis as they offer a superior signal-to-noise ratio (SNR). A key advantage of LIT is that it measures variations in temperature change and is not prone to variations in ambient temperature.

c. **Pulse Thermography (PPT):** PPT is a novel technique that takes advantage of the PT data with an analysis methodology similar to the phase and frequency concept in LIT [183], [184].

d. **Matched-Filter Thermography (MT):** The fundamental drawback of the methods outlined above is the inherent trade-off between examination depth and image resolution [185]. In other words, lower excitation frequencies are required to investigate deep within a sample, but this results in poor resolution and vice versa. Matched-filter Thermography (MF) is presented as a solution to this issue [186]. To achieve highly resolved images from low-frequency excitations inspecting deep in the sample, MT employs Radar's cross-correlation filtering with pulse compression techniques such as linear frequency modulation or binary phase coding [186]–[188].

3.2.2.2 Lock-in Thermography (LIT)

Among the several mentioned active thermography approaches, LIT has provided a preferable balance of defect detection sensitivity and system complexity and/or cost [189]. The lock-in thermography's working principle is based on introducing a light source with periodic modulation

(e.g. laser source) on the sample's surface and local temperature acquisition with an infrared camera [190]. Thermal impedances introduced by defects inside the sample (or absorbers of laser light such as GNPs) affect the amplitude and phase of the local thermal wave field. As a result, a detectable contrast is recorded in the collected infrared emissions from the sample surface [191]. Using quadrature demodulation, the amplitude and phase of infrared emissions from a sample surface are precisely computed in LIT and analyzed toward detection (also known as lock-in detection).

From non-destructive inspection of industrial samples for defects [192] to early diagnosis of diseases in soft and hard tissues [191], [193], LIT has been extensively employed in a wide range of industries. Assessment of fibre orientation in composites [194], evaluation of material thermal diffusivity [195], and detection of flaws such as cracks in samples [196] are examples of LIT uses in NDT. The analysis of a resin-embedded human tooth was one of the first LIT studies for medical diagnosis [197], [198]. Some other medical applications of LIT include early detection of dental caries [172], early phases of diagnosis of cutaneous melanoma [193], and developing portable devices for detection of target analytes in lateral flow immunoassays (LFAs) [175].

3.2.2.3 LIT Theory

Defects below the surface operate as a thermal resistance to heat diffusion, changing the local amplitude and phase of thermal radiation recorded by an infrared camera from the interface. Absorbers of laser excitation such as GNPs induce similar effects as internal defects of opaque materials. The depth integrated signal recorded by the infrared camera is theoretically expressed as [172], [199]:

$$s(l,t) \propto \overline{\mu_{IR}} \int_0^l T(z,t) e^{-\overline{\mu_{IR}} z} dz \qquad 3\text{-}14)$$

where $\overline{\mu_{IR}}$, l and $T(z,t)$ are the mean infrared absorption coefficient of the sample in the wavelength range of the infrared camera, specimen thickness or defect depth, and induced thermal wave field, respectively. The determination of the amplitude and phase of a thermal wave field ($T(z,t)$) is the final goal of LIT. For example, the thermal wave field of a semi-infinite opaque material is given as

$$T(z,t) = \frac{Q}{2\sqrt{\rho k c \omega}} e^{\left(\frac{-z}{\mu}\right)} e^{\left[i\left(\omega t - \frac{z}{\mu} - \frac{\pi}{4}\right)\right]} \qquad 3\text{-}15)$$

Where μ, k, c, ρ, and ω are the thermal diffusion length, thermal conductivity, specific heat, sample density, and laser modulation angular frequency, respectively. This equation shows that thermal waves dissipate exponentially with depth and that the rate of this exponential dissipation is a function of the thermal diffusion length (μ). The depth where the amplitude of a thermal wave falls to e^{-1} of its primary value is thermal diffusion length, and it is considered the maximum depth of inspection. The length of thermal diffusion can be numerically stated as:

$$\mu = \sqrt{2\alpha/\omega} \qquad 3\text{-}16)$$

Thus, thermal diffusion length is proportional to medium thermal diffusivity (α) but inversely proportional to the laser modulation frequency (ω). Therefore, the inspection depth can be adjusted by adjusting the modulation frequency. Thermal waves are less dissipated at lower frequencies and can probe deep into samples, whereas inspection depth is shallow at higher frequencies. The

spatial resolution of the Lock-in images is improved by raising the modulation frequency and, as a result, reducing the thermal diffusion length.

One of the signal processing techniques to retrieve the amplitude and phase of a recorded signal in a noisy channel by knowing the modulation frequency is lock-in demodulation. As the intensity of laser excitation varies at a specific and known modulation frequency (aka lock-in frequency), lock-in demodulation can be performed on the signals to retrieve amplitude and phase information. The process of demodulation begins with mixing camera frame signals ($ASin(\omega_0 t + \varphi)$) with unknown amplitude (A) and initial phase (φ) with in-phase ($\sin(\omega_0 t)$) and quadrature ($\sin(\omega_0 t + 90)$) reference signals. Afterward, the signals are weighted, and low pass filtered to obtain in-phase (S^0) and quadrature (S^{90}) images. Then, the amplitude (A) and phase (φ) can be obtained from the in-phase and quadrature images:

$$\begin{matrix} Sin(\omega_0 t) \times ASin(\omega_0 t + \varphi) \\ Sin(\omega_0 t + 90) \times ASin(\omega_0 t + \varphi) \end{matrix} \xrightarrow{Mixing} \begin{cases} \frac{A}{2}[Cos(\varphi) - Cos(2\omega_0 t + \varphi)] \\ \frac{A}{2}[Sin(\varphi) - Cos(2\omega_0 t + \varphi + 90)] \end{cases} \xrightarrow{Weighting \times \sqrt{2}}$$

$$\begin{cases} \frac{A}{\sqrt{2}}[Cos(\varphi) - Cos(2\omega_0 t + \varphi)] \\ \frac{A}{\sqrt{2}}[Sin(\varphi) - Cos(2\omega_0 t + \varphi + 90)] \end{cases} \xrightarrow{LPF} \begin{cases} S^0 = \frac{A}{\sqrt{2}} Cos(\varphi) \\ S^{90} = \frac{A}{\sqrt{2}} Sin(\varphi) \end{cases} \rightarrow \begin{cases} A = \sqrt{(S^0)^2 + (S^{90})^2} \\ \varphi = arctan(\frac{S^{90}}{S^0}) \end{cases} \quad (3\text{-}17)$$

Alternatively, the amplitude and phase of thermal waves may be directly computed by applying the fast Fourier transform (FFT) to the time lapse data from each infrared camera pixel. The frequency range of a time-lapse signal after Fourier treatment shows a strong peak at the modulation/lock-in frequency [200]. Amplitude and phase are determined using the complex number obtained via FFT at the modulation frequency. While amplitude images have a higher

SNR, LIT phase images are emissivity-normalized by nature [188], meaning that systematic errors due to differences in sample surface emissivity do not affect phase values.

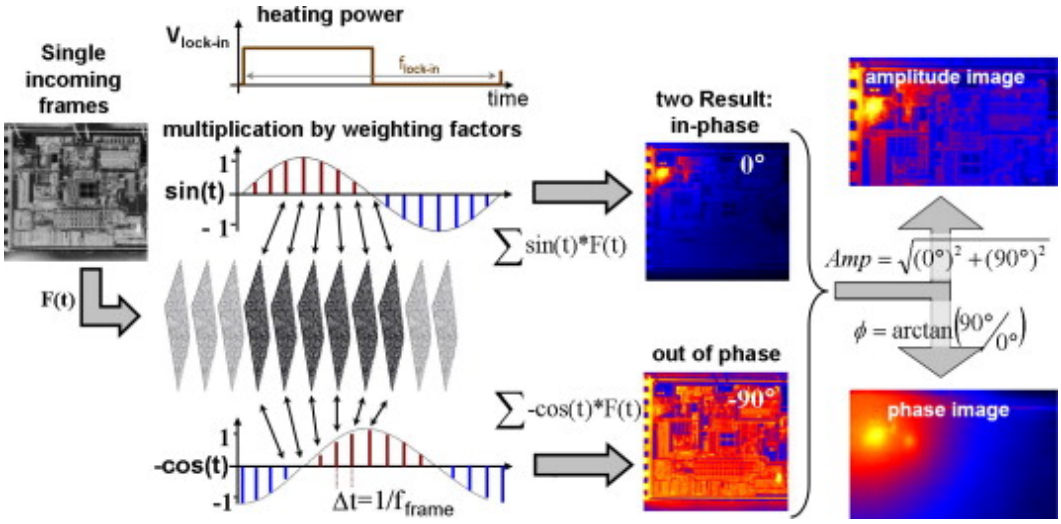

Figure 3-5, Demonstration of Lock-in thermography (LIT) operation [201]. *Reprinted with permission from Elsevier.*

3.2.2.4 LIT Detection Process

The bacteria captured on Ab-coated wires were sandwiched with the Ab-coated GNP. The GNP absorbed the modulated light upon laser irradiation, resulting in excitation and creating a modulated temperature field or thermal-wave field. The infrared camera then received the thermal radiations from the photothermal agents. The LIT allowed for distinguishing the signal from the background noise as the receiving signals had a similar frequency to that of the laser source's modulation frequency. The amplitude and phase images were then calculated. Afterward, the amplitude intensity on the bacteria-attached wires' surface was analyzed and studied to achieve the sensor’s calibration curve.

3.2.3 Photothermal Sensor Fabrication and Experimentation

Several configurations were examined for the photothermal sensing that will be briefly reviewed in this section, and the final configuration will be presented.

3.2.3.1 Preliminary Photothermal Setup

A compact and low-cost photothermal detection setup was developed based on a previously presented compact design [175]. The design needed modifications to accommodate radiation from the back of the microfluidic device and the collection of IR radiation on the other side. The reason was that the photothermal detection could not be achieved on the microfluidic device in the form it existed in the salinity detection and needed to be modified. As the PDMS would block the infrared radiation signals from the wires, a design modification was required to facilitate the detection. Therefore, we punched a 0.7 cm circular section of the top PDMS part in a preliminary design, and plasma bonded to a 1.0cm zinc celanide glass to cover the opening and prevent leakage (Figure 3-6a). A slit was also designed to hold the microfluidic device on the platform for detection (Figure 3-6b). Figure 3-6c and d show the developed computer-aided design, showing the internal electrical circuit components and the laser and the thermal camera. We used a low-cost (~250$) infrared camera (SEEK THERMAL COMPACT; Seek Thermal Inc.; Android; 206 × 157 Pixels) to record 33 frames per second in conjugation with a secondary Zinc Selenide lens ($ 10; MCWlaser Inc, Wuhan, China). The preliminary setup was equipped with an 808nm laser diode ($20; Besram Technology Inc, Wuhan, China). A generic timer relay circuit ($ 2.5) was utilized for system electronics to deliver electric power to the system for 30 seconds when the push button was triggered. Based on a 1 Hz transistor-transistor logic (TTL) signal received from a generic pulse-width modulation (PWM) circuit ($1.5), the laser driver ($12; Wuhan Jingluyao Trading Co., China) provided intensity-modulated electric current to the laser diode to enable the modulated signals.

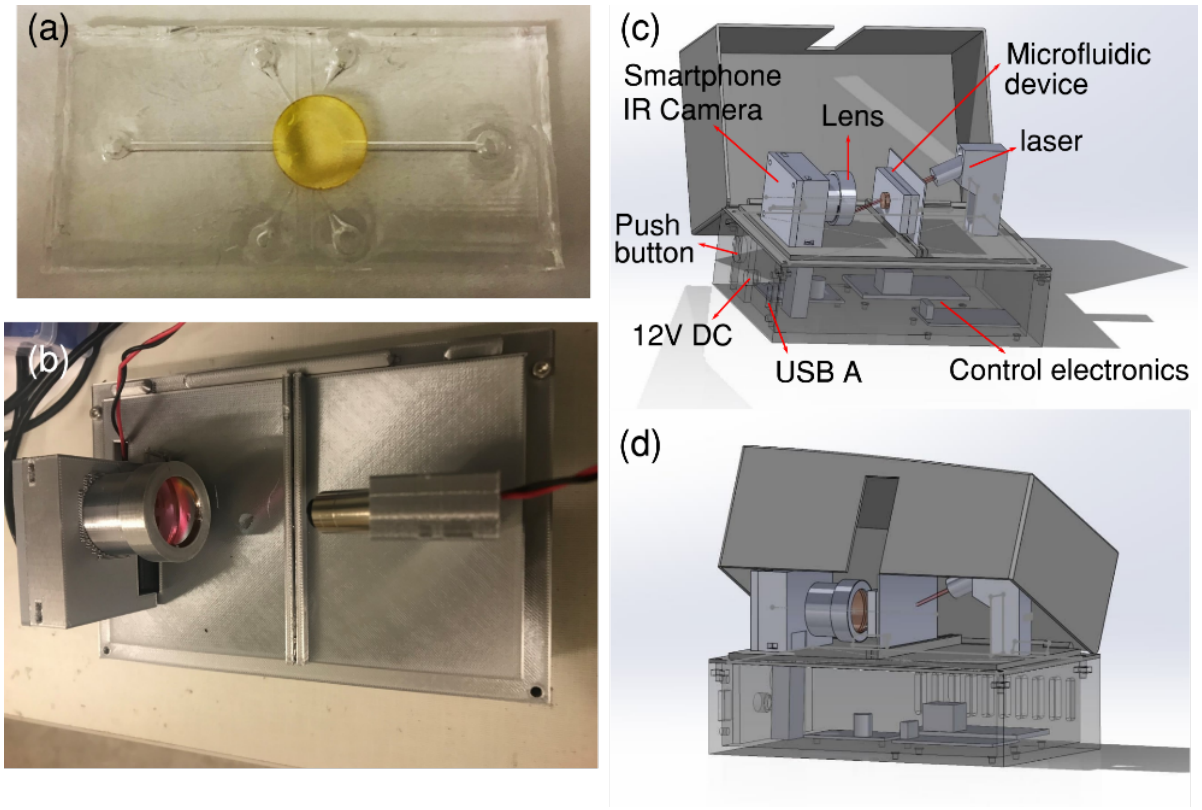

Figure 3-6. Preliminary photothermal detection setup. (a) The top PDMS part is punched to block IR radiation and bonded with a ZnS glass to facilitate IR radiation. (b) Bird's eye view of the compact preliminary detection. (c-d) Computer-aided design of the preliminary setup and detection.

Several issues affected the detection that made us further modify the setup. The first issue was that the fluid in the microchannel would block the IR radiation, and the channel should be dried after the conjugation of GNPs. The following issue after drying was the wire wetting effect caused when the wires were not completely dried and interfered with the photothermal signals. The last issue was the evaporation in the detection chamber due to laser irradiation, which gradually blocked the signals.

3.2.3.2 Modified Photothermal Setup

The modified setup replaced the microfluidic device with a wire holder and a sliding holder frame to measure photothermal activity straight from the wires (Figure 3-7a). The designed holder frame

attached to a transactional stage is illustrated in Figure 3-7b, and the wire holder that fixes the gold-coated wires with a bolt and nut in the designated areas is depicted in Figure 3-7c.

In this detection paradigm, the wires were prepared according to the protocols discussed in future sections and were tested as they were installed on the wire holder, as in Figure 3-7c. The modified platform allowed for fixing the wires in the middle of the laser beam as the translation stage allowed for displacing the wire on the z-axis. The amplitude and phase images were obtained for each wire, and the raw signal was collected from the amplitude image (Figure 3-7d). The amplitude image consisted of 156 rows and 206 columns of pixels. The amplitudes images were cropped to 156 rows and 60 columns of pixels that corresponded to wire locations. Histogram of the cropped images were plotted as shown in (Figure 3-7e). The observed peak in the histograms corresponded to the background noise which was subsequently filtered. For the filtration, a threshold metric was defined as the upper extreme of the $1/e^2$ of the halfwidth. This thresholding enabled us to quantify the tail section of the histogram which contains the signals from the wire (depicted with a vertical red line in Figure 3-7h). The amplitude values above the threshold were averaged and were examined for correlation with bacteria count.

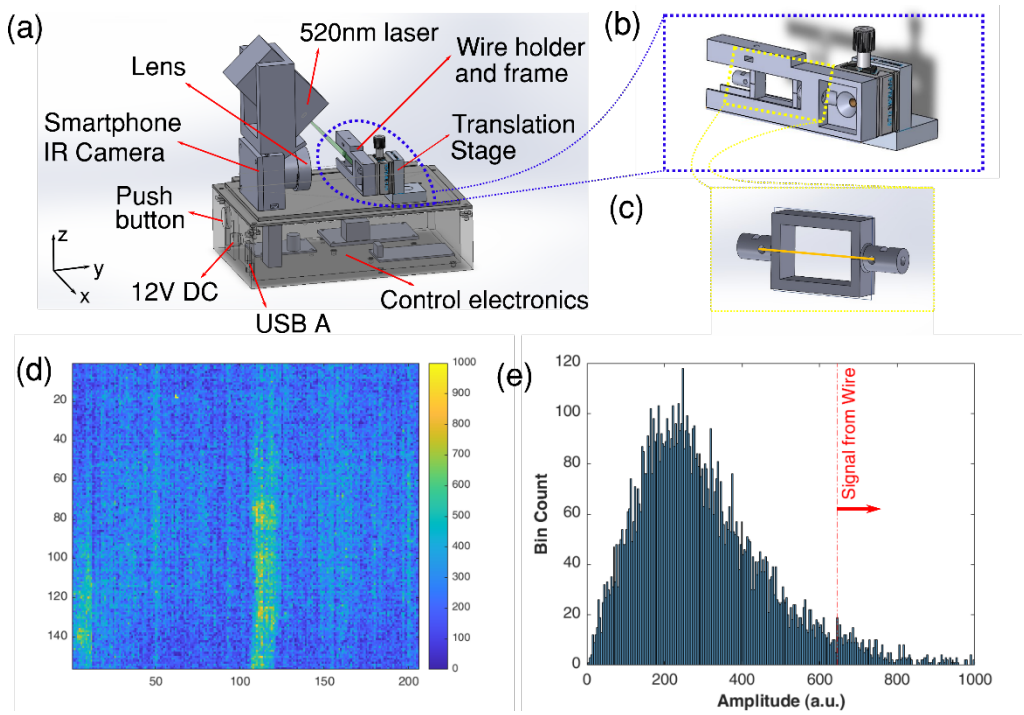

Figure 3-7. Modified Photothermal setup. (a) The setup modified for detecting bacteria straight from the wires is shown. (b) The holder frame is equipped with a translation stage to move in Z-direction. (c) The wire holder to install the gold-coated wires for the purpose of the detection is shown. (d) A sample amplitude image with the wire treated with 10^6 CFU/mL is depicted. (e) To analyze the amplitude image, we averaged the obtained signal from the wire, shown on the left side of the drawn red line.Materials and Reagents

Unless mentioned otherwise, all the materials and reagents were purchased from Sigma-Aldrich (Missouri, USA). For all the experiments, ultrapure and sterilized water were used. Gram-negative *Escherichia coli* Strain K12 (*E. coli*) with a red fluorescent expressing tag was purchased from Thermo Fisher Scientific (Cat. #E2863) as the target pathogen. Gold nanoparticles (GNPs) with diameters of 20nm were used as a photothermal agent to absorb the laser light source and generate the required temperature field for detection via lock-in thermography. Also, polyclonal anti-*E. Coli* antibodies were obtained to be conjugated to the target pathogen from Thermo Fischer Scientific (Cat. #PA1-7213). Bovine serum albumin (BSA) would be used to block the antibodies that are

not attached to the *E. Coli* and prevent non-specific conjugation. Gold-coated wires were purchased from MWS Wires with a diameter of 127µm. MES (2-(N-morpholino) ethanesulfonic acid) buffer was purchased from Thermo Fisher Scientific (Cat. #28390).

3.2.3.3 Immobilization of Anti-*E. coli* CapAb on Wires

The gold-coated wires that were used in this study were pre-modified with anti-*E. Coli* capture antibodies to capture the target bacteria from the sample. Two different protocols were tested to immobilize capturing antibodies on the surface of the gold-coated wires. The first and second protocols were based on direct and covalent-bonding immobilization techniques, respectively. The former used physical adsorption, and the latter were enabled through the covalent bonding of antibodies to the surface by chemical crosslinkers. Both methodologies are summarized below.

For both methods, an identical wire cleaning protocol was carried out. Briefly, the wires were washed by incubation with acetone and ethanol for 30 minutes each, followed by rinsing with MilliQ water and drying with N_2 gas prior to immobilization.

Direct Immobilization.

Cleaned wires were incubated with antibodies (in buffer solutions with pH 5, 7, 8, and 9) for 6h. After incubation, the wires were washed with corresponding buffers. The wires were placed in 1% BSA (overnight at 4ºC). MES buffer was used with pH 5, and a Tris buffer with a pH of 9 was used. Acetic acid was used to make the pH 8 and pH 7 buffers by gradually adding the acid to the solution and measuring the pH until the desirable pH was obtained.

Covalent Immobilization.

Before immobilizing the antibodies, the cleaned wires were incubated with 1, 5, 10, and 20 mM lipoic acid in absolute ethanol for 12-16 hours, as shown in Figure 3-8. Lipoic acid was used to carboxylate the surface of the wires that could be later activated using EDC to have a covalent

bond with an amine group of the antibodies. After washing with absolute ethanol and MES buffer, the wires were incubated with freshly prepared EDC (40 mM in MES) and NHS (20mM in MES) for 30 minutes. Then, the wires were washed with MES, followed by adding the antibody solution (500 µg/mL) to the wires. After 2 hours, the wires were washed with MES and were incubated with BSA solution (1% w/v in MES) for another 2 hours at 37°C. At last, the wires were washed with MES and kept at 4ºC before use.

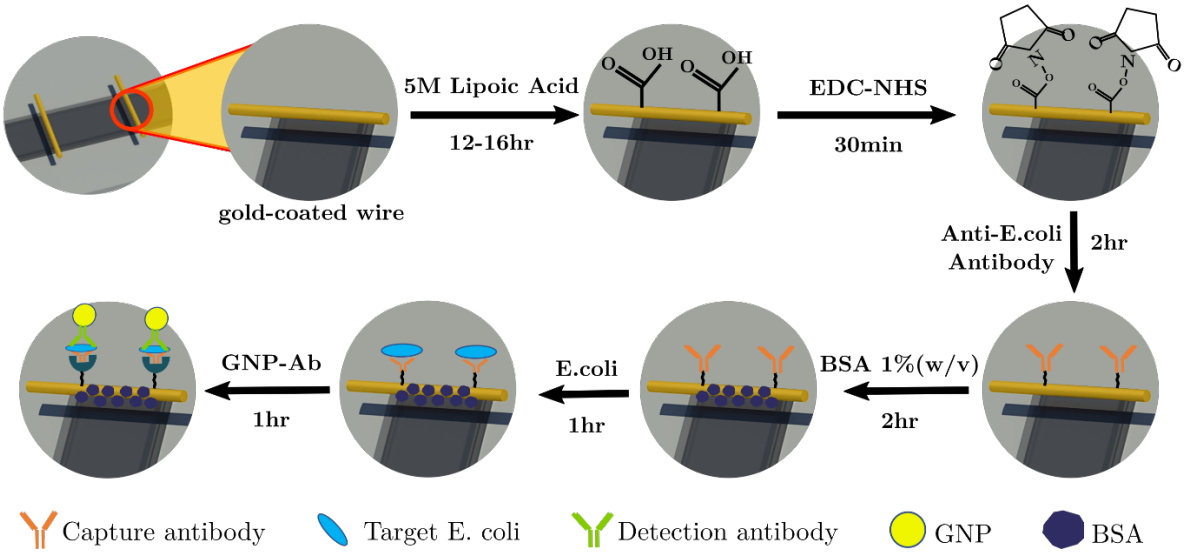

Figure 3-8. Antibody immobilization process, bacteria capturing, and GNP tagging are shown.

3.2.4 Electrical Sensor Fabrication and Experimentation

A few differences in fabrication and experimentation will be discussed in this sub-section. The device fabrication was slightly different from the salinity sensor. The Ab-immobilized wires were located inside the PDMS layers of the device after plasma oxidization of the two layers to prevent adverse effects of the plasma process on the antibodies. As placing the wires after plasma caused a delay in bonding, bonding efficiency was reduced, and paper clips were occasionally used to ensure no leakage. However, the effect of using paper clips was removed by normalization to the baseline. Another difference was the duration of the tests. Electrical measurements were performed

for 100 seconds as the current was swept from 10nA to 1μA. Data analysis and averaging were carried out on the steady-state section of the recorded data, spanning from 60 seconds to 100 seconds. Other aspects of experimentation were similar to salinity detection.

3.2.4.1 Bacteria Samples Preparation

The *E. coli* K12 samples were prepared by diluting 1mg of the lyophilized bacteria in 10 mL of the buffer to obtain 3×10^7 CFU/mL. Bacteria samples with different counts were prepared by serial dilution and were used in the experiments.

3.2.4.2 Gold Nanoparticle Conjugation to Detection Antibody

The GNPs were conjugated with detAb to attach to the bacteria. The following protocol was used for conjugation. All glassware was first washed with aqua regia (3:1 ratio of HCl to HNO3). Then, they were washed extensively with distilled water and dried. Exposure to dust and any dirt was avoided until used. Then, the gold nanoparticles' temperature was adjusted to room temperature (about 25 °C), and their pH value was adjusted to 9.0. For the adjustment, 0.5 M K2CO3 (filtered through a 0.22 μM filter) was used. The pH of the colloidal solution was not stable at this point and was not stored after pH adjustment. The solution was titrated with acid if the pH was over-titrated (pH >9.0). After adjusting pH, the colloidal solution was mixed with antibodies (final concentration – 10-15 μg of antibodies per 1 mL of colloidal solution). The ionic strength of the antibody stock solution was not high (<100 mM PBS). If the stock of antibodies was high ionic strength, antibodies were diluted, or dialysis/buffer replacement was performed. After mixing antibodies with gold nanoparticles, the colloidal solution was more-less the same colour. If the solution turned violet-blue, it meant nanoparticles' aggregation, which was undesirable. In this case, the ionic strength of antibodies buffer was reduced, or the pH of immobilization was optimized.

Next, the mixture of antibodies was incubated with gold nanoparticles with constant stirring for 2-3 hours. The BSA from the stock solution (10% in distilled water, filtered through a 0.22 μM filter and containing 0.05% NaN3 as preservative) was added to the final concentration of 0.25% (i.e., 40-times dilution) and was incubated for 5 min. Nanoparticles were centrifuged (16,000 g for 15 min at 4 °C) toward obtaining concentrated solutions for storage at 4°C. The size of the nanoparticles determined the g-values. For large particles, a lower g-value should be used. Too high g-values will result in the aggregation of nanoparticles. Too low g-values will result in poor precipitation of particles (particles stay in solution). After centrifugation, the supernatant was carefully removed using a pipette while shaking and mixing of the supernatant were averted. The supernatant was removed without taking particles. Lastly, concentrated particles were redispersed in the required buffer. The colour of the particles was obtained as red; violet-blue coloration indicated aggregation.

For verification purposes, the optical spectra of the concentrated particles should be recorded. The expected wavelength max is within 520-530 nM, and the absorbance value is determined by the concentration factor (ratio of volumes before and after centrifugation).

3.2.5 Data Analysis

All the statistical analyses in this study were conducted using Minitab 20. Levene's test was applied to examine the homogeneity of variances prior to conventional one-way ANOVA. If the test showed a significant result ($p<0.05$), then Welch's ANOVA was conducted instead of a one-way ANOVA. Also, when ANOVA showed a significant difference between the mean values, a post hoc pairwise analysis was performed to identify which pairs of means were significantly different. Tukey HSD post-hoc pairwise comparison was conducted for datasets with homogenous variances, and the Games-Howell post hoc test was adapted for those with inhomogeneous variances.

For the NaCl detection, the limits of detection (LOD) and quantification (LOQ) were determined as salt concentrations with resistances equal to DI water resistance (R_{DI}) minus three and ten times its standard deviation (SD), respectively (i.e., $R_{LOD}=R_{DI}-3SD_{DI}$ and $R_{LOQ}=R_{DI}-10SD_{DI}$).

Each set of results was normalized with measured baseline resistance to eliminate the variability between devices. The baseline resistance would correspond to R_0, at 0 ppm NaCl (blank DI water) for salt detection and 0 CFU/mL buffer in bacteria detection. The fold change method (R/R_0) was used for normalization, and data points at each concentration were divided by the mean resistance value of the baseline.

Chapter 4: Results and Discussion

In this chapter, numerical and experimental findings of the thesis will be presented and discussed.

4.1 Salinity Detection

4.1.1 Primary Sensor Experimental Evaluation

We measured the primary sensor's electric resistances for salty water samples with NaCl concentrations of 1-20ppm flown at a flow rate of 1 mL/min in the channel, as shown in Figure 4-1 (four replicate devices, each tested seven times). The sensor had a transient response at the beginning of the experiment, followed by a steady-state plateau (Figure 4-1). The transient effect is mainly a result of the sudden implementation of an external electric field intrinsic to measurement systems [26]. It usually dies out over time, and the device would reach a steady-state that is suitable for measurement[26]. Another reason for the transient mode presumably resulted from changes in the ionic composition of the medium around the wires when the current was applied. Samples with NaCl concentrations lower than 5ppm exhibited shorter transient modes (~10 s), and the duration was increased at higher concentrations (~25 s). A relatively stable plateau was observed for all the concentrations once the steady-state regime was reached (after 30 seconds; See Figure 4-1 insets).

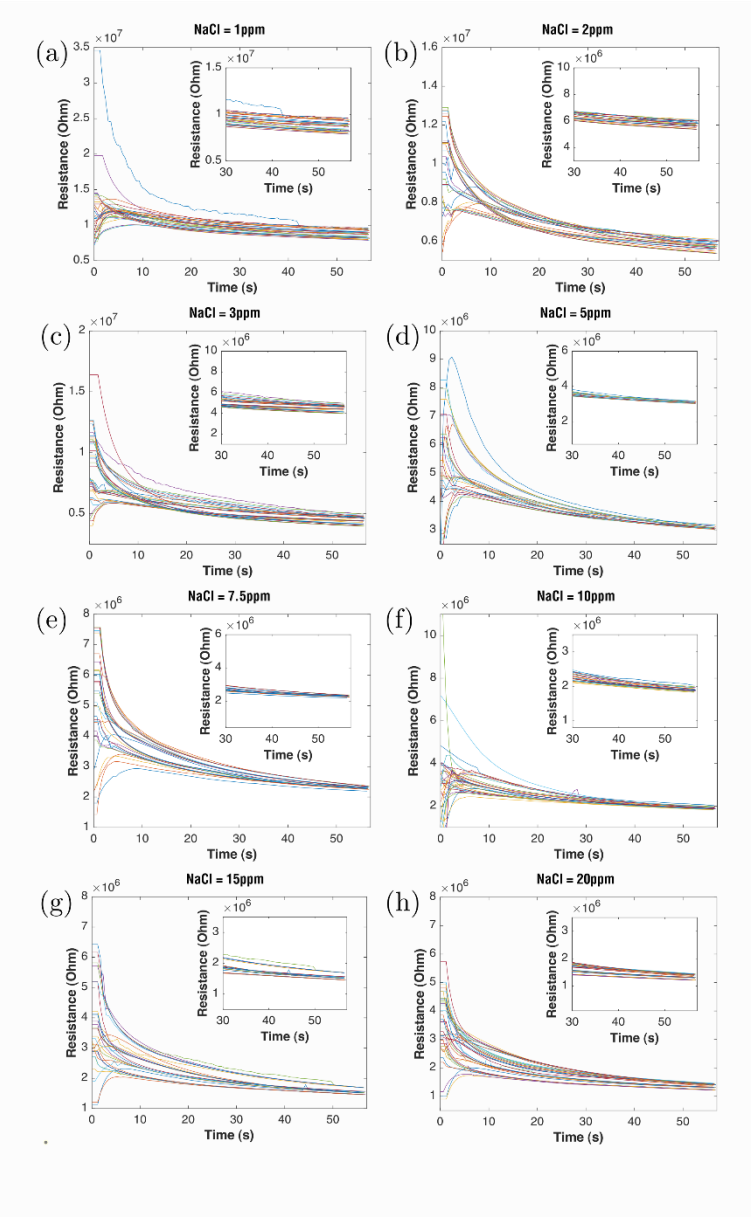

Figure 4-1. Dose-response measurements of the primary salinity sensor. Electrical resistances were recorded as the current was swept from 10 nA to 1 μA during 56 seconds. Results are shown for samples with (a) 1, (b) 2, (c) 3, (d) 5, (e) 7.5, (f) 10, (g) 15, and (h) 20 ppm of NaCl in DI water. Samples were flown in the microchannel at a 1 mL/min flow rate. The insets depict the 30-56 seconds intervals of the resistance measurements. Each panel consists of 28 recorded measurements from 4 replicates and 7 measurements. Repetition experiments in each plot are represented with different colours.

The resistance values in the range of 30-56 seconds, corresponding to the current range of 0.5 μA to 1 μA, showed a gradual decrease. Analysis of this data showed that the resistance changes in

the last 30 seconds of the experiments were smaller than the standard deviations (SD) in the same duration (Figure 4-2). Thereby, the recorded data in the 30-56 seconds of each experiment was inferred as the steady state plateau and used to obtain the resistance means and standard deviations for correlation to NaCl concentration in the samples.

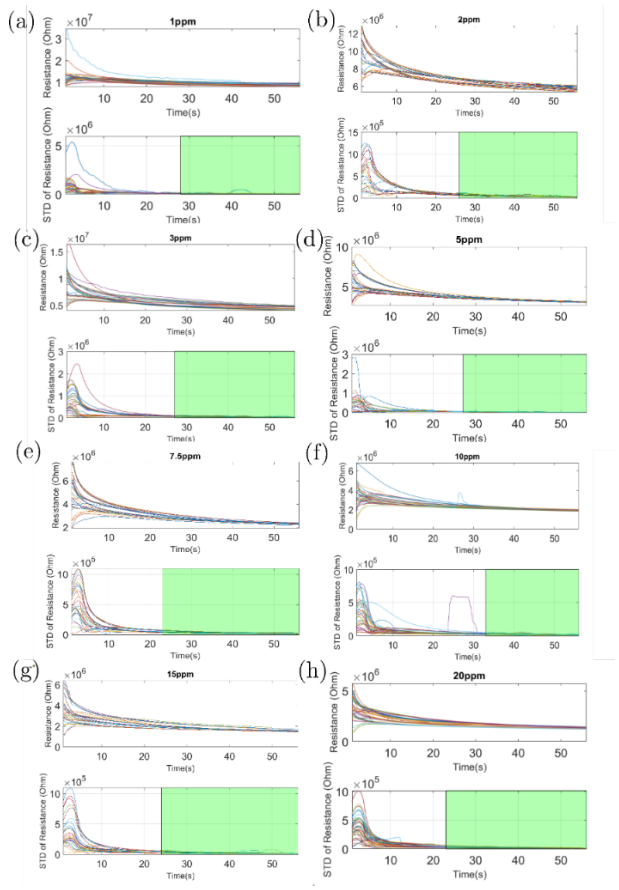

Figure 4-2. Resistances were recorded as the current was swept from 10nA to 1μA during 56 seconds and samples with (a) 1, (b) 2, (c) 3, (d) 5, (e) 7.5, (f) 10, (g) 15, and (h) 20ppm NaCl were infused into the microchannel of the primary sensor at 1 mL/min. The top plots of each figure panel depict the transient electrical resistances and the bottom plots demonstrate the standard deviation of signal throughout the 56 seconds. In the bottom subfigures, an algorithm was used to apply a green patch to the dataset as the standard deviation becomes smaller than the standard deviation of the 30-56 seconds, a plateau is reached. Each panel consists of twenty eight recorded measurements from four replicates and seven measurements. Colors denote experimental repetitions.

Figure 4-3 illustrates the electrical resistance means and SDs from the four replicated devices at different NaCl concentrations. The results show that different replicates had comparable readouts at each concentration as the error bars of replicates overlapped. Results qualitatively demonstrate that measurements were reproducible and reliable with no overlap between the error bars of any two concentrations. However, there are wider gaps between resistances of the samples with lower salinities (e.g., ΔR=~1.6 MΩ between 2 and 3 ppm NaCl vs. ΔR=~300 kΩ between 15 and 20 ppm NaCl). To compare the device readings quantitatively, we performed a one-way analysis of variance (ANOVA) test to examine if the sensor could statistically distinguish the difference among the samples. Statistically significant differences between the resistance mean values of different concentrations were observed ($p<0.0001$). Games-Howell post hoc test was adopted to conduct a pair-wise comparison for different concentrations. An effect size of 3.58 with a statistical power of 0.9 was obtained at a significance level of 0.05 and a sample size of 7 for each concentration. It was then established that the sensor could distinguish different tested concentrations, and the statistical difference for every two concentrations would be sufficiently large with at least 7 repetitions.

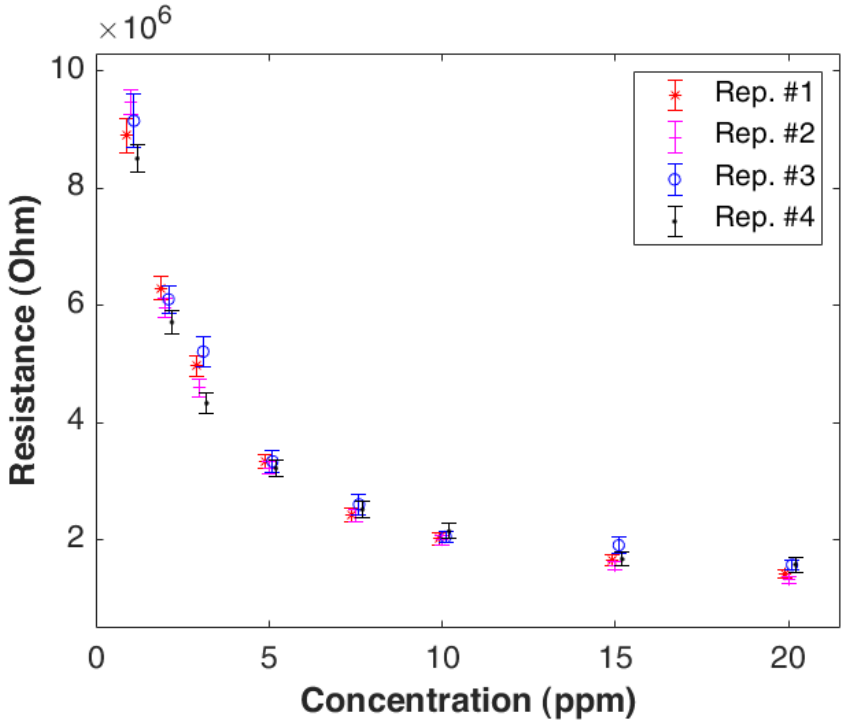

Figure 4-3. The averaged electric resistances of four replicate devices with 7 repetitions at different NaCl concentrations.

The raw resistances in Figure 4-3 were normalized with respect to measured DI water resistances to eliminate inter-device variabilities, as depicted in Figure 4-4. As shown, the normalized resistance decreases with an increase in salt concentration due to the rise in the number of ions between the two wires. Similar statistical analyses to the ones described for Figure 3a were performed with the normalized data in Figure 4-4, and identical results were achieved in terms of distinguishing between various salt concentrations ($p<0.0001$).

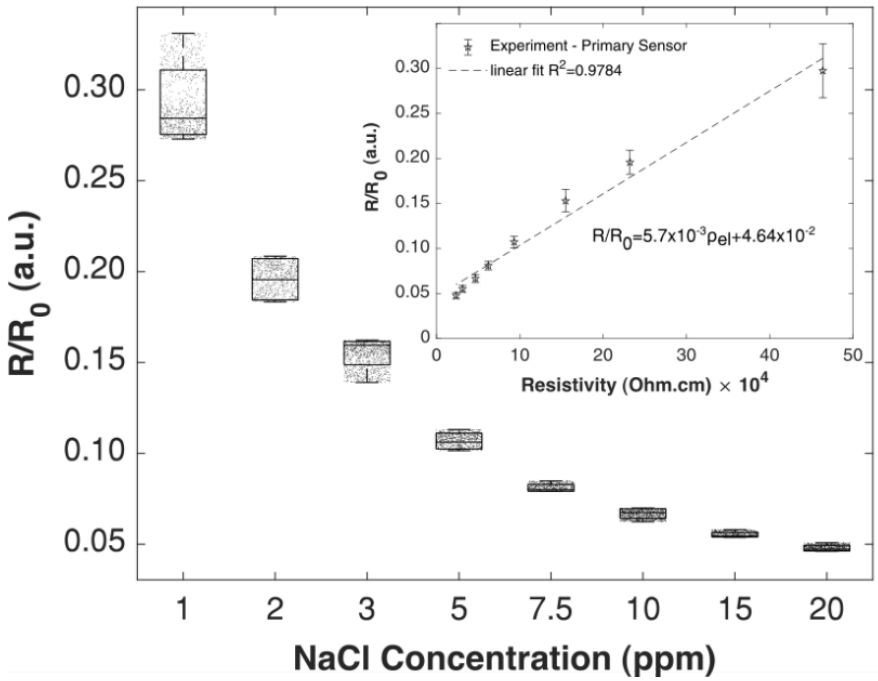

Figure 4-4. Normalized dose-response measurements of the primary salinity sensor. To eliminate inter-device variability, we normalized the results of each replicate with their baseline values at 0 ppm NaCl, and the normalized mean values and standard deviations are shown versus samples NaCl concentrations and resistivities. The calibration curve fits the experimental data.

Figure 4-4. inset depicts the normalized mean resistances correlated to the electrical resistivities of the samples, calculated according to Debye–Hückel–Onsager equation (3-10). The samples with lower NaCl concentrations would have higher resistivities. A linear relationship between the resistance and resistivity in equation (3-6) allows establishing the sensor's calibration curve as:

$$\frac{R}{R_0} = 5.7 \times 10^{-3} \rho_{el} + 4.6 \times 10^{-2} \qquad (4\text{-}1)$$

A goodness of linear fit of 97.84% was achieved for equation (4-1). Disregarding the 1 ppm concentration in the curve fitting process (since it demonstrated more noise than the other concentrations) would increase the goodness of the fit to 99.26%. Thereby, the sensitivity of the sensor based on the primary design was found as 17.1 Ohm/Ohm.cm. The blank DI water

resistance in the primary sensor was R_{DI}=$(30.1 \pm 7.04) \times 10^6$. Accordingly, the limit of detection (LOD) and limit of quantification (LOQ) were calculated to be 0.31 ppm and 0.37 ppm according to 3SD and 10SD methods, respectively. The device was observed to be saturated beyond the 20ppm in the primary design. The primary sensor's calibration curve could be also expressed with a second-degree polynomial function as $\frac{R}{R_0} = -6.74 \times 10^{-5}{\rho_{el}}^2 + 8.9 \times 10^{-3}\rho_{el} + 2.7 \times 10^{-2}$ that increases the goodness of the fit to 99.99%.

4.1.2 Numerical Optimization of the Sensor

To increase the sensor's sensitivity and its detection range, further optimization studies were warranted. For rapid optimization, a numerical model of the primary sensor based on the experimental results of Figure 4-3 and Figure 4-4 was developed, verified, and validated, then applied in a parametric study to determine the most contributing device parameters. In this sub section, we will first review numerical model's domain and mesh independency which will be followed with verification and validation.

4.1.2.1 Domain Independency

The channel length (along the x-axis) in the numerical model was assumed to be smaller than the actual experimental sensor (20 mm) to reduce the numerical load. To ensure that this measure would not influence the results, the effect of channel length was studied in a series of simulations. We studied the effect of decreasing length from 20mm to 2mm and obtained the velocity magnitude and current density (in the x-axis) along an arbitrary vertical line (along the y-axis) in the middle of the two wires. As shown in Figure 4-5, smaller channel lengths would not perturb the numerical results, e.g., velocity magnitude and current density, and the changes were infinitesimal. Thereby, the microfluidic channel length was set to 3 mm in the numerical simulation.

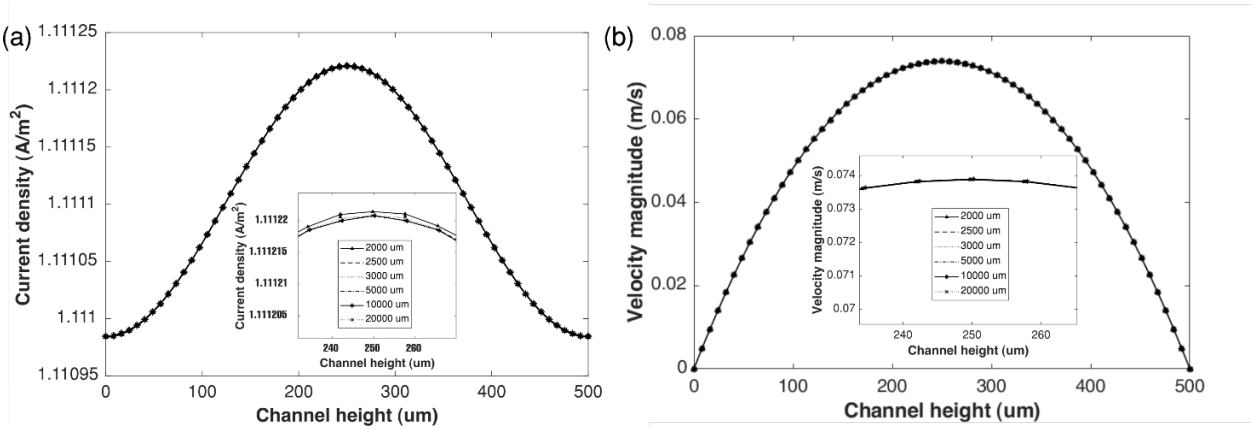

Figure 4-5. Domain independency study of the primary sensor model. The (a) electric current density and (b) fluid velocity in the x-axis direction is plotted along an arbitrary vertical line (along y-axis) in the channel height direction, for four microchannel lengths of 20, 10, 5, 3, 2.5, and 2mm in the legend.

4.1.2.2 Mesh Independency

Mesh independency was investigated by simulating the geometry of the primary sensor using six triangular meshing conditions with mesh elements ranging from 2,000 to more than half a million with element sizes ranging from 0.026 to 14 μm to ensure high accuracy around the wires. As depicted in Figure 4-6, the current density and velocity magnitude are plotted between the two wires and along the x-axis and y-axis to evaluate the results based on different mesh configurations, respectively. The first configuration with 2,306 mesh elements resulted in a significant deviation from the rest of the arrangements in the current density and thereby disregarded as it would produce unreliable results if employed. The remaining five configurations were similar at the first glance. The insets in Figure 4-6a and Figure 4-6b show magnified views of the five arrangements in a plot section. It was established that increasing the number of mesh elements to more than 191,026 would result in a deviation of only 0.07%. Therefore, to maintain accuracy and minimize the computational load, this mesh configuration (191,026 elements) was selected to be used in our study. There is a valley between the two peaks in the velocity magnitude since the velocity magnitude was studied on a vertical line between the two wires. The presence of the wire in the

channel just before the studied line is the reason the velocity profile was disturbed, and valley was observed.

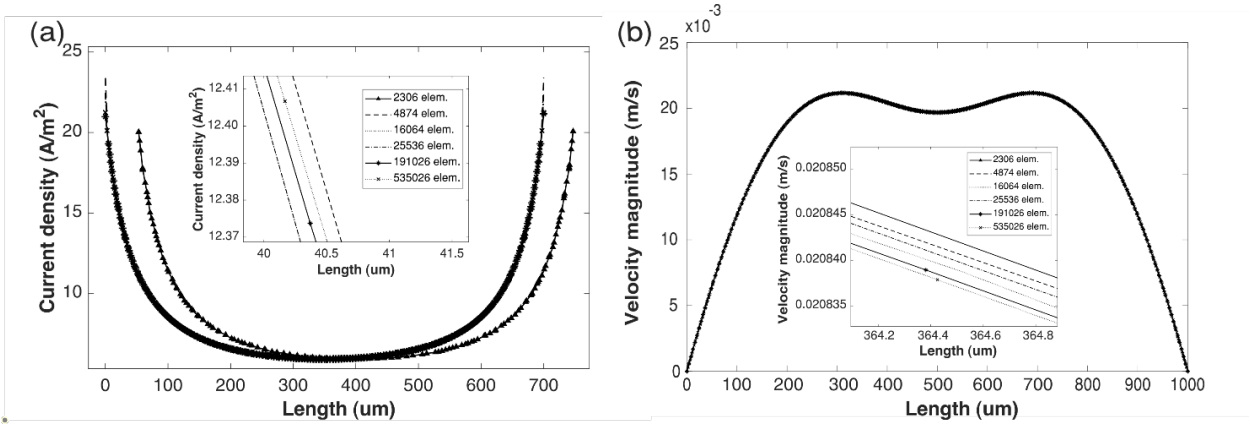

Figure 4-6. Mesh independency study of the primary sensor model. (a) Electric current density between the wires in the x-axis direction and (b) fluid x-velocity along the y-axis in six different mesh configurations ranging from 2,000 to half a million elements were plotted.

4.1.2.3 Model Verification

To verify the model, we examined several basic physical phenomena that were expected with our numerical method (results not shown). For example, the fluid flow showed a parabolic pattern through the microfluidic channel. The electrolyte conductivity increased at higher salt concentrations, resulting in lower electric resistance values. The electric potential decreased from its initial value to zero from the terminal to the ground. The ions migration was observed, and Na^+ and Cl^- ions accumulated around the ground and terminal electrodes due to potential differences, respectively. The accumulation of ions around the wires was increased as the salt concentration was raised in the sample. The fluid flow caused the convection of accumulated ions around the wires and reduced the effective ions in the current transfer. The above observations agreed well with the sensor's physics and verified the correct performance of the model.

4.1.2.4 Model Validation

We then validated our numerical model by comparing our results with the obtained experimental resistance values from the primary sensor. Figure 4-7 depicts the recorded electrical resistance mean values in the experimental study and the numerical study in the range of 1-20 ppm, corresponding to resistivities of 46.4 $\times 10^4$ to 4.5$\times 10^4$ Ω.cm. As expected, the resulting resistances from the simulation show a perfectly linear behavior ($R=2.52\times 10^5 \rho_{el}$; $R^2=1$). There was a deviation between the two datasets as the simulation did not consider the experimental errors. As the simulation could not completely mimic experimental conditions, a transfer function was defined so that the user could obtain experimental values using the simulated model and compensate for the observed deviation. We derived the transfer function of the system by dividing the line equations of the two datasets from numerical and experimental results of the primary design in the range of 1-20ppm, corresponding to resistivities of 46.4 $\times 10^4$ to 4.5$\times 10^4$ Ω.cm (See Figure 4-7).

$$\text{Transfer Function} = 0.68 + \frac{0.78}{\rho_{el}} \tag{4-2}$$

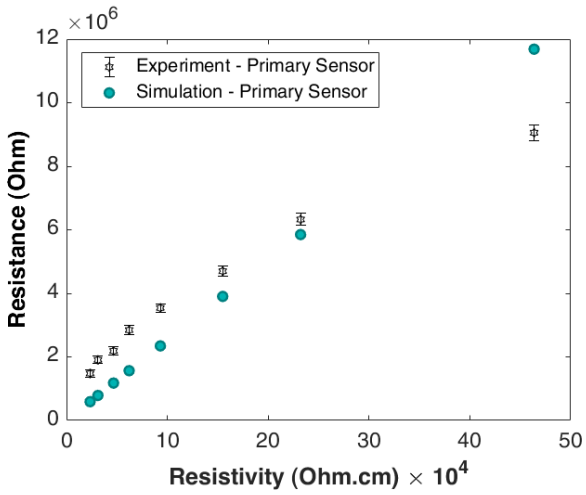

Figure 4-7. The numerical simulation results are shown compared to the experimental findings.

4.1.2.5 Parametric Optimization Study

The numerical optimization study was carried out with a full factorial parametric approach. The effects of six parameters with three levels were examined on the sensor performance as tabulated in Table 4-1. The minimum channel height and width levels were selected based on fabrication restrictions using 3D printing. The wire diameters were chosen from several available choices in the market. The effects of changing the fluid properties and flow rate were also studied using the Reynolds number. The study involved 3^6=729 combinations, and each combination was simulated for 1-20 ppm NaCl concentrations.

Table 4-1. Numerical optimization study parameters and levels. The P-values were achieved through a full factorial design for each parameter.

Parameter	Levels			P-value
	Low	Medium	High	
Channel height (h) [µm]	150	250	500	<0.001
Channel width (w) [µm]	200	500	900	<0.001
Interwire distance (g) [µm]	1000	1500	2000	<0.001
Wire diameter (d_w) [µm]	90	110	130	0.973
Electric Current (I) [nA]	1	100	1000	1.00
Reynolds number (Re)	16	32	64	0.998

The results of the optimization study are shown partially in Figure 4-8. Our simulations showed that the channel width, channel height, and interwire distance had the most significant effects on the sensor's performance, determined by examining the increase in resistance compared to the primary sensor; these observations were also confirmed by ANOVA test (Table 4-1). Low levels of the channel width and height caused the highest increase in resistance value as the sensing

medium was shrunk (h×w would decrease in equation (3-6)). On the other hand, the effect of increasing the interwire distance was not as intense as the channel height and width. The reason is that as g increased, there were two opposing effects on the resistance, i.e., an increase as there was more electrolyte with small conductivity and a decrease as the electric field was weakened when the two electrodes moved further apart.

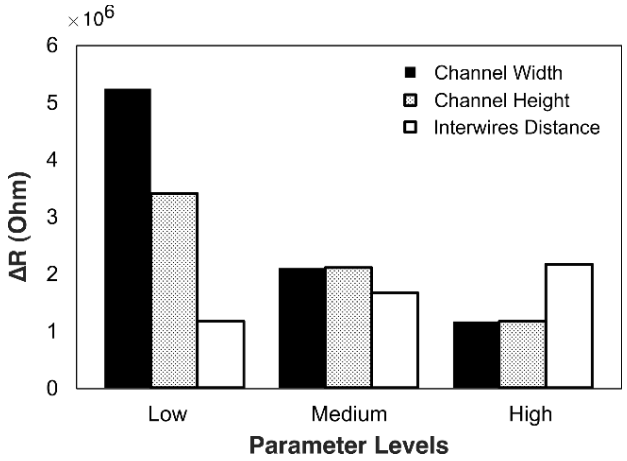

Figure 4-8. Effect of the most contributing parameters at different levels on the electrical resistance of the sensor. The increase in resistance compared to the primary sensor is plotted. The optimized design parameter configuration should be composed of low levels of channel width and height and a high level of interwire distance, resulting in g=2000 μm, w=200 μm, and h=150 μm.

We found that the electrode diameter, electric current and Reynolds number had no statistically significant effect on the resistance (P-values close to 1 in Table 4-1). Changing the electric current resulted in similar changes in voltage that left the resistance intact. The fluid flow was always in the laminar regime and did not significantly reduce the effective concentration of the ions in the electric circuit to cause changes in the resistance. It was counterintuitive that the wire diameter had no significant impact on sensor performance as increasing the electrode surface was expected to allow for better electron transfer. However, we hypothesize that as the salt concentrations were scarce, the wires surface area was more than enough for the ions to transfer electrons. To

investigate this hypothesis, we simulated smaller wire diameters in the range of 1-130 µm and studied the discharged current density on the wire surfaces (Figure 4-9). There was less than 10% difference in current densities between wire diameters of 90, 110, and 130 µm. This is also in agreement with our findings from Table 2 that wire diameter did not have significant contribution.

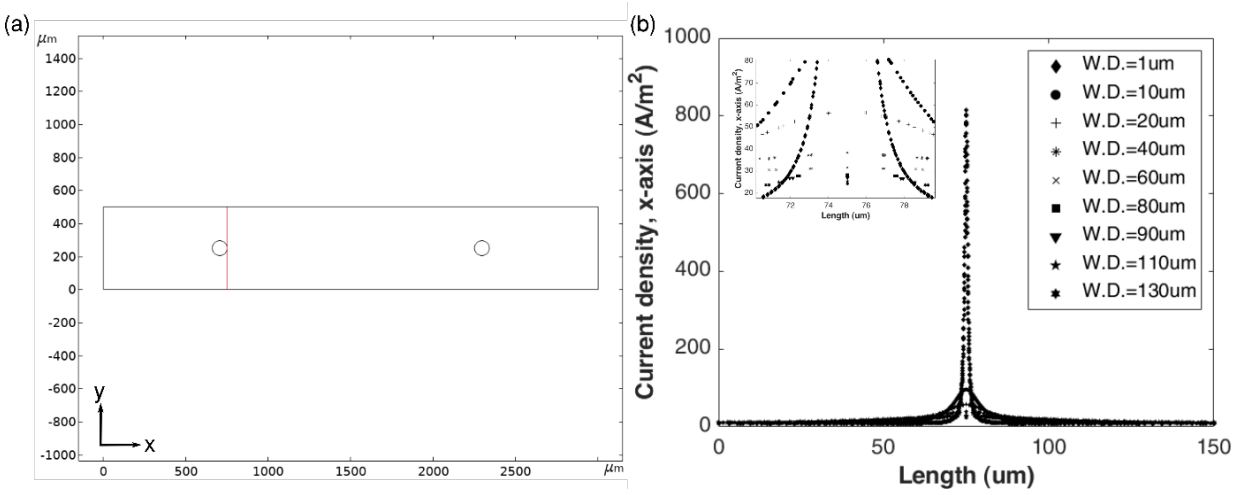

Figure 4-9. Numerical study of the effect of wire diameter on the current density discharge in the primary sensor. (a) A tangential cut-line is drawn next to the wire along the y-axis and (b) the current density along this cut-line in the y-axis direction is plotted.

According to Table 4-1 and Figure 4-8, the optimized sensor should have the dimensions of g=2000 µm, w=200µm, and h=150 µm. This finding is in agreement with equation 3-6) as increasing and decreasing the cross-section area and interwire distance, respectively, would result in a wider range of resistances and, thereby, higher sensitivity. The achieved resistances, calculated through simulation, were plotted against NaCl solution resistivities for the optimized and primary designs in Figure 4-10. It is estimated that the sensitivity of the optimized sensor would increase 27-fold compared to the primary sensor. This estimation will be further investigated in experimental analysis in the next section.

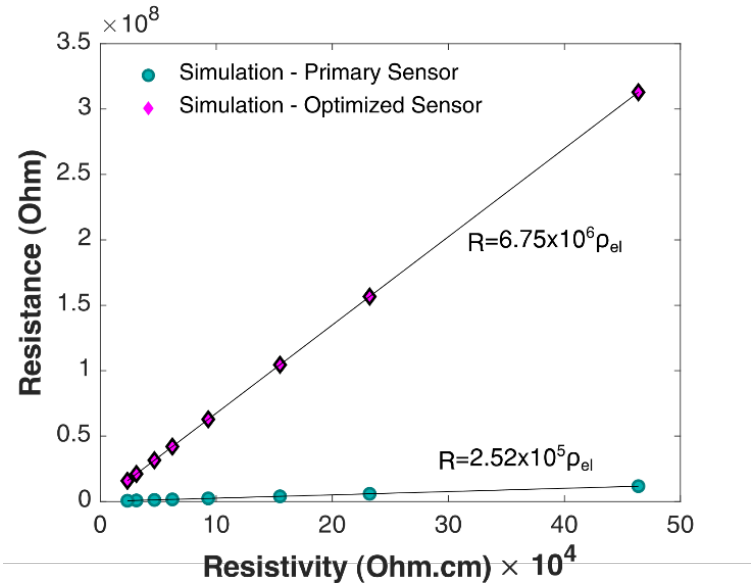

Figure 4-10. Numerically calculated electrical resistance versus saltwater resistivity for the primary and optimized sensors. The numerical model predicts 27-fold higher sensitivities with the optimized sensor compared to the primary one.

4.1.3 Experimental Analysis of the Optimized Sensor

To evaluate the optimized sensor after fabrication, we performed the same experimental procedures as the preliminary device (See Figure 4-11). Figure 4-12 illustrates the electrical resistance means and SDs at different NaCl concentrations in the optimized sensor (d_w=90 µm, g=2000 µm, w=200µm, and h=150 µm). Similar to the primary sensor, the resistance decreases as the ions population increases, and the electron transfer improves. Also, there are wider resistance variations between replicates of samples with less than 3 ppm NaCl concentrations. The analysis of variance and Games-Howell post hoc analyses were performed. It was obtained that there is a statistically significant difference between all and each pair of concentrations with a 0.01 significance level for both analyses ($p<0.0001$). An effect size of 2.89 with a statistical power of 0.99 was obtained at a significance level of 0.01 and a sample size of 5 for each concentration. The analysis demonstrated that the sensor could distinguish different tested concentrations, and the

statistical difference for every two concentrations would be sufficiently large with at least 5 repetitions.

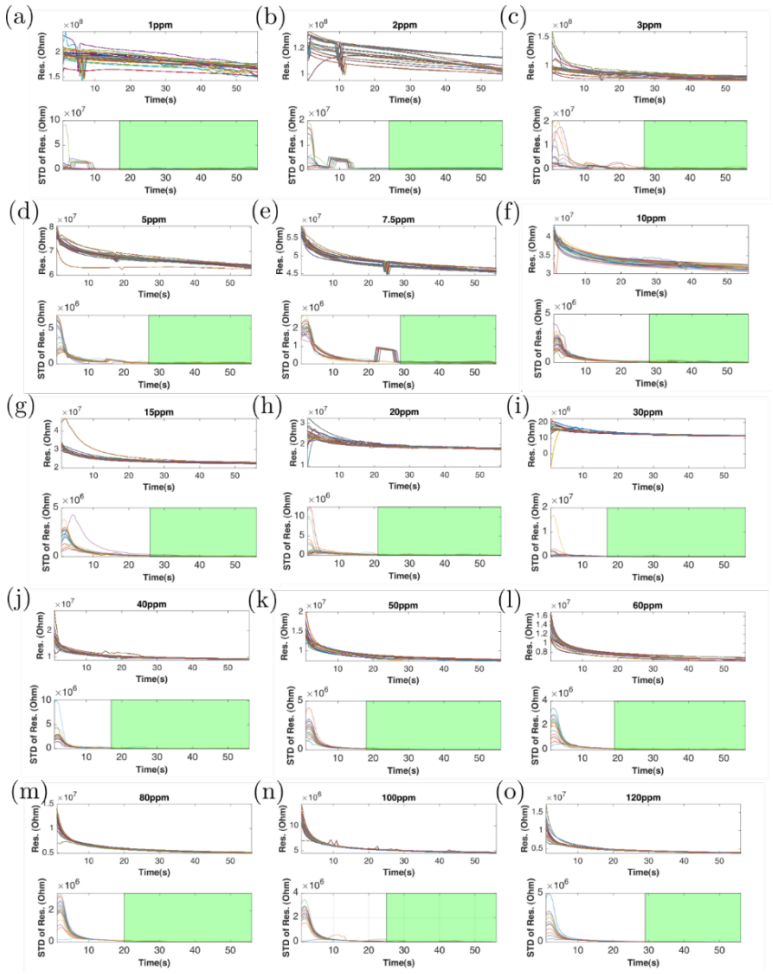

Figure 4-11. Resistance is recorded as the current is swept from 10nA to 1μA during 56 seconds as samples with (a) 1, (b) 2, (c) 3, (d) 5, (e) 7.5, (f) 10, (g) 15, (h) 20, (i) 30, (j) 40, (k) 50, (l) 60, (m) 80, (n) 100, and (o) 120 ppm NaCl are infused into the optimized sensor at 0.2 ml/min. The top plots of each figure panel depict the transient electrical resistances and the bottom plots demonstrate the standard deviation of signal throughout the 56 seconds. In the bottom subfigures, an algorithm was used to apply a green patch to the dataset as the standard deviation becomes smaller than the standard deviation of the 30-56 seconds, a green patch would be shown from that moment to the right side of the plot, indicating a plateau is reached. Each panel consists of fifteen recorded measurements from three replicates and five measurements. Colors denote experimental repetitions.

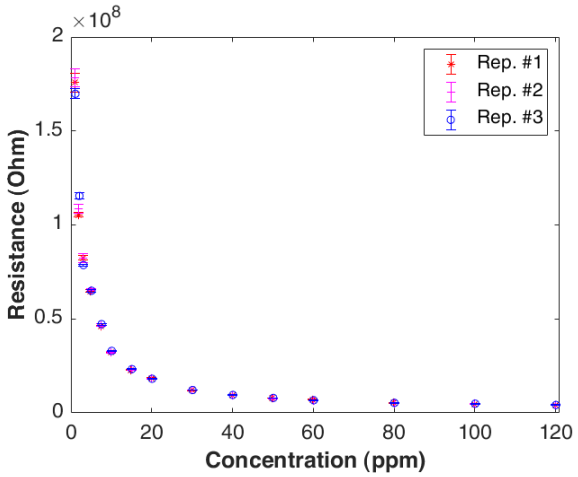

Figure 4-12. Dose-response experimental measurements of the optimized salinity sensor. The measured electric resistances of three replicate devices at different NaCl concentrations.

The raw resistance values (R) in Figure 4-12 were normalized to eliminate inter-device variability, as in Figure 4-13. Moreover, the normalized values were plotted against the resistivity to establish the sensor's linear calibration curve, expressed in Figure 4-13 inset and equation (4-3).

$$\frac{R}{R_0} = 7.8 \times 10^{-3} \rho_{el} + 2 \times 10^{-2} \qquad (4\text{-}3)$$

The goodness of linear regression was found to be of R^2=96.49%. Neglecting 1, 2, and 3 ppm NaCl concentrations would increase R^2 to 99.76%. Comparing the primary and optimized sensors' calibration curves, we found that the sensitivity increased an order of magnitude to 385 Ohm/Ohm.cm with averaged data (further discussed on Figure 4-13 . The higher sensitivity allowed the sensor's detection range to be widened by 6-fold, increasing it from 1-20ppm to 1-120ppm. The device was observed to be saturated beyond the 20ppm and 120ppm in primary and optimized designs, respectively. The blank DI water resistance in the optimized sensor was $R_{DI}=(491.2 \pm 8) \times 10^6$. Accordingly, the LOD and LOQ was calculated to be 0.39 and 0.44 ppm using 3SD and 10SD methods, respectively, which was almost equivalent to the primary design.

The optimized sensor's calibration curve could be also expressed with a second-degree polynomial function as $\frac{R}{R_0} = 10^{-4}{\rho_{el}}^2 + 1.2 \times 10^{-2}\rho_{el} + 7 \times 10^{-3}$ that increases the goodness of the fit to 99.99%.

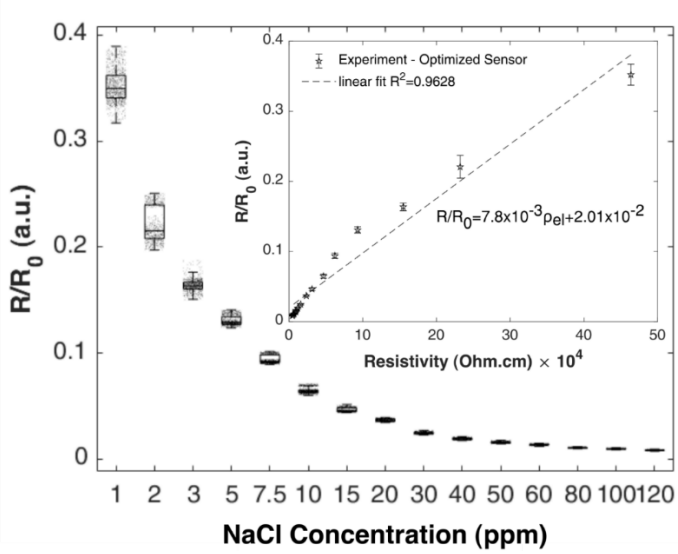

Figure 4-13. To eliminate inter-device variability, results of each replicate in (a) were normalized relative to their baseline values at 0 ppm NaCl and the normalized mean values and standard deviations are shown versus samples NaCl concentrations and (inset) resistivities. The calibration curve fit to the experimental data is also shown in the inset. The error bars represent standard deviations.

The overall performance of the two sensors was re-plotted under both experimental and numerical conditions in Figure 4-14a. The first three concentrations of NaCl at 1, 2 and 3ppm (46.37-15.49×10^4 Ω.cm resistivity range) had a lower signal-to-noise ratio and brought about the highest deviation from the simulation findings. As previously mentioned, this deviation resulted from simulation ideal intrinsic quality in not considering experimental errors. This deviation is observed as the experiment and simulation results are compared for the case of the optimized sensor (Figure 4-14). However, the simulation results are in better agreement with the experimental findings in the range of 5-120ppm (corresponding to 9.31- 0.39×10^4 Ω.cm resistivity range), as illustrated in Figure 4-14b, with an average deviation of 12%. As the simulation could not completely mimic

experimental conditions, a transfer function was calculated and applied to experimental results. The transfer function was established as a result of dividing equation (4-3) and optimized sensor numerical equation ($R=6.75 \times 10^{6}\rho_{el}$) and is expressed in (4-4).

$$\text{Transfer function} = 0.57 + \frac{1.484}{\rho_{el}} \qquad (4\text{-}4)$$

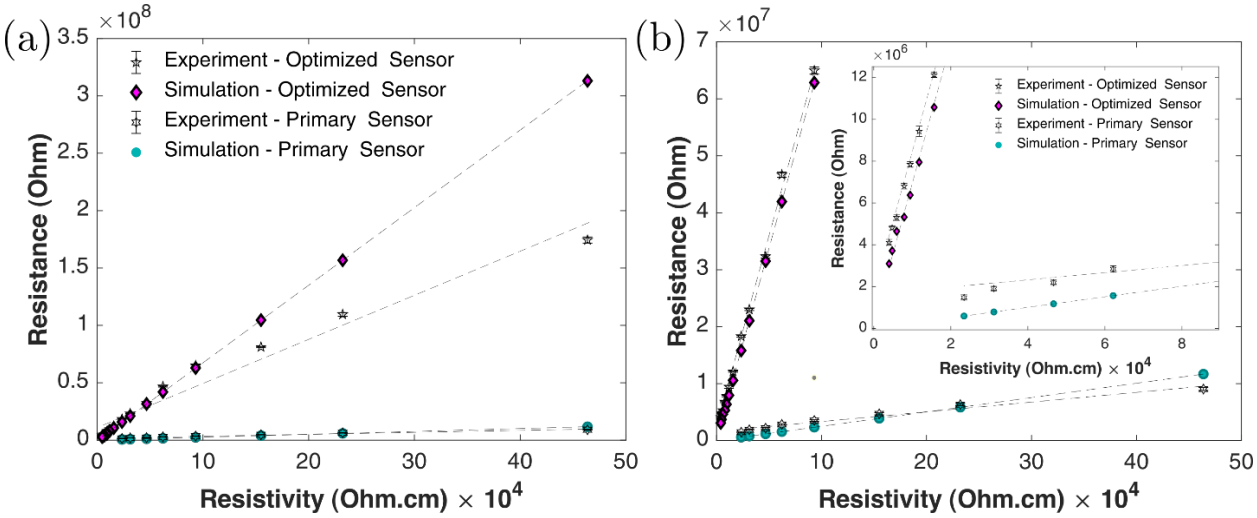

Figure 4-14. Comparison of the dose-response measurements of the primary and optimized sensors in our experimental and numerical analyses. (a) The optimized model has higher theoretical and experimental sensitivities and allows a detection range of 1-120 ppm NaCl (46.37- 0.39×10⁴ Ω.cm) compared to 1-20ppm (46.37- 2.34×10⁴ Ω.cm) for the primary sensor. (b) The optimized sensor results are illustrated in the range of 5-120 ppm NaCl (9.31- 0.39×10⁴ Ω.cm) that has the least deviation between the simulation and experimental results. The inset magnifies the 7.5-120ppm NaCl (6.21- 0.39×10⁴ Ω.cm) range for the optimized sensor.

As shown in Figure 4-14a and Figure 4-14b, the slope of the primary sensor fitted line is 17.1 Ohm/Ohm.cm with the pre-normalized data, which in comparison to the optimized sensor slope of 385 Ohm/Ohm.cm (1-120ppm) or 692.4 Ohm/Ohm.cm (5-120ppm), shows a significant improvement in the sensitivity of the optimized sensor.

4.1.4 Discussion on Salinity Sensor

The experimental evidence showed the sensor's reliability, making it a promising candidate for different applications such as surveillance of water in different settings. The proposed sensor is a total conductivity sensor and thereby, differences in conductivity of the tested samples would change the output resistance signal. Such characteristic allows for installing the sensor for continuous monitoring of water conductivity levels. It can be installed at the outlet of water treatment facilities, consumed source or tap waters to constantly monitoring the conductivity ranges of the water prior to consumption by comparing it to pre-established safe levels. Whenever the conductivity levels show a divergence from the safe-to-drink amounts, the consumers will be warned not to consume the water until further official investigations into the source of potential contamination.

For successful sensor implementation for continuous monitoring of drinking waters, there should be several considerations. First, the sensor must be calibrated for each installation location and safe drinking water's conductivity magnitudes must be established and known. As conductivity magnitudes change geographically and seasonally, knowing possible variations in conductivity would ensure detection of contaminations only. Second, the sensor is designed for detection of contamination in aesthetically appealing drinking waters and not waters with high turbidity. As the sensor relies on measuring conductivity of the water samples, any interference in sensor's electrical field might impair its performance and raise false alarms. To prevent such occurrences, the tested samples must be filtered prior to detection to ensure removal of large particulates of clay, rocks, and/or other materials that might also affect water turbidity and clarity.

As mentioned, the sensor is made of two PDMS layers and two microbridge wires that contributes to sensor's simplicity in detection and fabrication. The average cost of two top and bottom PDMS

parts, considering each to be 3 grams, would be 2 USD [202]. The cost of two microbridge copper wires, 5 centimeters each, would be also about 1 cent. Thereby, the microfluidic sensor itself is made of low-cost materials that also does not require complex fabrication steps and could be fabricated easily. Timewise, it will take 1 hour to make a device so labor cost is a major consideration which can be reduced per device by parallelization of manufacturing process to break the cost. Moreover, the current equipment used for electrical measurement and operation, such as sourcemeter and syringe pump, are not low-cost and appropriate low-cost alternatives should be used when integrating the sensor into a handheld platform in the future.

4.2 Bacteria detection

In this section, the findings of the microfluidic device being modified for bacteria detection will be presented. First, optimization of the antibody immobilization on the gold-coated wires will be reviewed. Then, the electrical detection of bacteria concentrations will be discussed. Next, the success of conjugation of the GNPs to the antibodies will be investigated. Lastly, our results on photothermal detection will be reported.

4.2.1 Antibody Immobilization: Characterization and Optimization

As discussed in the materials and methods section, the characterization of two immobilization techniques of direct and covalent bonding was investigated in several conditions to obtain the optimum methodology. The employed *E. coli* K12 had red fluorescent expressing tags that enabled probing successful or failed immobilization of the antibodies and successfully binding bacteria to the Ab-coated wires.

4.2.1.1 Direct Immobilization

To investigate the feasibility and efficiency of the direct immobilization, four wires (test) were functionalized with antibodies diluted in buffers with pH values of 5, 7, 8, and 9. Four other wires

(control) were treated with BSA 1% (w/v) diluted in identical buffers with varying pH levels. The wires were then incubated with *E. coli* bacteria buffer of 10^7 CFU/mL at 37°C. The bacteria had a red fluorescent expressing tag. Figure 4-15a-d shows the bacteria-incubated test and control wires after being treated with antibody and BSA solutions of pH 5, 7, 8, and 9, respectively. Each tested wire compared to its control wire was captured in the same image. After a qualitative assessment of the fluorescent images and comparison of test wires to their corresponding control wires, we concluded that the immobilization efficiency decreased as the pH increased, and the highest immobilization efficiency and uniformity were observed at pH 5. However, the control wires showed a red fluorescent signal due to the bacteria, though they were not functionalized with antibodies. This result indicates that the direct immobilization technique was not specific, and also not due to the presence of antibodies, as non-specific binding was observed, which was also reported previously [203].

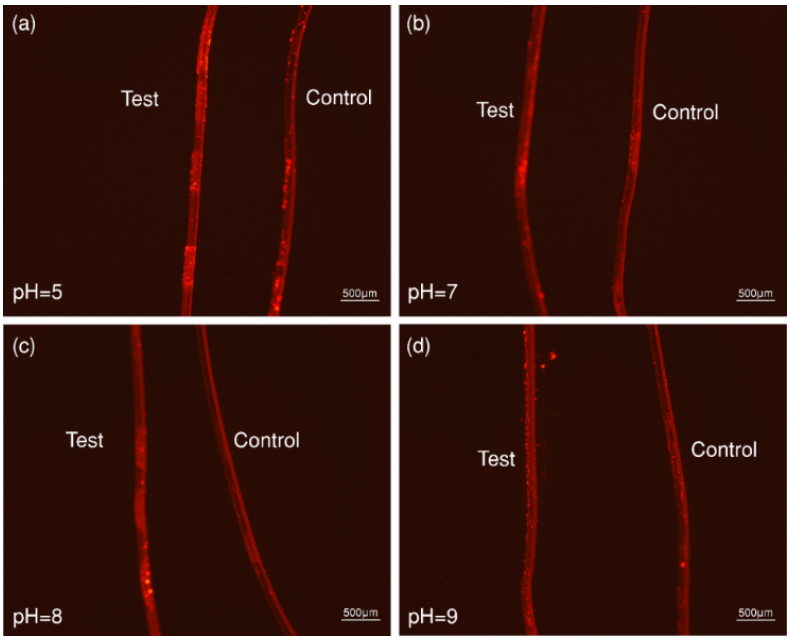

Figure 4-15. Bacteria capturing on wires using the direct antibody immobilization technique. Obtained fluorescent images in the red region were used to investigate the efficiency of the direct immobilization technique while the test wires were treated with antibodies and control wires were treated with BSA in

buffers of (a) pH 5, (b) pH 7, (c) pH 8, and (d) pH 9. Non-specific binding is observed within all pH values.

To minimize the non-specific binding, we added Tween 20 surfactant with a concentration of 0.05% (v/v) to both interaction (bacteria carrier) and washing buffers [204]. As depicted in Figure 4-16, the non-specific binding was reduced in the case of pH 5, 8, and 9, but it was worsened in the case of pH 7. In addition, the overall binding was exacerbated at pH 8 and 9 but was maintained at pH 5. However, in the case of wires treated with pH 5, the immobilization throughout the wires was not uniform, and patches of immobilized and non-immobilized sections were observed (See Figure 4-15a and Figure 4-16a). Thereby, as the direct immobilization technique did not show repeatability and robustness, it was not pursued further for experimentations.

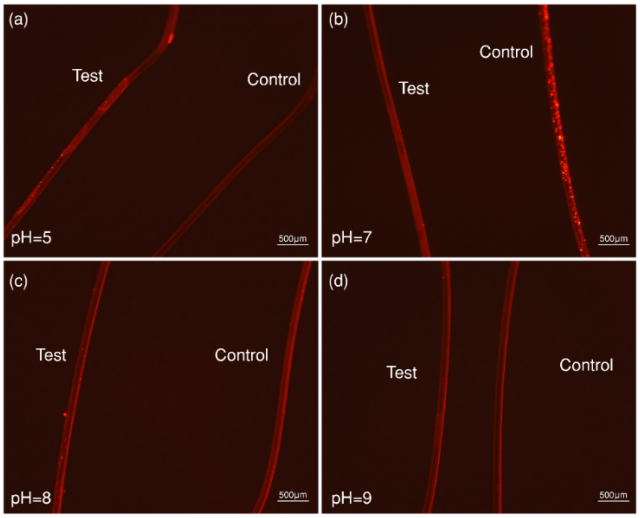

Figure 4-16. Fluorescent images in the red region were obtained to assess the efficiency of direct immobilization performed with test wires treated with antibodies and control wires treated with BSA in buffers of (a) pH 5, (b) pH 7, (c) pH 8, and (d) pH 9 with the addition of Tween 20 with a concentration of 0.05% (v/v). Non-specific binding is observed within all pH values.

4.2.1.2 Covalent Immobilization

Chemical cross-linkers were explored to immobilize antibodies through covalent binding to the gold-coated wires. The gold surface was first treated with lipoic acid to make it carboxylated to

react with the amino groups of the antibodies. To investigate the optimum concentration of lipoic acid for carboxylation, we selected four concentrations of 1, 5, 10, and 20 mM. The rest of the procedure was performed as explained in the materials and methods section. The control wires were exposed to BSA solutions for further comparison with antibody functionalized wires. Each tested wire compared to its control wire was captured in the same image. As in Figure 4-17, the immobilization uniformity and binding are improved compared to the direct method. A qualitative comparison of tested wires with their controls showed that the 5 mM and 10 mM lipoic acid concentrations had better uniformity but did not allow for choosing the optimal option.

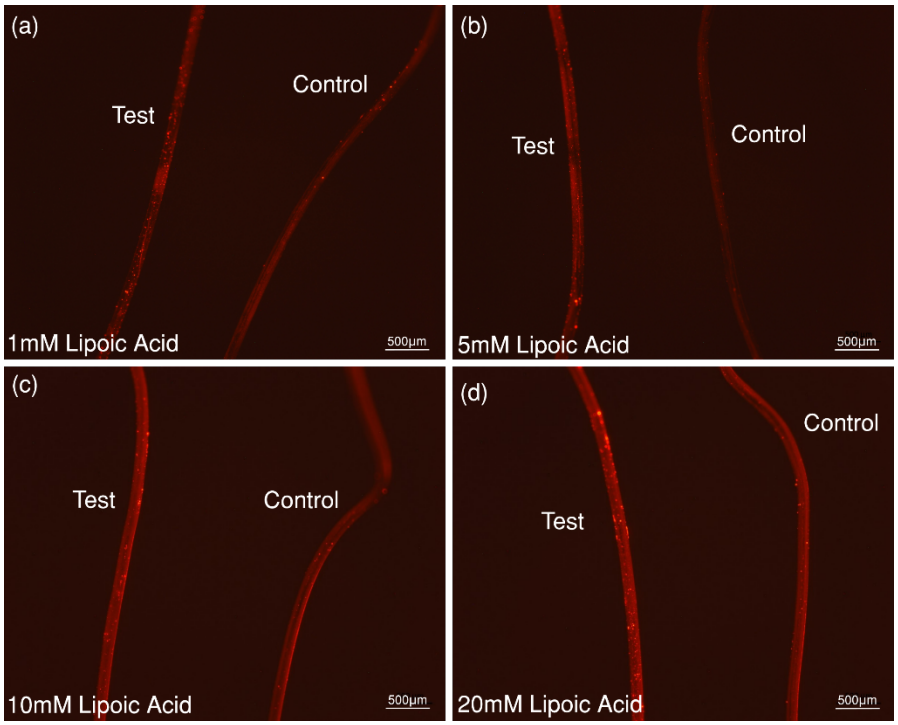

Figure 4-17. Fluorescent images in the red region were obtained to assess the efficiency of covalent immobilization performed with test wires treated with antibodies and control wires treated with BSA in lipoic acid with concentrations of (a) 1mM, (b) 5mM, (c) 10mM, and (d) 20mM.

To choose the most efficient concentration of lipoic acid, we analyzed red colour histograms of test and control wires in each concentration, as illustrated for 5mM lipoic acid in Figure 4-18. The

test and control wire average intensities were calculated and divided to obtain the intensity ratio (4-5).

$$\text{Intensity ratio} = \frac{\text{Average red color intensity in test wire}}{\text{Average red color intensity in control wire}} \quad (4\text{-}5)$$

The intensity ratio was then used to compare the efficiency of immobilization among the four concentrations of lipoic acid. As in Figure 4-18c, the intensity ratio at 5mM lipoic acid was higher than the other three concentrations and thus was picked for further experimentation.

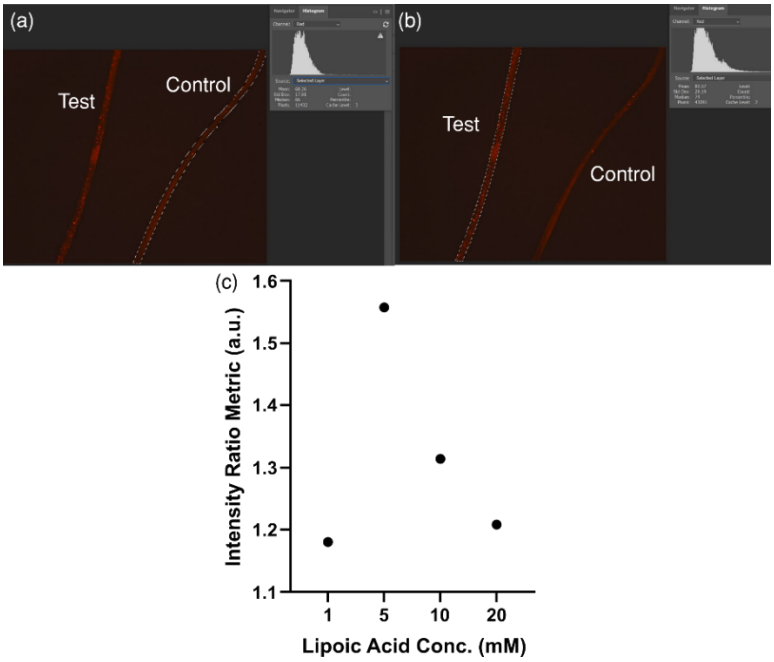

Figure 4-18. Determination of efficient lipoic acid concentration based on histograms of fluorescent images comparing test and control wires. (a) A sample test wire red colour histogram is obtained. (b) A sample control wire red colour histogram is obtained. (c) Determining the most efficient lipoic acid concentration for covalent immobilization was performed by calculating the average red colour intensity of the test and control wires and obtaining the intensity ratio by dividing them.

4.2.2 Electrical Bacteria Detection

As previously mentioned, for the case of bacteria detection, the interface resistances ($R_{int.}$) in Figure 3-1 are more critical as they are affected by the immobilized bacteria and, thereby, $R_{int.}$

should be maximized and the solution resistances ($R_{sol.}$) must be minimized. Therefore, the primary design configuration of the sensor described in section 3.1 was employed for bacteria contamination detection with 10^5, 10^6, and 10^7 CFU/mL bacterial counts. First, we measured the baseline resistance, defined as the resistance of the carrier solution without any bacteria between the wires in the microfluidic channel while maintaining the fluid flow (Figure 4-19a, d, g and j). Next, a bacteria solution was inserted into the channel, and the device was incubated for an hour at 37°C. After incubation, the channel was washed extensively with the same carrier solution to remove the uncaptured bacteria. Lastly, the resistance was measured with captured bacteria on the surface of the wires while the fluid flow of the carrier solution was maintained (Figure 4-19b, e, h and k). It was established that the signals reach a plateau after 60 seconds, and thus the recorded signals during the 60-100 seconds were used to calculate the mean resistance values. The averaged resistances were then compared to the baseline in Figure 4-19c, f, i and l. It was established that the sensor could not detect bacteria counts of 10^5 CFU/mL as there was no difference observed between the averaged data of the baseline and bacteria captured on the wires. Thereby, the 10^5 CFU/mL was disregarded in the further experimentations.

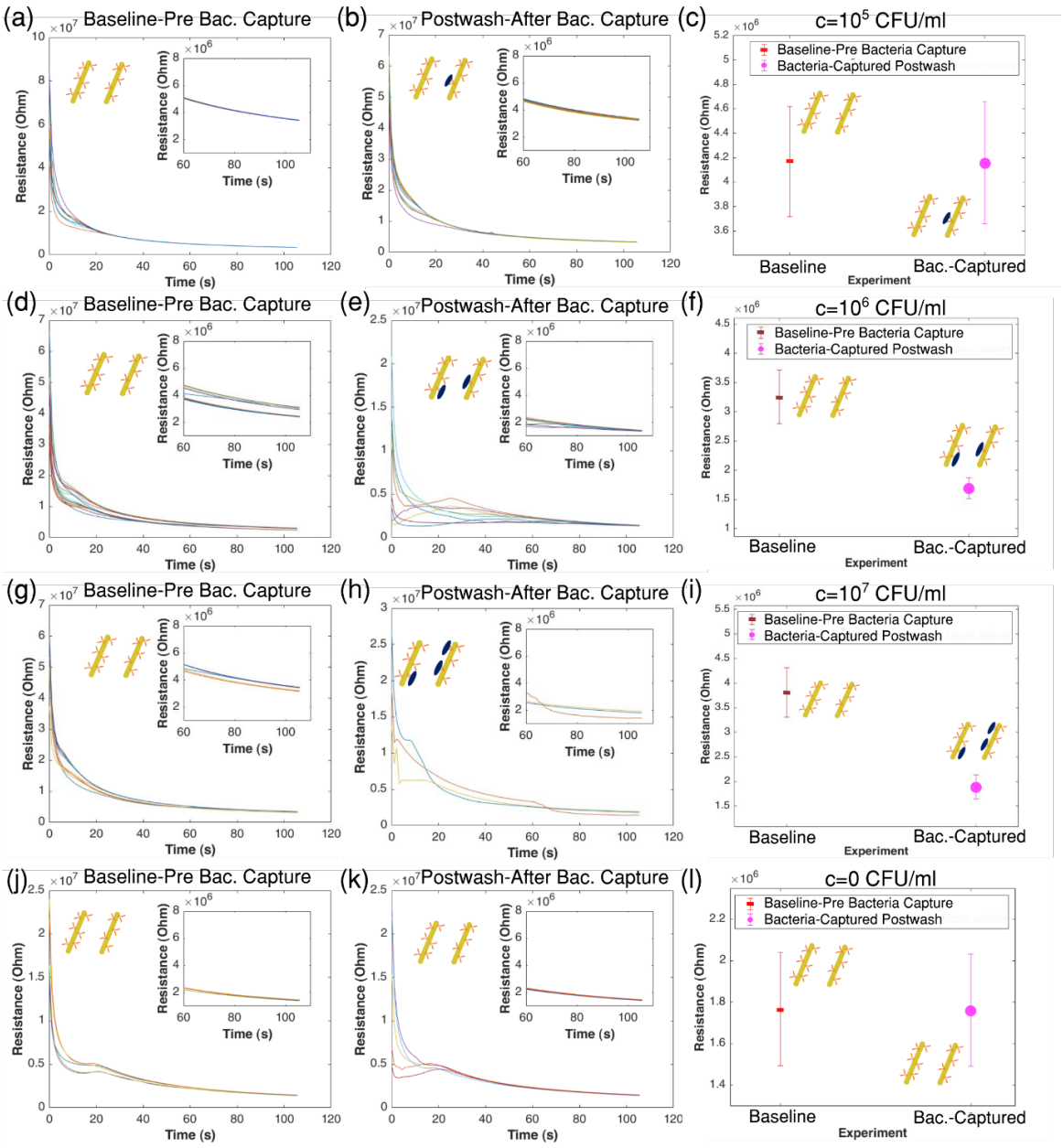

Figure 4-19. Electrical sensing of immunologically captured bacteria on the wires of the microfluidic sensor. Resistances were measured for blank buffer prior to bacteria sample incubation (left column) and after post-incubation wash (middle column). The average resistances are also reported (right column) for (a-c) 10^5 CFU/mL , (d-f) 10^6 CFU/mL, (g-i) 10^7 CFU/mL, and (j-l) negative control with no bacterial incubation.

Each bacteria count was replicated three times with at least three repetition measurements. The raw resistances in Figure 4-19 were normalized to the corresponding device's measured baseline

to eliminate inter-device variabilities, as depicted in Figure 4-20. Figure 4-20a illustrates each replicate's normalized resistances, enabling comparisons between different replicates of counts. It was established that the lowest resistances recorded from a replicate tested with 10^6 CFU/mL were statistically different from the highest recorded signal from a replicate of negative control (NC, with no bacterial incubation). Similarly, the lowest recorded resistance from a replicate exposed to 10^7 CFU/mL was statistically different from the highest signal recorded from a 10^6 CFU/mL replicate. It was then obtained that the recorded signals for replicates of one count are distinct compared to replicates of another count.

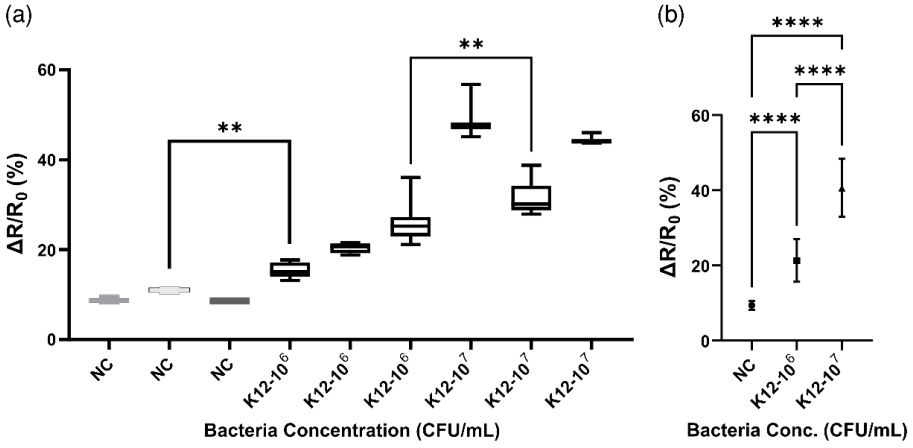

Figure 4-20. Normalized dose-response measurements of the bacteria microfluidic sensor. (a) Replicates of every tested bacterial count are shown. (b) The two tested counts of 10^6 and 10^7 CFU/mL are significantly different from each other and the baseline.

Figure 4-20b compares the three experimented bacterial counts, considering all replicates and repetitions. It was observed that there is a statistically significant difference between negative control, 10^6 CFU/mL, and 10^7 CFU/mL counts.

4.2.3 Photothermal Bacteria Detection

This section will first discuss the verification of GNP conjugation to antibodies, as the tags used for photothermal detection of bacteria. Then, the results of the photothermal detection of bacteria captured on the gold-coated wires will be presented.

4.2.3.1 GNP-Antibody Conjugation

To investigate whether the conjugation of synthesized GNPs to the secondary antibodies was successful or not, we performed two experiments using monoclonal and polyclonal antibodies. The first experiment involved adding a saline solution to the gold nanoparticle samples, as depicted in Figure 4-21a. The addition of saline solution to samples of GNP that are not covered with antibodies would result in the aggregation of GNPs that change their colour from red to violet. Whereas GNPs treated with antibodies did not experience a significant change in their colour. It was established that the GNPs conjugated with polyclonal antibodies (GNP-pAb) were more stable than the monoclonal antibodies (GNP-mAb) due to their superior colour preservation after treatment with saline solution. Thereby, GNP-pAb functionalization was used for the photothermal experiments.

The second experiment for conjugation verification of GNPs with pAb was performed through UV-vis measurement, as shown in Figure 4-21b. The observed peak was blue shifted from 520nm to 529nm, showing an interaction between the GNPs and antibodies. Similar confirmations were reported previously [205]. Following the observations in the UV-vis measurements, a 520nm laser was used in the compact optical setup, shown in Figure 3-7, to achieve the highest absorbance of light by the GNPs.

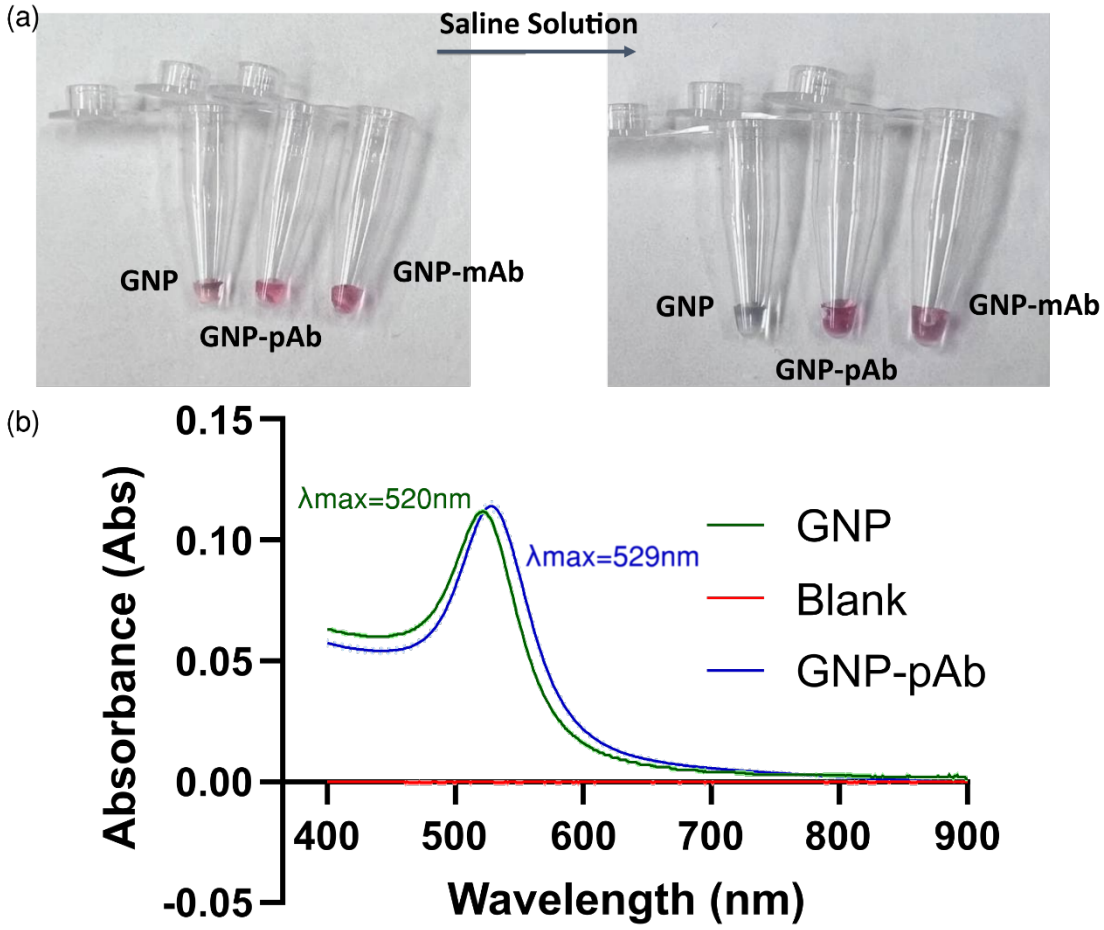

Figure 4-21. Investigation of GNP conjugation to antibodies. (a) Saline solution addition to samples of GNP, GNP-mAb, and GNP-pAb. GNPs not treated with Ab would aggregate and change colour from red to violet. (b) UV-vis measurement and comparison of GNP and GNP-pAb solutions show that the peak blueshifted from 520nm to 529nm, confirming antibody-GNP interactions.

4.2.3.2 Lock in Thermography (LIT) Analysis of Datasets

As mentioned in the materials and methods section, the amplitude and phase of thermal waves may be directly computed by applying the fast Fourier transform (FFT) to the time-lapse data from each infrared camera pixel. Figure 4-22 demonstrates how this process is performed for a wire with a high signal. Figure 4-22a shows the amplitude image on which GNPs were dried to have a strong signal. To better explain the signal processing carried out on datasets, here we explain the processing done on signal of one pixel in the image (i.e., pixel showed by crosshair in Fig, 4-22a).

The recorded time lapse signal for the selected pixel is plotted in Figure 4-22b. As expected, the infrared radiation registered is modulated at the modulation frequency of laser excitation. It can also be seen that the baseline (aka DC offset) of signal increases over time due to bulk heating of the wire by laser. To remove the DC offset from the signal, a 7-degree polynomial was fit to the data and subsequently subtracted. The outcome of this processing is depicted in Figure 4-22c. Lastly, FFT is applied to the signal to establish the amplitude against the frequency, shown in Figure 4-22d. The resulting amplitude peak at 1 Hz (i.e., laser modulation frequency) can be established as the amplitude value for the selected pixel. By applying similar signal processing to all pixels, an amplitude image can be formed.

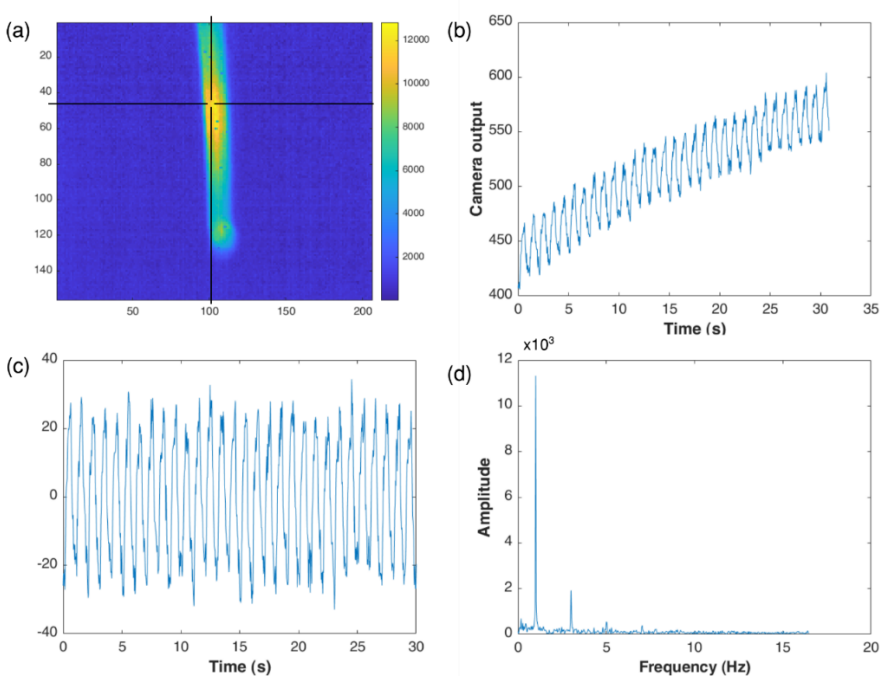

Figure 4-22. Process of computing amplitude from recorded frames for each pixel. (a) one pixel is selected for analysis. (b) The recorded signals for the selected pixel are plotted against time. (c) DC offset was removed. (d) FFT was applied to plot amplitude against the frequency. The amplitude value at the modulation frequency (1Hz) is established for the selected pixel.

4.2.3.3 Fluorescent Image Results

To study the compact sensor's bacteria detection capability, wires with bacteria counts of 0, 10, 10^2, 10^3, 10^5, 10^6, and 10^7 CFU/mL were prepared and tagged with GNPs. (Figure 4-23). As the applied bacteria have red expressing fluorescent tags, we can observe and confirm the successful capturing of bacteria. As anticipated, the fluorescent activity of the wires increased when the bacteria count increased, verifying the bacteria count difference on the tested wires. However, qualitative assessment of the 10, 10^2, and 10^3 CFU/mL wires did not show significant changes, whereas a visual difference could be noticed in higher bacteria counts.

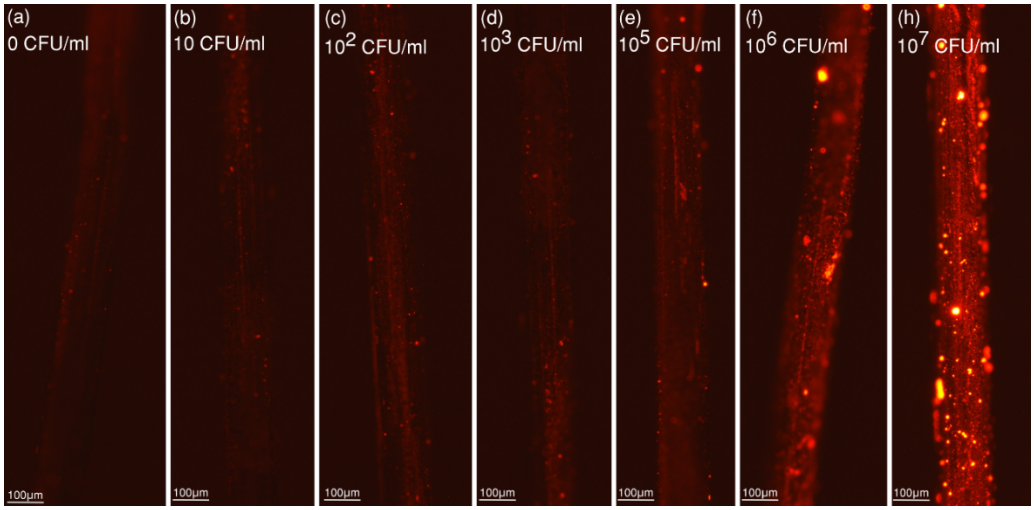

Figure 4-23. Fluorescent images in the red region were obtained from wires treated with (a) 0, (b)10, (c) 10^2, (d) 10^3, (e) 10^5, (f) 10^6, and (h) 10^7 CFU/mL of E. coli bacteria.

4.2.3.4 Photothermal Detection Results

The photothermal measurements were carried out three times for the prepared wires. Using our established signal analysis method, histograms of the amplitude values within the vicinity of the wires were plotted, and data was filtered to remove the background noise. Then, the data were averaged and correlated to the bacteria count (See 3.2.3.2). The averaged data from the wires were plotted in Figure 4-24a. Our pair-wise post-hoc analysis demonstrated that the differences between

the obtained amplitude values for each bacteria count are not statistically significant. However, our lowest bacteria count of 10 CFU/mL was significantly different from the negative control wire that established 10 CFU/mL LOD. We did not detect different PT signals in 10-10^3 range which is also consistent with fluorescent images of Figure 4-23, which might be due to the chemistry/immobilization or the fact that our fluorescent imaging and photothermal methods were not sensitive to the changes in concentration. Besides, the signals showed an increasing trend following the increase in the bacteria count. To further analyze the data, we divided the bacteria counts into two main groups of lower and higher bacteria counts with 10-10^3 and 10^5-10^7 CFU/mL, respectively. The statistical analysis showed a significant difference between the lower and higher bacteria groups (p=0.0011). The lower and higher bacteria groups were also different than the negative control wire (Figure 4-24a).

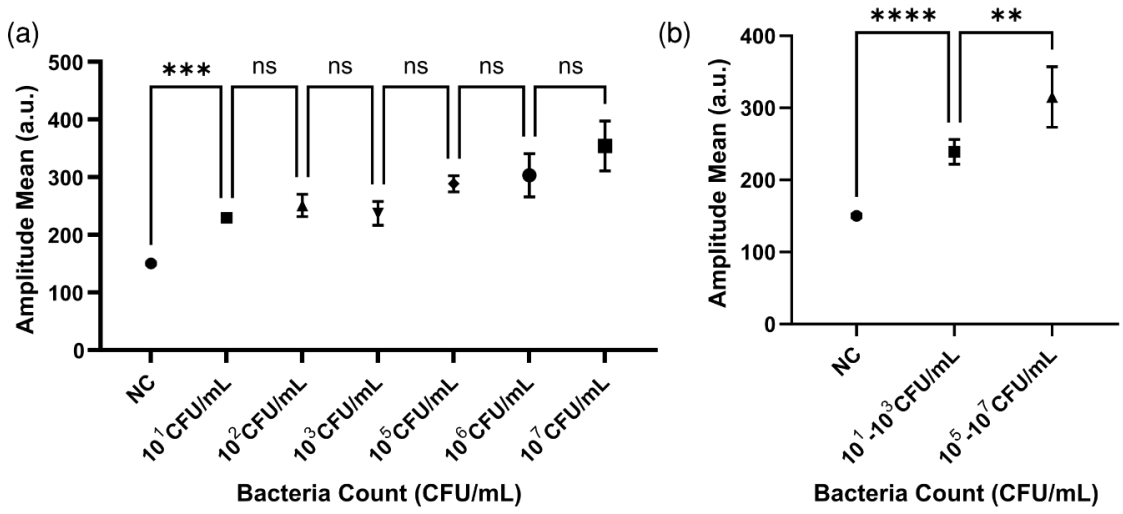

Figure 4-24. Photothermal detection results of wires treated with bacteria count 10-10^7 CFU/mL. (a) A LOD of 10 CFU/mL was established, though there was no significant difference between bacteria count pairs. (b) The lower bacteria count (10-10^3 CFU/mL) and higher bacteria count (10^5-10^7 CFU/mL) groups showed significant difference (p=0.0011).

4.2.3.5 Inter-variability Assessment

To examine data repeatability and reproducibility, three wire replicates for each bacterium count in the range of 10^2-10^7 CFU/mL were prepared. Photothermal measurements and data analysis were carried out on all replicates. For each replicate, three measurements were carried out. Figure 4-25 illustrates amplitude images of the bacteria-treated and GNP-tagged wires. No significant signal was recorded from the negative control wires as in Figure 4-25a. In contrast, the amplitude values for the bacteria-treated wires were all distinguishable from the background. The wires treated with dried GNPs expressed the highest amplitude values shown in Figure 4-25g, as expected.

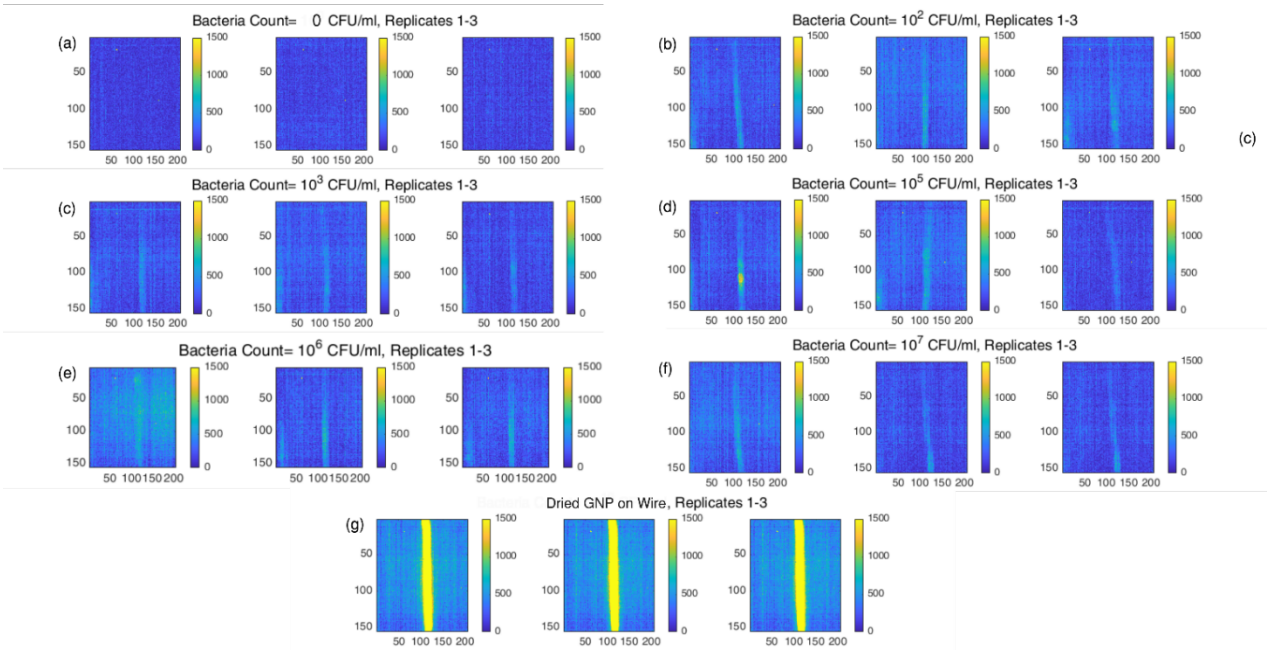

Figure 4-25. Amplitude images of wires with bacteria captured and GNPs tagged. The bacteria count is (a) 0, (b) 10^2, (c) 10^3, (d) 10^5, (e) 10^6, and (f) 10^7 CFU/mL. (g) GNPs were dried on the wire to establish the highest possible signal from the GNP batch concentration. Three replicate wires were produced for each bacteria count, and each wire measurement was repeated three times.

A histogram of the amplitude data for each replicate is plotted in Figure 4-26, demonstrating the filtration process by discarding the data to the left side of the drawn red vertical line for each

replicate. The results of the replicate are summarized and plotted in Figure 4-27a. It was established that there was no statistically significant difference between three wire replicates that were treated with the same bacteria counts ($p>0.2$). This observation suggests that the sensor had an acceptable inter-variability and replicate-to-replicate reproducibility. Figure 4-27b shows the averaged data values from all replicates and repetitions for each bacteria count. Again, there is no statistically significant difference between each neighboring pair of the bacteria counts. However, we observed significant difference ($p<0.01$) among higher and lower bacteria groups with bacteria concentrations of 10^5-10^7 CFU/mL and 10^2-10^3 CFU/mL, as in Figure 4-27c.

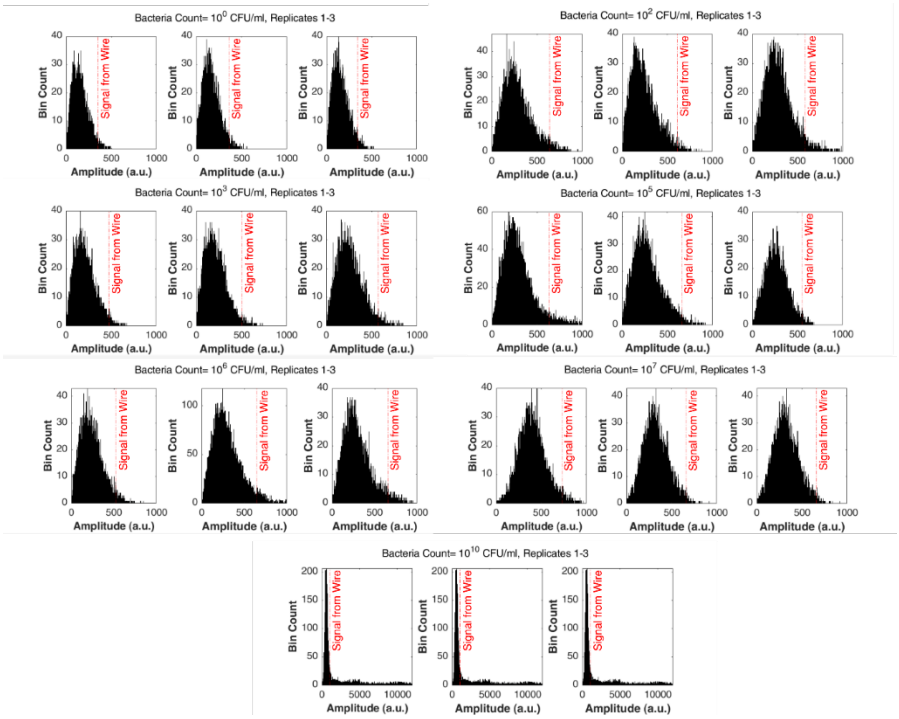

Figure 4-26. Histograms of the amplitude images are plotted for (a) 0, (b) 10^2, (c) 10^3, (d) 10^5, (e) 10^6, (f) 10^7 CFU/mL, and (g) dried GNP on wire. The full width at half maximum (FWHM) is depicted with two red dots on each sub-panel.

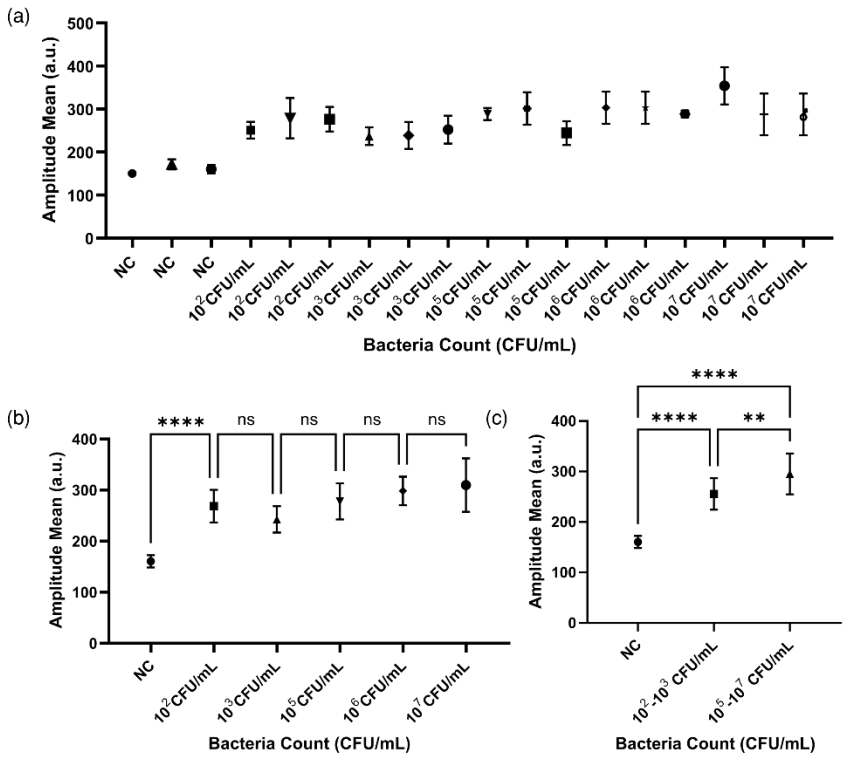

Figure 4-27. Intervariability assesment of the phothermal detection. Three wire replicates with the same bacteria counts are prepared in the range of 10^2-10^7 CFU/mL. (a) Photothermal detection and data analysis demonstrated that the sensor had inter-variability and replicate-to-replicate reproducibility ($p>0.2$). (b)The averaged data values from all replicates and repetitions are shown.

4.2.3.6 Photothermal Biosensor Selectivity

To investigate the compact biosensor's selectivity toward the target analytes, we performed a specificity test using three non-specific and two specific bacteria. As our antibodies are specific only toward *E. coli* bacteria with O and K strains, we anticipated to have photothermal signals from bacteria with these strains only. *Lysteria innocua*, *Salmonella pullorum*, and *E. coli DH5α* were used as our non-specific targets whereas *E. coli OP50* and *E. coli K12* were employed as our specific analytes. Three replicate wires were prepared and exposed to each of these bacterium strains with 10^7 CFU/mL and then similar previous preparation and detection procedure were followed. As in Figure 4 28, it was established that the amplitude signals of the non-specific

bacterium types were significantly different than the specific strains ($p<0.0001$). It was also evident that the specific bacteria were successfully captured and sandwiched by the GNPs on the wires that produced the enhanced detection signals.

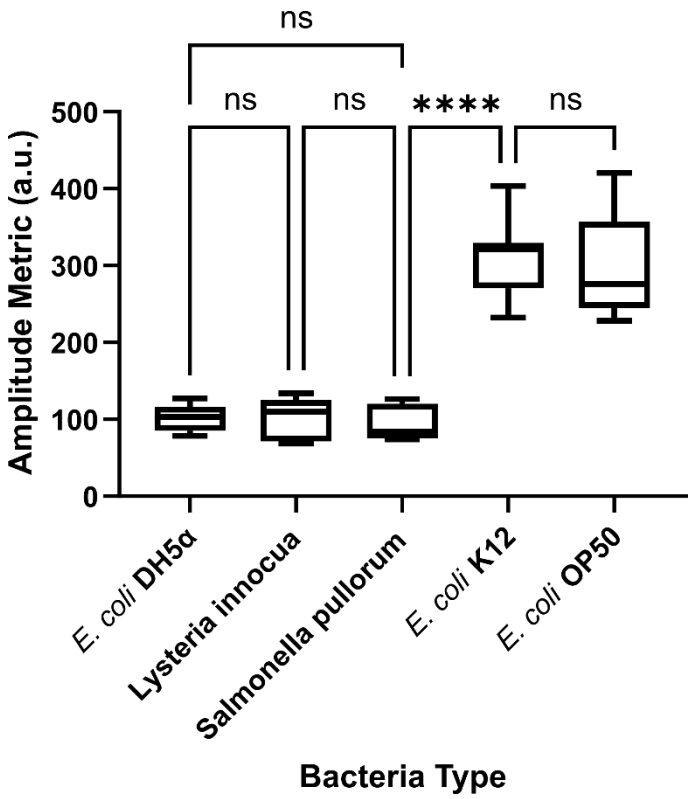

*Figure 4-28. Selectivity assessment of the photothermal detection. Photothermal amplitude signals from three non-specific bacteria strains (Lysteria innocua, Salmonella pullorum, and E. coli DH5α) were compared to two specific bacterium types (E. coli OP50 and E. coli K12). Three replicate wires were considered for each bacterium type and the wires were exposed to 10^7 CFU/mL of the bacteria. The averaged data values from all replicates and repetitions are shown. ****: $p<0.0001$*

4.2.4 Conclusion on the Bacteria Sensor

The bacteria detection sensor showed promising possibilities in detecting the bacteria samples in both electrical and photothermal techniques. The microfluidic sensor demonstrated an electrical detection and quantification of bacteria samples with *E. coli* K12 counts of 10^6 CFU/mL and 10^7 CFU/mL in 1 hour. The sensor can operate with small sample volumes (500µL) and measure in

100 seconds following the bacteria sample incubation (1 hour) and washing steps (5 mins). The detection chamber was also contained in the electrical detection, and the operators would not be in close contact with the bacteria samples.

For the case of photothermal detection, a handheld detection platform was developed that demonstrated a low LOD of 10 CFU/mL. Bacteria in the range of 10-10^7CFU/mL were detected and were found to be significantly different than the negative control wire. It was established that the platform could distinguish wires treated with high bacteria counts (10^5-10^7 CFU/mL) from lower bacteria counts (10-10^3 CFU/mL).

The next chapter will provide further suggestions to improve the sensor's capabilities like sensitivity and LOD.

Chapter 5: Conclusion and Recommendations for Future Works

This section summarizes the thesis, followed by recommendations for future research.

5.1 Thesis Summary

We have designed and developed a low-cost PDMS-based microfluidic platform for water contamination detection. The detection device consisted of a microfluidic channel with two wires in the middle. The wires were used as probing electrodes, and the conductivity of the sample between the electrodes was measured and correlated to sample concentration. As two critical contaminators, the detection of NaCl and bacteria in water were picked to investigate the sensor's performance.

For the case of NaCl detection, the primary device was used to detect and quantify samples with low salt levels of 0-20 ppm, which is more relevant to drinking water salt spans than previously developed sensors that primarily work in seawater ranges. The sensor worked in less than 1 minute, and detection sensitivity, the limit of detection (LOD), and quantification (LOQ) of 17.1 Ohm/Ohm.cm, 0.31 ppm, and 0.37 ppm, respectively. Next, a numerical model was developed based on the primary design and was verified and validated against experimental findings. Then, a numerical optimization through parametric analysis was carried out to obtain an efficient geometrical and physical parameter configuration. After establishing the optimized design, the salt detection was repeated, and an extended detection range of 1-120 ppm was achieved. The optimized sensor also produced the results in less than 1 minute but with an improved detection sensitivity, LOD and LOQ of 385 Ohm/Ohm.cm, 0.39 and 0.44 ppm, respectively.

The optimized NaCl sensor demonstrated promising potential in differentiating the samples with NaCl concentrations in the range of 1-120 ppm. The sensor exhibited a LOD of 0.39 ppm, lower than the NaCl detectors reported before. Although previously developed optical salinity sensors have reported lowest detected values of 2 ppm [38], [60] 4 ppm[37], 6.7 ppm [55], 10 ppm [61], and 40 ppm [62] they lack the required resolution to quantify salt within drinking water ranges. This limitation occurs because a 1,000 ppm change in salinity normally causes an infinitesimal deviation in the optical pathlength [33]. In addition, these sensors were complex, laboratory-based, and costly due to their reliance on prisms or delicate fiber optics but were able to detect non-ionic salts as well. Reported conductivity-based sensors offered lowest detected values of 12 ppm [206], 16 ppm [207], 165 ppm [112], and even higher (e.g. 7,800 ppm) [208]–[210] which are not suitable for sensitive detection in the drinking water applications. Also, these sensors involved labor-intensive and expensive fabrication procedures. In comparison, the proposed optimized sensor was fabricated with a simple and low-cost technique which allows for sensing in drinking water ranges on a miniaturized and inexpensive platform.

The experimental evidence showed the sensor's accuracy and repeatability, making it a promising candidate for different applications such as surveillance of consumed water by individuals with salt-restricted diets.

Following the promising performance of the sensor in detecting water salinity, the sensor was modified for bacteria detection. The copper wires in the salinity detection were replaced with gold-coated copper wires that are more suitable for anti-*E. coli* antibody immobilization. Antibodies were used as bioreceptors to capture the target antigen from the bacteria sample. After characterization of successful antibody immobilization and bacteria capturing, the detection was performed by electrical and photothermal techniques. The electrical detection was carried out

inside the microfluidic channel, and quantification of bacteria samples with 10^6 CFU/mL and 10^7 CFU/mL with statistically significant differences.

The feasibility of detecting bacteria from photothermal responses was studied to enhance the detection performance further. The photothermal detection was performed off-chip and on a compact platform that could be used on site. GNPs, covered with anti-*E. coli* antibodies were used to sandwich the bacteria on the wires. The GNPs were irradiated with modulating laser light, resulting in their excitation and radiation of infrared radiation. An IR camera collected these radiations, and the signals' amplitude was calculated and analyzed for detection. The sensor demonstrated the detection of bacteria in the range of 10-10^7 CFU/mL with a LOD of 10 CFU/mL. The detection duration was approximately 1 hour and 20 minutes.

This work has shown great potential to make significant contributions to environmental water monitoring by offering a low-cost, swift, and reliable solution for contamination detection.

5.2 Limitations and Recommendations for Future Research

In this thesis, we used the microfluidic device to detect NaCl and bacteria as two contaminations of water with repeatability and accuracy. However, certain drawbacks will be discussed for each application below with suggested resolutions.

The current design of the developed microfluidic salinity sensor suffers from three main limitations. First, salt detection is performed by measuring conductivity so that non-specific ionic entities in the sample can interfere. As such, the detection of the current version of the sensor is not selective/specific. To resolve this issue, sample filtration prior to detection or specific receptors to the target analyte is recommended. Although the proposed device does not specifically detect sodium chloride, it could be used as a preliminary surveillance system to warn the water consumers

or inspection officials to perform further tests on water safety. Second, the discussed characterizations of the sensors were performed in ambient temperature, and pressure and the established calibration curves are only accurate in these conditions. This issue could be resolved by repeating the experiments in different temperature and pressure conditions and establishing the calibration curves. Third, the present sensors rely on a syringe pump and source meter that impedes in-situ measurement that could be solved by replacing the DC source-meter with portable alternatives and the syringe pump with a passive on-chip or a battery-operated peristaltic pump.

For the case of bacteria detection by measuring the conductivity, the limit of detection was 10^6 CFU/mL, which is higher than similar other biosensors. Several modifications could remove this limitation to the device. First, the sensor's electrodes could be changed to interdigitated electrodes with a higher detection area toward a higher surface-to-volume ratio in the detection chamber. Second, signal amplification can help achieve lower detection limits by using on-chip sample bacteria amplification methods like PCR or the Wheatstone bridge. In addition, migrating from DC signal acquisition to AC might need additional equipment but would allow measuring resistance and capacitance that could help lower the LOD. Similarly, shifting to electrochemical detection in a three-electrode paradigm and maintaining specific enzyme reactions that contribute to the measured electrical signal could improve the sensor's functionality. Further numerical and experimental parametric studies to optimize the sensor's geometrical characteristics could be insightful in this regard as well.

The photothermal detection of bacteria samples on the wires also showed promising potential in detection on a handheld platform for in-situ applications. There existed a limitation that included the operator's safety. Close contact of the operator with the wire could pose health hazards in the case of pathogenic bacteria detection. The detection procedure must be further modified to

maintain the operator's safety without compromising the detection limit or portability of the platform. On the other hand, our pairwise post-hoc analysis showed that the sensor resolution is approximately 10^3 CFU/mL, which shows low sensor sensitivity. Several steps can be taken to improve sensor sensitivity in future works. First, the concentration of GNPs and the type and concentration of secondary antibodies could be optimized. Second, the detection platform could be widened to increase the surface-to-volume ratio of the device to increase the signal acquisition and potentially increase the sensitivity. Third, the immobilization of primary antibodies on the gold-coated wires could be further optimized in a parametric study for parameters such as incubation temperature and duration, and antibody concentration. Following the suggestions above, the proposed low-cost detection platform could be applied for low-cost, swift, and accurate detection in a point-of-care paradigm.

References

[1] M. Elimelech, "The global challenge for adequate and safe water," *J. Water Supply Res. Technol.*, vol. 55, no. 1, pp. 3–10, 2006.

[2] S. Sharma and A. Bhattacharya, "Drinking water contamination and treatment techniques," *Appl. Water Sci.*, vol. 7, no. 3, pp. 1043–1067, 2017.

[3] S. A. Jaywant and K. Mahmood Arif, "A comprehensive review of micro fluidic water quality monitoring sensors," *Sensors (Switzerland)*. 2019, doi: 10.3390/s19214781.

[4] J. Fawell and M. Nieuwenhuijsen, "Contaminants in drinking waterEnvironmental pollution and health," *J Br. Med. Bull.*, vol. 68, no. 1, pp. 199–208, 2003.

[5] R. L. Calderon, "The epidemiology of chemical contaminants of drinking water," *Food Chem. Toxicol.*, vol. 38, pp. S13–S20, 2000.

[6] "Guidelines for drinking-water quality, Fourth Edition," 2011.

[7] J. Ma, F. Meng, Y. Zhou, Y. Wang, and P. Shi, "Distributed water pollution source localization with mobile UV-visible spectrometer probes in wireless sensor networks," *Sensors*, vol. 18, no. 2, p. 606, 2018.

[8] G. Mills and G. Fones, "A review of in situ methods and sensors for monitoring the marine environment," *Sensor Review*. 2012, doi: 10.1108/02602281211197116.

[9] C. Canhoto, S. Simões, A. L. Gonçalves, L. Guilhermino, and F. %J S. of the T. E. Bärlocher, "Stream salinization and fungal-mediated leaf decomposition: a microcosm study," vol. 599, pp. 1638–1645, 2017.

[10] W. Xu *et al.*, "All-fiber seawater salinity sensor based on fiber laser intracavity loss modulation with low detection limit," *Opt. Express*, 2019, doi: 10.1364/oe.27.001529.

[11] E. Samiei, M. Tabrizian, and M. Hoorfar, "A review of digital microfluidics as portable platforms for lab-on a-chip applications," *Lab Chip*, vol. 16, no. 13, pp. 2376–2396, 2016.

[12] H. Vaisocherová-Lísalová *et al.*, "Low-fouling surface plasmon resonance biosensor for multi-step detection of foodborne bacterial pathogens in complex food samples," *Biosens. Bioelectron.*, 2016, doi: 10.1016/j.bios.2016.01.040.

[13] G. M. Whitesides, "The origins and the future of microfluidics," *Nature*. 2006, doi: 10.1038/nature05058.

[14] S. W. Dutse and N. A. Yusof, "Microfluidics-based lab-on-chip systems in DNA-based biosensing: An overview," *Sensors*, 2011, doi: 10.3390/s110605754.

[15] F. A. N. Yi-Qiang, W. Hong-Liang, G. A. O. Ke-Xin, L. I. U. Jing-Ji, C. Dong-Ping, and Y.-J. ZHANG, "Applications of Modular Microfluidics Technology," *Chinese J. Anal.*

Chem., vol. 46, no. 12, pp. 1863–1871, 2018.

[16] L. Wang and A. Mustapha, "Ema-real-time pcr as a reliable method for detection of viable salmonella in chicken and eggs," *J. Food Sci.*, 2010, doi: 10.1111/j.1750-3841.2010.01525.x.

[17] J. Wan, J. Ai, Y. Zhang, X. Geng, Q. Gao, and Z. Cheng, "Signal-off impedimetric immunosensor for the detection of Escherichia coli O157:H7," *Sci. Rep.*, 2016, doi: 10.1038/srep19806.

[18] P. M. Shaibani *et al.*, "Portable Nanofiber-Light Addressable Potentiometric Sensor for Rapid Escherichia coli Detection in Orange Juice," *ACS Sensors*, 2018, doi: 10.1021/acssensors.8b00063.

[19] G. A. R. Y. Suaifan, S. Alhogail, and M. Zourob, "Rapid and low-cost biosensor for the detection of Staphylococcus aureus," *Biosens. Bioelectron.*, 2017, doi: 10.1016/j.bios.2016.11.047.

[20] L. Wang *et al.*, "QCM-based aptamer selection and detection of Salmonella typhimurium," *Food Chem.*, 2017, doi: 10.1016/j.foodchem.2016.11.104.

[21] S. Leahy and Y. Lai, "A cantilever biosensor based on a gap method for detecting E. coli in real time," *Sensors Actuators, B Chem.*, 2017, doi: 10.1016/j.snb.2017.02.144.

[22] S. B. Patil, V. F. Annese, and D. R. S. Cumming, "Commercial aspects of biosensors for diagnostics and environmental monitoring," in *Advances in Nanosensors for Biological and Environmental Analysis*, Elsevier, 2019, pp. 133–142.

[23] M. J. McGrath and C. N. Scanaill, "Sensing and sensor fundamentals," in *Sensor technologies*, Springer, 2013, pp. 15–50.

[24] J. Fraden, "Sensor characteristics," in *Handbook of Modern Sensors*, Springer, 2010, pp. 13–52.

[25] G. Van Der Horn and J. Huijsing, *Integrated smart sensors: design and calibration*, vol. 419. Springer Science & Business Media, 1997.

[26] K. A. Charles and N. O. Matthew, *Fundamentals of electric circuits*. McGraw-hill Education, 2017.

[27] J. S. Wilson, *Sensor technology handbook*. Elsevier, 2004.

[28] C. K. Ho, A. Robinson, D. R. Miller, and M. J. %J S. Davis, "Overview of sensors and needs for environmental monitoring," vol. 5, no. 1, pp. 4–37, 2005.

[29] S.-Y. Lu, H.-M. Zhang, S. O. Sojinu, G.-H. Liu, J.-Q. Zhang, and H.-G. Ni, "Trace elements contamination and human health risk assessment in drinking water from Shenzhen, China," *Environ. Monit. Assess.*, vol. 187, no. 1, p. 4220, 2015.

[30] A. Jang, Z. Zou, K. K. Lee, C. H. Ahn, and P. L. Bishop, "State-of-the-art lab chip sensors for environmental water monitoring," *Meas. Sci. Technol.*, vol. 22, no. 3, p. 32001, 2011.

[31] M. G. Weller, "Immunoassays and biosensors for the detection of cyanobacterial toxins in

water," *Sensors*, vol. 13, no. 11, pp. 15085–15112, 2013.

[32] B. Nasseri, N. Soleimani, N. Rabiee, A. Kalbasi, M. Karimi, and M. R. Hamblin, "Point-of-care microfluidic devices for pathogen detection," *Biosens. Bioelectron.*, vol. 117, pp. 112–128, 2018, doi: https://doi.org/10.1016/j.bios.2018.05.050.

[33] Y. Qian, Y. Zhao, Q. lu Wu, and Y. Yang, "Review of salinity measurement technology based on optical fiber sensor," *Sensors and Actuators, B: Chemical*. 2018, doi: 10.1016/j.snb.2017.12.077.

[34] N. P. Majozi, M. S. Salama, S. Bernard, D. M. Harper, and M. G. Habte, "Remote sensing of euphotic depth in shallow tropical inland waters of Lake Naivasha using MERIS data," *Remote Sens. Environ.*, 2014, doi: 10.1016/j.rse.2014.03.025.

[35] F. Adamo, F. Attivissimo, and C. G. C. %J A. smart sensor network for sea water quality monitoring Carducci, "Lanzolla AMLJISJ 2014," vol. 15, pp. 2514–2522.

[36] G. Bœuf and P. Payan, "How should salinity influence fish growth?," 2001, doi: 10.1016/S1532-0456(01)00268-X.

[37] A. Nag, S. C. Mukhopadhyay, and J. Kosel, "Sensing system for salinity testing using laser-induced graphene sensors," *Sensors Actuators, A Phys.*, 2017, doi: 10.1016/j.sna.2017.08.008.

[38] J. M. Racicot, T. L. Mako, A. Olivelli, and M. Levine, "A paper-based device for ultrasensitive, colorimetric phosphate detection in seawater," *Sensors (Switzerland)*, 2020, doi: 10.3390/s20102766.

[39] P. Vineis, Q. Chan, and A. Khan, "Climate change impacts on water salinity and health," *Journal of Epidemiology and Global Health*. 2011, doi: 10.1016/j.jegh.2011.09.001.

[40] "Guidelines for Canadian Drinking Water Quality: Guideline Technical Document – Sodium," 1992.

[41] F. J. He and G. A. MacGregor, "A comprehensive review on salt and health and current experience of worldwide salt reduction programmes," *Journal of Human Hypertension*. 2009, doi: 10.1038/jhh.2008.144.

[42] A. D. Lopez, C. D. Mathers, M. Ezzati, D. T. Jamison, and C. J. Murray, "Global and regional burden of disease and risk factors, 2001: systematic analysis of population health data," *Lancet*, vol. 367, no. 9524, pp. 1747–1757, 2006.

[43] E. Schulze, "Guidelines for Drinking-Water Quality. Vol. 2. Health Criteria and Other Supporting Information. 335 Seiten. World Health Organization, Geneva 1984. Preis: 35.– Sw. fr.," *Food / Nahrung*, 1986, doi: 10.1002/food.19860300121.

[44] V. C. Armstrong, M. G. Holliday, and T. F. Schrecker, "Tap water consumption in Canada. Environmental Health Directorate Report 82-EHD-80," Ottawa, 1981.

[45] K. S. Subramanian and J. C. Meranger, "A survey for sodium, potassium, barium, arsenic and selenium in Canadian drinking water supplies," *At. Spectrosc.*, vol. 5, no. 1, pp. 34–35, 1984.

[46] R. G. Bond and C. P. Straub, *Genetic types of subterranean waters in relation to their salinity. In: Handbook of environmental control.*, 1st editio. Cleveland, OH: CRC Press, 1973.

[47] T. Co-ordinated by Water Quality Section, Laboratory Services Branch, "Outlines of analytical methods: a guide to the occurrence, significance, sampling and analysis of chemical and microbiological parameters in water, sediment, soil, vegetation and air.," 1981.

[48] J. M. White *et al.*, "Sodium ion in drinking water. 1. Properties, analysis, and occurrence.," *J. Am. Diet. Assoc.*, vol. 50, pp. 32–36, 1967.

[49] "Guidelines for Canadian Drinking Water Quality: Guideline Technical Document – Escherichia coli," Ottawa, Mar. 2020.

[50] C. Fritzmann, J. Löwenberg, T. Wintgens, and T. Melin, "State-of-the-art of reverse osmosis desalination," *Desalination*, 2007, doi: 10.1016/j.desal.2006.12.009.

[51] M. Cañedo-Argüelles, B. Kefford, and R. Schäfer, "Salt in freshwaters: Causes, effects and prospects - Introduction to the theme issue," *Philosophical Transactions of the Royal Society B: Biological Sciences*. 2019, doi: 10.1098/rstb.2018.0002.

[52] "Centre for Environment, Fisheries and Aquaculture Science." https://www.cefas.co.uk/.

[53] "Seabird Scientific." https://www.seabird.com/.

[54] H. A. Rahman *et al.*, "Tapered plastic multimode fiber sensor for salinity detection," *Sensors Actuators, A Phys.*, 2011, doi: 10.1016/j.sna.2011.09.024.

[55] Y. Zhao and Y. Liao, "Novel optical fiber sensor for simultaneous measurement of temperature and salinity," *Sensors Actuators, B Chem.*, 2002, doi: 10.1016/S0925-4005(02)00148-X.

[56] H. A. Rahman, S. W. Harun, M. Yasin, and H. Ahmad, "Fiber-optic salinity sensor using fiber-optic displacement measurement with flat and concave mirror," *IEEE J. Sel. Top. Quantum Electron.*, 2012, doi: 10.1109/JSTQE.2011.2159705.

[57] Q. Meng, X. Dong, K. Ni, Y. Li, B. Xu, and Z. Chen, "Optical fiber laser salinity sensor based on multimode interference effect," *IEEE Sens. J.*, 2014, doi: 10.1109/JSEN.2014.2298511.

[58] I. Hussain, M. Das, K. U. Ahamad, and P. Nath, "Water salinity detection using a smartphone," *Sensors Actuators, B Chem.*, 2017, doi: 10.1016/j.snb.2016.08.102.

[59] H. A. Rahman, S. W. Harun, M. Yasin, and H. %J I. J. of selected topics in quantum electronics Ahmad, "Fiber-optic salinity sensor using fiber-optic displacement measurement with flat and concave mirror," vol. 18, no. 5, pp. 1529–1533, 2011.

[60] B. Hou, P. Grosso, and M. Le Menn, "Principle and implementations of a refracto-nephelo-turbidimeter for seawater measurements," *Opt. Eng.*, vol. 52, no. 4, p. 44402, 2013.

[61] C. Wu, L. Sun, J. Li, and B.-O. Guan, "Highly sensitive evanescent-wave water salinity

sensor realized with rectangular optical microfiber Sagnac interferometer," in *23rd International Conference on Optical Fibre Sensors*, 2014, vol. 9157, p. 915758.

[62] N. Xie, H. Zhang, B. Liu, H. Liu, T. Liu, and C. Wang, "In-line microfiber-assisted Mach–Zehnder interferometer for microfluidic highly sensitive measurement of salinity," *IEEE Sens. J.*, vol. 18, no. 21, pp. 8767–8772, 2018.

[63] T. Okazaki, T. Orii, A. Ueda, A. Ozawa, and H. Kuramitz, "Fiber optic sensor for real-time sensing of silica scale formation in geothermal water," *Sci. Rep.*, vol. 7, no. 1, pp. 1–7, 2017.

[64] WHO, "Antimicrobial resistance. Global report on surveillance," *World Heal. Organ.*, 2014, doi: 10.1007/s13312-014-0374-3.

[65] M. K. Thomas *et al.*, "Estimates of the burden of foodborne illness in Canada for 30 specified pathogens and unspecified agents, Circa 2006," *Foodborne Pathog. Dis.*, 2013, doi: 10.1089/fpd.2012.1389.

[66] S. Jaffee, S. Henson, L. Unnevehr, D. Grace, and E. Cassou, *The Safe Food Imperative: Accelerating Progress in Low- and Middle-Income Countries*. 2018.

[67] G. Bitton, *Microbiology of Drinking Water Production and Distribution*. 2014.

[68] H. Water, "Magnitude and Burden of Waterborne Disease in the U.S." [Online]. Available: https://www.cdc.gov/healthywater/burden/index.html.

[69] WHO, "Publications on water, sanitation and health: 2017," 2018.

[70] S. Krauss and R. G. Webster, "Avian influenza virus surveillance and wild birds: Past and present," 2010, doi: 10.1637/8703-031609-Review.1.

[71] L. P. Mansfield and S. J. Forsythe, "The detection of Salmonella using a combined immunomagnetic separation and ELISA end-detection procedure," *Lett. Appl. Microbiol.*, 2000, doi: 10.1046/j.1472-765X.2000.00811.x.

[72] J. Liu *et al.*, "An integrated impedance biosensor platform for detection of pathogens in poultry products," *Sci. Rep.*, 2018, doi: 10.1038/s41598-018-33972-0.

[73] "Pathogen Testing Solutions for Salmonella, E. coli, and Listeria." https://www.solusscientific.com/.

[74] W. H. Chin *et al.*, "Direct PCR – A rapid method for multiplexed detection of different serotypes of Salmonella in enriched pork meat samples," *Mol. Cell. Probes*, 2017, doi: 10.1016/j.mcp.2016.11.004.

[75] R. K. Saiki *et al.*, "Primer-directed enzymatic amplification of DNA with a thermostable DNA polymerase," vol. 239, no. 4839, pp. 487–491, 1988.

[76] L. Yang and R. Bashir, "Electrical/electrochemical impedance for rapid detection of foodborne pathogenic bacteria," *Biotechnology Advances*. 2008, doi: 10.1016/j.biotechadv.2007.10.003.

[77] Y. He and C. Y. Chen, "Quantitative analysis of viable, stressed and dead cells of

Campylobacter jejuni strain 81-176," *Food Microbiol.*, 2010, doi: 10.1016/j.fm.2009.11.017.

[78] V. Velusamy, K. Arshak, O. Korostynka, A. Vaseashta, and C. Adley, "Real time detection of foodborne pathogens," in *Technological Innovations in Sensing and Detection of Chemical, Biological, Radiological, Nuclear Threats and Ecological Terrorism*, Springer, 2012, pp. 149–158.

[79] Z. Yu *et al.*, "Simultaneous dyeing and deposition of silver nanoparticles on cotton fabric through in situ green synthesis with black rice extract," vol. 27, no. 3, pp. 1829–1843, 2020.

[80] "No Title." [Online]. Available: https://www.abcam.com/kits/elisa-principle.

[81] Enzoclopus, "No Title." [Online]. Available: https://commons.wikimedia.org/wiki/File:Polymerase_chain_reaction-en.svg), https://creativecommons.org/licenses/by-sa/4.0/legalcode.

[82] L. Marle and G. M. %J T. T. in A. C. Greenway, "Microfluidic devices for environmental monitoring," vol. 24, no. 9, pp. 795–802, 2005.

[83] J. C. Jokerst, J. M. Emory, and C. S. Henry, "Advances in microfluidics for environmental analysis," *Analyst*, vol. 137, no. 1, pp. 24–34, 2012.

[84] R. Pol, F. Céspedes, D. Gabriel, and M. Baeza, "Microfluidic lab-on-a-chip platforms for environmental monitoring," *TrAC Trends Anal. Chem.*, vol. 95, pp. 62–68, 2017.

[85] H.-F. Li and J.-M. Lin, "Applications of microfluidic systems in environmental analysis," *Anal. Bioanal. Chem.*, vol. 393, no. 2, pp. 555–567, 2009.

[86] W. R. Heineman, "Introduction to Electroanalytical Chemistry," *Chem. Instrum. A Syst. Approach*, pp. 963–999, 1989.

[87] J. T. Maloy, "Factors affecting the shape of current-potential curves." ACS Publications, 1983.

[88] I. Karube, Y. Nomura, and Y. Arikawa, "Biosensors for environmental control," *TrAC Trends Anal. Chem.*, vol. 14, no. 7, pp. 295–299, 1995.

[89] J. Janata, "Conductometric sensors," in *Principles of Chemical Sensors*, Springer, 2009, pp. 241–266.

[90] G. Luka *et al.*, "Microfluidics integrated biosensors: A leading technology towards lab-on-a-chip and sensing applications," *Sensors*, vol. 15, no. 12, pp. 30011–30031, 2015.

[91] J. Wang, "Electrochemical nucleic acid biosensors," *Anal. Chim. Acta*, vol. 469, no. 1, pp. 63–71, 2002.

[92] P. D'Orazio, "Biosensors in clinical chemistry," *Clin. Chim. Acta*, vol. 334, no. 1–2, pp. 41–69, 2003.

[93] B. Bottazzi *et al.*, "Multiplexed label-free optical biosensor for medical diagnostics," *J. Biomed. Opt.*, vol. 19, no. 1, p. 17006, 2014.

[94] S. Pal, A. R. Yadav, M. A. Lifson, J. E. Baker, P. M. Fauchet, and B. L. Miller, "Selective virus detection in complex sample matrices with photonic crystal optical cavities," *Biosens. Bioelectron.*, vol. 44, pp. 229–234, 2013.

[95] Z. Zhong *et al.*, "Fiber optic monooxygenase biosensor for toluene concentration measurement in aqueous samples," *Biosens. Bioelectron.*, vol. 26, no. 5, pp. 2407–2412, 2011.

[96] X. Fan, I. M. White, S. I. Shopova, H. Zhu, J. D. Suter, and Y. Sun, "Sensitive optical biosensors for unlabeled targets: A review," *Anal. Chim. Acta*, vol. 620, no. 1–2, pp. 8–26, 2008.

[97] S. Liu, Z. Zheng, and X. Li, "Advances in pesticide biosensors: current status, challenges, and future perspectives," *Anal. Bioanal. Chem.*, vol. 405, no. 1, pp. 63–90, 2013.

[98] T. F. McGrath, K. Andersson, K. Campbell, T. L. Fodey, and C. T. Elliott, "Development of a rapid low cost fluorescent biosensor for the detection of food contaminants," *Biosens. Bioelectron.*, vol. 41, pp. 96–102, 2013.

[99] X. Xu, X. Liu, Y. Li, and Y. Ying, "A simple and rapid optical biosensor for detection of aflatoxin B1 based on competitive dispersion of gold nanorods," *Biosens. Bioelectron.*, vol. 47, pp. 361–367, 2013.

[100] M. Gabig-Ciminska, "Developing nucleic acid-based electrical detection systems," *Microb. Cell Fact.*, vol. 5, no. 1, p. 9, 2006.

[101] M. Citartan, S. C. B. Gopinath, J. Tominaga, and T.-H. Tang, "Label-free methods of reporting biomolecular interactions by optical biosensors," *Analyst*, vol. 138, no. 13, pp. 3576–3592, 2013.

[102] B. Sciacca and T. M. Monro, "Dip biosensor based on localized surface plasmon resonance at the tip of an optical fiber," *Langmuir*, vol. 30, no. 3, pp. 946–954, 2014.

[103] P. D. Ohlsson, O. Ordeig, K. B. Mogensen, and J. P. Kutter, "Electrophoresis microchip with integrated waveguides for simultaneous native UV fluorescence and absorbance detection," *Electrophoresis*, vol. 30, no. 24, pp. 4172–4178, 2009.

[104] A. J. Driscoll, M. H. Harpster, and P. A. Johnson, "The development of surface-enhanced Raman scattering as a detection modality for portable in vitro diagnostics: progress and challenges," *Phys. Chem. Chem. Phys.*, vol. 15, no. 47, pp. 20415–20433, 2013.

[105] P. Kozma, F. Kehl, E. Ehrentreich-Förster, C. Stamm, and F. F. Bier, "Integrated planar optical waveguide interferometer biosensors: A comparative review," *Biosens. Bioelectron.*, vol. 58, pp. 287–307, 2014.

[106] S. Hosseini, F. Ibrahim, I. Djordjevic, and L. H. Koole, "Recent advances in surface functionalization techniques on polymethacrylate materials for optical biosensor applications," *Analyst*, vol. 139, no. 12, pp. 2933–2943, 2014.

[107] D. B. Go, M. Z. Atashbar, Z. Ramshani, and H.-C. %J A. methods Chang, "Surface acoustic wave devices for chemical sensing and microfluidics: a review and perspective," vol. 9, no. 28, pp. 4112–4134, 2017.

[108] J.-W. Thies, P. Kuhn, B. Thürmann, S. Dübel, and A. %J M. E. Dietzel, "Microfluidic quartz-crystal-microbalance (QCM) sensors with specialized immunoassays for extended measurement range and improved reusability," vol. 179, pp. 25–30, 2017.

[109] R. R. Anderson *et al.*, "Transient deflection response in microcantilever array integrated with polydimethylsiloxane (PDMS) microfluidics," vol. 11, no. 12, pp. 2088–2096, 2011.

[110] K. Chon, J. Moon, S. Kim, S. D. Kim, and J. Cho, "Bio-particle separation using microfluidic porous plug for environmental monitoring," *Desalination*, 2007, doi: 10.1016/j.desal.2005.12.057.

[111] C. Sun, S.-T. Chen, and P.-J. Hsiao, "Mapping the salinity gradient in a microfluidic device with schlieren imaging," *Sensors*, vol. 15, no. 5, pp. 11587–11600, 2015.

[112] M. Kim, W. Choi, H. Lim, and S. Yang, "Integrated microfluidic-based sensor module for real-time measurement of temperature, conductivity, and salinity to monitor reverse osmosis," *Desalination*, 2013, doi: 10.1016/j.desal.2013.03.007.

[113] D. Saerens, L. Huang, K. Bonroy, and S. Muyldermans, "Antibody fragments as probe in biosensor development," *Sensors*, vol. 8, no. 8, pp. 4669–4686, 2008.

[114] M. McKeague, C. R. Bradley, A. De Girolamo, A. Visconti, J. D. Miller, and M. C. DeRosa, "Screening and initial binding assessment of fumonisin B1 aptamers," *Int. J. Mol. Sci.*, vol. 11, no. 12, pp. 4864–4881, 2010.

[115] H. Lin, W. Zhang, S. Jia, Z. Guan, C. J. Yang, and Z. Zhu, "Microfluidic approaches to rapid and efficient aptamer selection," *Biomicrofluidics*, vol. 8, no. 4, p. 41501, 2014.

[116] Y. Jiang, S. Zou, and X. Cao, "A simple dendrimer-aptamer based microfluidic platform for E. coli O157: H7 detection and signal intensification by rolling circle amplification," *Sensors Actuators B Chem.*, vol. 251, pp. 976–984, 2017.

[117] T. Li *et al.*, "Naked-eye based point-of-care detection of E. coli O157: H7 by a signal-amplified microfluidic aptasensor," *Anal. Chim. Acta*, vol. 1130, pp. 20–28, 2020.

[118] A. T. Bayrac *et al.*, "In vitro selection of DNA aptamers to glioblastoma multiforme," *ACS Chem. Neurosci.*, vol. 2, no. 3, pp. 175–181, 2011.

[119] D. Hilvert, "Critical analysis of antibody catalysis," *Annu. Rev. Biochem.*, vol. 69, no. 1, pp. 751–793, 2000.

[120] S. Subrahmanyam, S. A. Piletsky, and A. P. F. Turner, "Application of natural receptors in sensors and assays," *Anal. Chem.*, vol. 74, no. 16, pp. 3942–3951, 2002.

[121] D. B. Weibel and G. M. Whitesides, "Applications of microfluidics in chemical biology," *Curr. Opin. Chem. Biol.*, vol. 10, no. 6, pp. 584–591, 2006.

[122] M. R. Bringer, C. J. Gerdts, H. Song, J. D. Tice, and R. F. Ismagilov, "Microfluidic systems for chemical kinetics that rely on chaotic mixing in droplets," *Philos. Trans. R. Soc. London. Ser. A Math. Phys. Eng. Sci.*, vol. 362, no. 1818, pp. 1087–1104, 2004.

[123] D. N. Breslauer, P. J. Lee, and L. P. Lee, "Microfluidics-based systems biology," *Mol. Biosyst.*, vol. 2, no. 2, pp. 97–112, 2006.

[124] K. Sato, K. Mawatari, and T. Kitamori, “Microchip-based cell analysis and clinical diagnosis system,” *Lab Chip*, vol. 8, no. 12, pp. 1992–1998, 2008.

[125] Y.-H. Kim *et al.*, “An RNA aptamer that specifically binds pancreatic adenocarcinoma up-regulated factor inhibits migration and growth of pancreatic cancer cells,” *Cancer Lett.*, vol. 313, no. 1, pp. 76–83, 2011.

[126] J. G. E. Gardeniers and A. van den Berg, “Lab-on-a-chip systems for biomedical and environmental monitoring,” *Anal. Bioanal. Chem.*, vol. 378, no. 7, pp. 1700–1703, 2004.

[127] S. Ghosh Dastider, S. Barizuddin, N. S. Yuksek, M. Dweik, and M. F. Almasri, “Efficient and rapid detection of Salmonella using microfluidic impedance based sensing,” *J. Sensors*, vol. 2015, 2015.

[128] L. Yao, L. Wang, F. Huang, G. Cai, X. Xi, and J. Lin, “A microfluidic impedance biosensor based on immunomagnetic separation and urease catalysis for continuous-flow detection of E. coli O157: H7,” *Sensors Actuators B Chem.*, vol. 259, pp. 1013–1021, 2018.

[129] Y. Hou, G. Cai, L. Zheng, and J. Lin, “A microfluidic signal-off biosensor for rapid and sensitive detection of Salmonella using magnetic separation and enzymatic catalysis,” *Food Control*, 2019, doi: 10.1016/j.foodcont.2019.04.008.

[130] S. Wang *et al.*, “Rapid and ultrasensitive detection of Salmonella typhimurium using a novel impedance biosensor based on SiO2@ MnO2 nanocomposites and interdigitated array microelectrodes,” *Sensors Actuators B Chem.*, vol. 324, p. 128654, 2020.

[131] Z. Altintas, M. Akgun, G. Kokturk, and Y. Uludag, “A fully automated microfluidic-based electrochemical sensor for real-time bacteria detection,” *Biosens. Bioelectron.*, vol. 100, pp. 541–548, 2018.

[132] K. L. Brogan and D. R. Walt, “Optical fiber-based sensors: application to chemical biology,” *Curr. Opin. Chem. Biol.*, vol. 9, no. 5, pp. 494–500, 2005.

[133] F. Mi *et al.*, “Recent advancements in microfluidic chip biosensor detection of foodborne pathogenic bacteria: a review,” *Anal. Bioanal. Chem.*, pp. 1–20, 2022.

[134] J. Yu, H. Wu, L. He, L. Tan, Z. Jia, and N. %J T. Gan, “The universal dual-mode aptasensor for simultaneous determination of different bacteria based on naked eyes and microfluidic-chip together with magnetic DNA encoded probes,” vol. 225, p. 122062, 2021.

[135] L. Sun *et al.*, “A novel, simple and low-cost paper-based analytical device for colorimetric detection of Cronobacter spp,” vol. 1036, pp. 80–88, 2018.

[136] S.-A. Tan, T. Agarwal, S. Kar, M. R. Borrelli, T. K. Maiti, and P. Makvandi, “A progressive review on paper-based bacterial colorimetric detection and antimicrobial susceptibility testing,” in *Food, Medical, and Environmental Applications of Polysaccharides*, Elsevier, 2021, pp. 687–718.

[137] J. C. Jokerst, J. A. Adkins, B. Bisha, M. M. Mentele, L. D. Goodridge, and C. S. Henry, “Development of a paper-based analytical device for colorimetric detection of select

foodborne pathogens," *Anal. Chem.*, vol. 84, no. 6, pp. 2900–2907, 2012.

[138] E. R. Peskind *et al.*, "Cerebrospinal fluid epinephrine in Alzheimer's disease and normal aging," *Neuropsychopharmacology*, vol. 19, no. 6, pp. 465–471, 1998.

[139] W. Nawrot, K. Drzozga, S. Baluta, J. Cabaj, and K. Malecha, "A fluorescent biosensors for detection vital body fluids' agents," *Sensors*, vol. 18, no. 8, p. 2357, 2018.

[140] L. Xue, L. Zheng, H. Zhang, X. Jin, and J. Lin, "An ultrasensitive fluorescent biosensor using high gradient magnetic separation and quantum dots for fast detection of foodborne pathogenic bacteria," *Sensors Actuators B Chem.*, vol. 265, pp. 318–325, 2018.

[141] S. Yu, Y. Tang, M. Yan, Z. P. Aguilar, W. Lai, and H. Xu, "A fluorescent cascade amplification method for sensitive detection of Salmonella based on magnetic Fe3O4 nanoparticles and hybridization chain reaction," *Sensors Actuators B Chem.*, vol. 279, pp. 31–37, 2019.

[142] J. R. Choi, K. W. Yong, J. Y. Choi, and A. C. Cowie, "Emerging point-of-care technologies for food safety analysis," *Sensors*, vol. 19, no. 4, p. 817, 2019.

[143] R. Wang, Y. Xu, Y. Jiang, N. Chuan, X. Su, and J. Ji, "Sensitive quantification and visual detection of bacteria using CdSe/ZnS@ SiO 2 nanoparticles as fluorescent probes," *Anal. Methods*, vol. 6, no. 17, pp. 6802–6808, 2014.

[144] I. Kubo, M. Kajiya, N. Aramaki, and S. Furutani, "Detection of salmonella enterica in egg yolk by PCR on a microfluidic disc device using immunomagnetic beads," *Sensors*, vol. 20, no. 4, p. 1060, 2020.

[145] X. Tan *et al.*, "Rapid mouse follicle stimulating hormone quantification and estrus cycle analysis using an automated microfluidic chemiluminescent ELISA system," *ACS sensors*, vol. 3, no. 11, pp. 2327–2334, 2018.

[146] N. M. Matos Pires and T. Dong, "Microfluidic biosensor array with integrated poly (2, 7-carbazole)/fullerene-based photodiodes for rapid multiplexed detection of pathogens," *Sensors*, vol. 13, no. 12, pp. 15898–15911, 2013.

[147] J. L. Delaney, C. F. Hogan, J. Tian, and W. Shen, "Electrogenerated chemiluminescence detection in paper-based microfluidic sensors," *Anal. Chem.*, vol. 83, no. 4, pp. 1300–1306, 2011.

[148] R. B. M. Schasfoort, *Handbook of surface plasmon resonance*. Royal Society of Chemistry, 2017.

[149] Y. Luo, F. Yu, and R. N. Zare, "Microfluidic device for immunoassays based on surface plasmon resonance imaging," *Lab Chip*, vol. 8, no. 5, pp. 694–700, 2008.

[150] M. G. Manera *et al.*, "SPR based immunosensor for detection of Legionella pneumophila in water samples," *Opt. Commun.*, vol. 294, pp. 420–426, 2013.

[151] O. Tokel *et al.*, "Portable microfluidic integrated plasmonic platform for pathogen detection," *Sci. Rep.*, vol. 5, no. 1, pp. 1–9, 2015.

[152] J. Gomez-Cruz, S. Nair, A. Manjarrez-Hernandez, S. Gavilanes-Parra, G. Ascanio, and C.

Escobedo, “Cost-effective flow-through nanohole array-based biosensing platform for the label-free detection of uropathogenic E. coli in real time,” *Biosens. Bioelectron.*, vol. 106, pp. 105–110, 2018.

[153] T. W. Ebbesen, H. J. Lezec, H. F. Ghaemi, T. Thio, and P. A. Wolff, “Extraordinary optical transmission through sub-wavelength hole arrays,” *Nature*, vol. 391, no. 6668, pp. 667–669, 1998.

[154] B. N. Feltis, B. A. Sexton, F. L. Glenn, M. J. Best, M. Wilkins, and T. J. Davis, “A hand-held surface plasmon resonance biosensor for the detection of ricin and other biological agents,” *Biosens. Bioelectron.*, vol. 23, no. 7, pp. 1131–1136, 2008.

[155] Y. Wang, S. Su, S. Du, Y. Gao, Z. Xu, and H. Zhang, “Rapid Detection for Salmonella typhimurium by Conventional Resistive Temperature Sensor Based on Photothermal Effect of Carboxylated Graphene Oxide,” *Food Anal. Methods*, 2020, doi: 10.1007/s12161-020-01793-5.

[156] S. Du, Y. Wang, Z. Liu, Z. Xu, and H. Zhang, “A portable immune-thermometer assay based on the photothermal effect of graphene oxides for the rapid detection of Salmonella typhimurium,” *Biosens. Bioelectron.*, 2019, doi: 10.1016/j.bios.2019.111670.

[157] L. Lu *et al.*, “Rapid and sensitive multimode detection of Salmonella typhimurium based on the photothermal effect and peroxidase-like activity of MoS2@Au nanocomposite,” *Sensors Actuators, B Chem.*, 2021, doi: 10.1016/j.snb.2020.128807.

[158] M. Jia, J. Liu, J. Zhang, and H. Zhang, “An immunofiltration strip method based on the photothermal effect of gold nanoparticles for the detection of: Escherichia coli O157:H7,” *Analyst*, 2019, doi: 10.1039/c8an01004h.

[159] A. B. Baldwin, “Thin-Film Impedimetric Sensors for Chronic in vivo Use: Design and Application to Hydrocephalus Treatment,” University of Southern California, 2018.

[160] S. COMSOL Multiphysics® v. 5.5. COMSOL AB, Stockholm, “Chemical Reaction Engineering Module,” 2019.

[161] P. Vanýsek, “Equivalent Conductivity of Electrolytes in Aqueous Solution,” *Handb. Chem. Phys.*, 2012.

[162] N. Walton, “Electrical conductivity and total dissolved solids—what is their precise relationship?,” *Desalination*, vol. 72, no. 3, pp. 272–292, 1989.

[163] A. F. Rusydi, “Correlation between conductivity and total dissolved solid in various type of water: A review,” in *IOP conference series: earth and environmental science*, 2018, p. 12019.

[164] S. COMSOL Multiphysics® v. 5.5. COMSOL AB, Stockholm, “Heat Transfer Module,” 2019.

[165] J. H. Lienhard IV and J. H. Lienhard V, *A HEAT TRANSFER TEXTBOOK, fourth edition*. 2017.

[166] M. H. Sharqawy, J. H. Lienhard V, and S. M. Zubair, “Thermophysical properties of

seawater: A review of existing correlations and data," *Desalin. Water Treat.*, 2010, doi: 10.5004/dwt.2010.1079.

[167] K. G. Nayar, M. H. Sharqawy, L. D. Banchik, and J. H. Lienhard, "Thermophysical properties of seawater: A review and new correlations that include pressure dependence," *Desalination*, 2016, doi: 10.1016/j.desal.2016.02.024.

[168] Y.-C. Lu *et al.*, "Bacteria detection utilizing electrical conductivity," *Biosens. Bioelectron.*, vol. 23, no. 12, pp. 1856–1861, 2008.

[169] H. Wiggenhauser, "Active IR-applications in civil engineering," *Infrared Phys. Technol.*, vol. 43, no. 3–5, pp. 233–238, 2002.

[170] O. Breitenstein, M. Langenkamp, F. Altmann, D. Katzer, A. Lindner, and H. Eggers, "Microscopic lock-in thermography investigation of leakage sites in integrated circuits," *Rev. Sci. Instrum.*, vol. 71, no. 11, pp. 4155–4160, 2000.

[171] F. Ciampa, P. Mahmoodi, F. Pinto, and M. Meo, "Recent advances in active infrared thermography for non-destructive testing of aerospace components," *Sensors*, vol. 18, no. 2, p. 609, 2018.

[172] N. Tabatabaei, A. Mandelis, M. Dehghany, K. H. Michaelian, and B. T. Amaechi, "On the sensitivity of thermophotonic lock-in imaging and polarized Raman spectroscopy to early dental caries diagnosis," *J. Biomed. Opt.*, vol. 17, no. 2, p. 25002, 2012.

[173] M. Kaczmarek, A. Nowakowski, A. Renkielska, J. Grudzinski, and W. Stojek, "Investigation of skin burns basing on active thermography," in *2001 Conference Proceedings of the 23rd Annual International Conference of the IEEE Engineering in Medicine and Biology Society*, 2001, vol. 3, pp. 2882–2885.

[174] B. Wiecek and S. Zwolenik, "Thermal wave method-limits and potentialities of active thermography in biology and medicine," in *Proceedings of the Second Joint 24th Annual Conference and the Annual Fall Meeting of the Biomedical Engineering Society][Engineering in Medicine and Biology*, 2002, vol. 2, pp. 1133–1134.

[175] D. Thapa, N. Samadi, and N. Tabatabaei, "Handheld Thermo-Photonic Device for Rapid, Low-Cost, and On-Site Detection and Quantification of Anti-SARS-CoV-2 Antibody," *IEEE Sens. J.*, vol. 21, no. 17, pp. 18504–18511, 2021.

[176] C. Ibarra-Castanedo *et al.*, "Comparative study of active thermography techniques for the nondestructive evaluation of honeycomb structures," *Res. Nondestruct. Eval.*, vol. 20, no. 1, pp. 1–31, 2009.

[177] M. Genest, M. Martinez, N. Mrad, G. Renaud, and A. Fahr, "Pulsed thermography for non-destructive evaluation and damage growth monitoring of bonded repairs," *Compos. Struct.*, vol. 88, no. 1, pp. 112–120, 2009.

[178] C. Ibarra-Castanedo, M. Genest, P. Servais, X. P. V Maldague, and A. Bendada, "Qualitative and quantitative assessment of aerospace structures by pulsed thermography," *Nondestruct. Test. Eval.*, vol. 22, no. 2–3, pp. 199–215, 2007.

[179] R. Stoessel *et al.*, "Review of some measurement techniques involved in modern NDE,"

2001.

[180] G. Busse, “Nondestructive evaluation of polymer materials,” *NDT E Int.*, vol. 27, no. 5, pp. 253–262, 1994.

[181] G. BuSSe, D. Wu, and W. Karpen, “Thermal wave imaging with phase sensitive modulated thermography,” *J. Appl. Phys.*, vol. 71, no. 8, pp. 3962–3965, 1992.

[182] V. P. Vavilov and S. Marinetti, “Pulsed phase thermography and fourier-analysis thermal tomography,” *Russ. J. Nondestruct. Test.*, vol. 35, no. 2, pp. 134–145, 1999.

[183] X. Maldague and S. Marinetti, “Pulse phase infrared thermography,” *J. Appl. Phys.*, vol. 79, no. 5, pp. 2694–2698, 1996.

[184] F. Galmiche and X. Maldague, “Depth defect retrieval using the wavelet pulsed phased thermography,” in *Proc. QIRT*, 2000, pp. 194–199.

[185] N. Tabatabaei, “Matched-filter thermography,” *Appl. Sci.*, vol. 8, no. 4, p. 581, 2018.

[186] N. Tabatabaei and A. Mandelis, “Thermal-wave radar: A novel subsurface imaging modality with extended depth-resolution dynamic range,” *Rev. Sci. Instrum.*, vol. 80, no. 3, p. 34902, 2009.

[187] N. Tabatabaei and A. Mandelis, “Thermal coherence tomography using match filter binary phase coded diffusion waves,” *Phys. Rev. Lett.*, vol. 107, no. 16, p. 165901, 2011.

[188] N. Tabatabaei, A. Mandelis, and B. T. Amaechi, “Thermophotonic radar imaging: An emissivity-normalized modality with advantages over phase lock-in thermography,” *Appl. Phys. Lett.*, vol. 98, no. 16, p. 163706, 2011.

[189] R. Schlangen *et al.*, “Use of lock-in thermography for non-destructive 3D defect localization on system in package and stacked-die technology,” in *proceedings of ISTFA*, 2011, pp. 68–73.

[190] S. Huth, O. Breitenstein, A. Huber, D. Dantz, U. Lambert, and F. Altmann, “Lock-in IR-thermography - A novel tool for material and device characterization,” 2002, doi: 10.4028/www.scientific.net/ssp.82-84.741.

[191] N. Tabatabaei, A. Mandelis, and B. T. Amaechi, “Thermophotonic lock-in imaging of early demineralized and carious lesions in human teeth,” *J. Biomed. Opt.*, vol. 16, no. 7, p. 71402, 2011.

[192] C. Meola, G. M. Carlomagno, A. Squillace, and G. Giorleo, “Non-destructive control of industrial materials by means of lock-in thermography,” *Meas. Sci. Technol.*, vol. 13, no. 10, p. 1583, 2002.

[193] M. Bonmarin and F.-A. Le Gal, “Lock-in thermal imaging for the early-stage detection of cutaneous melanoma: a feasibility study,” *Comput. Biol. Med.*, vol. 47, pp. 36–43, 2014.

[194] W. Karpen, D. Wu, R. Steegmuller, and G. Busse, “Depth profiling of orientation in laminates with local lockin thermography,” in *Proc. QIRT*, 1994, vol. 94, pp. 23–26.

[195] C. Meola and G. M. Carlomagno, “The role of infrared thermography in NDT,” in

Nondestructive Testing of Materials and Structures, Springer, 2013, pp. 91–96.

[196] Y.-K. An, J. M. Kim, and H. Sohn, "Laser lock-in thermography for detection of surface-breaking fatigue cracks on uncoated steel structures," *Ndt E Int.*, vol. 65, pp. 54–63, 2014.

[197] C. John and A. Salerno, "Raw data set of thermal wave propagation in hard dental tissues," in *Proc. of 11th Int. Symp. and Exhibition for Computer Assisted Radiology (CAR97)*, 1997, vol. 986, pp. 986–1052.

[198] C. John, D. Wu, A. Salerno, G. Busse, and C. Löst, "Applying phase sensitive modulated thermography to ground sections of a human tooth," in *Nondestructive Characterization of Materials VIII*, Springer, 1998, pp. 757–762.

[199] A. Ojaghi, A. Parkhimchyk, and N. Tabatabaei, "First step toward translation of thermophotonic lock-in imaging to dentistry as an early caries detection technology," *J. Biomed. Opt.*, vol. 21, no. 9, p. 96003, 2016.

[200] Z. Instruments, "Principles of lock-in detection and the state of the art," *CH-8005 Zurich, Switzerland, Accessed*, 2016.

[201] R. Schlangen *et al.*, "Dynamic lock-in thermography for operation mode-dependent thermally active fault localization," *Microelectron. Reliab.*, vol. 50, no. 9–11, pp. 1454–1458, 2010.

[202] M. Annabestani, P. Esmaeili-Dokht, and M. Fardmanesh, "A novel, low cost, and accessible method for rapid fabrication of the modifiable microfluidic devices," *Sci. Rep.*, vol. 10, no. 1, pp. 1–10, 2020.

[203] S. K. Vashist and J. H. T. Luong, "Antibody immobilization and surface functionalization chemistries for immunodiagnostics," in *Handbook of Immunoassay Technologies*, Elsevier, 2018, pp. 19–46.

[204] K. L. Brogan, J. H. Shin, and M. H. Schoenfisch, "Influence of surfactants and antibody immobilization strategy on reducing nonspecific protein interactions for molecular recognition force microscopy," *Langmuir*, vol. 20, no. 22, pp. 9729–9735, 2004.

[205] T. Emami, R. Madani, F. Golchinfar, A. Shoushtary, and S. M. Amini, "Comparison of gold nanoparticle conjugated secondary antibody with non-gold secondary antibody in an ELISA kit model," *Monoclon. Antib. Immunodiagn. Immunother.*, vol. 34, no. 5, pp. 366–370, 2015.

[206] F. Laugere, G. W. Lubking, J. Bastemeijer, and M. J. Vellekoop, "Design of an electronic interface for capacitively coupled four-electrode conductivity detection in capillary electrophoresis microchip," *Sensors Actuators B Chem.*, vol. 83, no. 1–3, pp. 104–108, 2002.

[207] H. A. Broadbent, S. Z. Ivanov, and D. P. Fries, "A miniature, low cost CTD system for coastal salinity measurements," *Meas. Sci. Technol.*, 2007, doi: 10.1088/0957-0233/18/11/005.

[208] S. H. Russ, V. Perepa, S. Leavesly, and B. Webb, "Novel low-cost salinity sensor for embedded environmental monitoring," in *Proceedings of the IEEE SoutheastCon 2010*

(SoutheastCon), 2010, pp. 53–56.

[209] P. M. Ramos, J. M. D. Pereira, H. M. G. Ramos, and A. L. Ribeiro, “A four-terminal water-quality-monitoring conductivity sensor,” *IEEE Trans. Instrum. Meas.*, vol. 57, no. 3, pp. 577–583, 2008.

[210] G. Herzog, W. Moujahid, K. Twomey, C. Lyons, and V. I. Ogurtsov, “On-chip electrochemical microsystems for measurements of copper and conductivity in artificial seawater,” *Talanta*, vol. 116, pp. 26–32, 2013.